# Characterizing the lattice induced light shifts of the Ytterbium optical lattice clock

UNIVERSITY OF
COPENHAGEN

ASBJØRN ARVAD JØRGENSEN

A MAN WITH A WATCH KNOWS WHAT TIME IT IS. A MAN WITH TWO
WATCHES IS NEVER SURE

SEGAL'S LAW

# Characterizing the lattice induced light shifts of the Ytterbium optical lattice clock

| | |
|---|---|
| Author | Asbjørn Arvad Jørgensen |
| Advisor | Prof. Hidetoshi Katori[1] |
| Advisor | Assoc. prof. Jan Westenkær Thomsen[2] |

[1]RIKEN Quantum Metrology Laboratory - Japan

[2] QUANTOP The Niels Bohr Institute - Denmark

Quantum Optics and Ultra Cold Atom Group
The Niels Bohr Institute

Submitted to the University of Copenhagen
May 17, 2017
Revised on
September 15, 2017

## Abstract

The atomic optical lattice clocks use, as the name suggests, an optical lattice to trap a large number of neutral atoms allowing Doppler and recoil free clock spectroscopy. The disadvantage of using an optical lattice is that the high intensity required for trapping introduces large AC stark shifts which perturb the clock transition. By choosing the wavelength of the optical lattice correctly this effect can be minimized but never canceled. In order to reach fractional stabilities of $10^{-17}$ and below we need to characterize the remaining AC stark shifts to better precision than they are currently known. In this work we present a novel introduction to the theory behind the optical lattice clocks and the light shift model used to describe the AC stark shifts. We detail the operation of the ytterbium lattice clock and present the changes that were made to the optical setup in order to investigate the light shifts at higher lattice intensities than previously possible. We then present the analysis of the frequency measurements together with a new way of modeling the sideband spectra in order to extract the operational parameters. Finally we present the analysis which determines the light shift model coefficients and find a large improvement in precision over previous values.

## Resume

Et optisk gitter atom ur bruger, som navnet antyder, et optisk gitter til at fange et stort antal neutrale atomer. Gitteret fanger atomerne så stærkt at man kan lave Dopplerfri og rekylfri spectroscopi. Ulempen ved at bruge et optisk gitter er at det kræver en meget høj intensitet hvilket skaber stærke AC stark forskydningerne der perturberer atom overgangen. Ved at vælge den rigtige bølgelængde kan denne effect minimeres, men den forsvinder aldrig helt. For at nå fractionelle stabiliteter på $10^{-17}$ eller lavere kræver det at vi bestemmer de tilbageværende AC stark forskydninger til bedre præcision end de er kendt idag. I denne rapport presenterer vi en simpel introducktion til teorien bag optiske gitter ure og den model der bruges til at beskrive AC stark forskydningerne. Vi beskriver hvordan ytterbium gitter uret fungerer og detaljerer de ændringer der er lavet for at kunne undersøge AC stark forskydningerne ved højere gitter intensitet end tidligere muligt beskriver. Derefter beskriver vi analysen af frekvensmålingerne sammen med en ny metode til at modellere sidebåndsspetre for at bestemme de operationelle parametre. Til sidst præsenterer vi den analyse der bestemmer de nye koefficienter til AS stark shift modellen og vi finder en stor forbedring i præsision i forhold til tidligere resultater hvis man kun medtager statistiske usikkerheder.

# Acknowledgement

This thesis has been a long time underway and if I had to thank everybody who has supported me throughout this past year I would likely double the page count. There are however a few who I would like to thank explicitly.

First of all I would like to thank Professor Hidetoshi Katori. As the chief scientist at the Riken Quantum Metrology Laboratory he was the one who generously allowed me to join the lab for eleven months. From the first day I set foot in his office I felt very welcome.

Secondly I want to thank Dr. Nils Nemitz who became my daily supervisor on the Yb clock experiment and whom I stayed in close contact with during the writing process in Denmark. He spent countless hours teaching me about every detail of the Yb clock. He taught me the value of long working nights and to treasure sleep whenever it was available. He taught me the beauty of sitting in a laboratory at 4.05 in the morning and uncovering your own little piece of the great secrets of the universe. This thesis would not have been anything without his thorough and detailed feedback on every chapter.

I want to thank my Danish supervisor Jan Thomsen for taking on the Challenge of supervising a student on the other side of the globe. Even when he was very busy he always had time for skype conversations and emails and he has been a great help after I came back from Japan.

I also want to thank the rest of the members of the Riken laboratory who each never shied back from helping me with whatever problems I had. I want to thank Dr. Atsushi Yamaguchi for always remembering to invite me to lunch, Dr. Nobuaki Ohmae who was always willing to beat the comb lasers back in place, Dr. Ichiro Ushijima for being overbearing with me whenever I bumped a mirror belonging to the Strontium setup and Dr. Manoj Das for all the friendly chat in the break room and for always inquiring about my day.

A special thanks goes to assistant Megumi Kobayashi and secretary Makiko Tanaka. Without their help I would never even have set foot in Japan, and without their continuous support during my stay I would probably still be there - stuck in some endless bureaucratic loop.

I must also thank Takuya Ohkubo whom sadly left the lab just as I arrived. His doctor thesis on the Yb clock has been immensely helpful and a great resource during my writing process.

A big thanks goes to the other students whom I shared time with in the Riken lab. To Tadahiro Takahashi and Yusuke Kimone who welcomed me from the first day I set foot in the lab and Masatoshi Matsuura who joined us later.

I also want to thank the student Ryotatsu Yanagimoto who did his bachelor work on the Yb clock. His pure interest in physics and diligent nature always inspired me to do better.

Bjarke Tahaski Røjle Christensen also deserves a big thanks for giving me the inspiration and the push to go to Japan.

Lastly I want to thank Anine Borger, Christoffer Østfeldt and Freja Thilde Pedersen for reading through my unfinished an barely understandable chapters.

And finally I want to thank Sofus Laguna Kristensen for the nice desk.

# Contents

# Prologue

*The most universal standard of length which we could assume would be the wave length in vaccum of a particular kind of light, emitted by some widely diffused substance such as sodium, which has well-defined lines in its spectrum. (...) A more universal unit of time might be found by taking the periodic time of vibration of the particular kind of light whose wavelength is the unit of length.*

— James Clerk Maxwell*, A Treatise on Electricity and Magnetism - 1873*

## 1.1   Introduction

Old as time itself - is a popular idiom for good reason. Having a concept of time, and more importantly, a systematic way of defining it, is paramount to a civilized society. Not only does it give us the ability soft boil eggs, it also allows us to arrange meetings, organize our lives, use a global positioning system, and calculate how many episodes of the newest Netflix series I can watch before I have to leave for work.

However, being able to perfectly soft boil my eggs is not that impressive if I cannot explain to my neighbor how long it took. For this Mankind needs a common agreed upon time reference. To create a time reference all that is needed is some type of periodic event happening with a fixed frequency

Creating a *good* time reference relies on two important qualities; stability and accuracy, with the former describing how much the reference systematically changes over time, and the latter describing how far off the reference is from the 'true' value. One might include precision, the random fluctuation of the reference, as an important quality, but the mean value of an imprecise but stable reference can be determined by averaging over many measurements

For centuries we used the movement of the sun across the sky and the changing phases of the moon as frequency references. But since the frequency

of both is very low, it is difficult to measure shorter periods of time, i.e. the cooking time of an egg or the length of a guard watch.

This led to the construction of man made clocks, starting with the water clocks dating back to ancient Egypt, to the pendulum clocks during the 17'th century and electronic and crystal oscillators three centuries later.

Common to all the man made clocks were that they were very sensitive to variations in environmental parameters such as temperature, humidity or gravity. For these reasons, when the first scientific definition of the SI second finally happened in the 1940's, it was not a man made frequency reference but rather defined as was as $\frac{1}{86400}$ of a mean solar day. This was the most stable frequency reference known to man at the time even though it is fundamentally limited by tidal effects caused by the moon. This causes Earths rotation period to increase by 1.8 ms per century[24], corresponding to a fractional stability:

$$\frac{\delta\nu}{\nu_0} = \frac{1.8 \text{ ms}}{\text{century}} = \frac{1.8 \text{ ms}}{3153600000 \text{ s}} = 5.7 \times 10^{-13}, \tag{1.1}$$

if it was only limited by the tidal effects. For comparison the best pendulum clocks today have a fractional stability of $10^{-8}$, while quartz oscillators used in wrist watches have only $10^{-7}$([20]).

### 1.1.1   The atomic clock

In 1873 Maxwell had noticed that certain lamps emitted a spectral pattern with very well defined spectral lineshapes. Since he understood that the vibrations of electromagnetic waves and the wavelength were connected, he suggested to use the wavelength of these lineshapes to define a "universal unit of time".

With the discovery of quantum mechanics, we finally understood the nature behind Maxwell's spectral lines, as emission of photons with an energy corresponding to the difference between two quantum states of the atom. We also realized that:

1. The energy difference between two quantum states of an isolated atom is very well defined.

2. Electromagnetic waves can cause transitions between two quantum states, if the energy matches the difference.

3. The energy of electromagnetic waves and their frequency are intimately linked by Planck's constant:

$$E = h\nu. \tag{1.2}$$

Maxwell's original idea was to use the emission from an atomic transition to produce electromagnetic waves at a specific frequency. But since the emission rate is inversely proportional to the linewidth[1], a very well defined transition radiates very little power.

Instead of relying on emission, an atomic clock could be built on absorption. We could prepare the atoms in the low energy state of a given transition, and target them with coherent radiation produced by a local oscillator. This would

---

[1]The full width at half the maximum of the spectral line.

cause the atoms to become excited, with the fraction of atoms ending up in the excited state depending on how close the 'local oscillator' frequency matched the transition frequency. By detecting how many atoms ended up in the excited state we could tune our 'local oscillator' until the absorption was maximal, hereby locking the frequency of the local oscillator to the atomic transition frequency.

The advantage of using an atomic transition as a frequency reference is not only that atoms are much less sensitive to changes in the environment, compared to the previous man made clocks, but also that atoms of the same species are universally identical. This means a ceasium atom from anywhere in the universe will behave the exact same way as a ceasium atom from Africa or Antarctica.

Furthermore the transition frequencies of atomic clocks depend on the configuration and the atomic species but range from the ceasium microwave clocks to the Ag x ray clocks. Having a high clock frequency ($\nu_0$) not only allows you to split the second into smaller fractions but also decreases the fractional instability for similar uncertainties ($\delta\nu$).

The creation of a coherent local oscillator was not possible until the invention of the maser, which lead to the most famous atomic clock to date; the caesium clock. In 1967 it became the definition of SI second, the so called Primary Frequency Standard[3]:

*A second is defined as the duration of* 9 192 631 770 *periods of the radiation corresponding to the transition between the two hyperfine levels of the ground state of the caesium* 171.

In this day and age caesium fountain clocks have reached fractional stabilities of[1]:

$$\frac{\delta\nu}{\nu_0} = 10^{-16}, \tag{1.3}$$

but are only able to do so by averaging over many repeated measurements taken over a long period of time, sometimes up to 30 days. This is possible because the long term stability of the atomic transition is very good, so even if the line width is relatively wide the line center can be found with very high precision.

One of the challenges of atomic clocks is limiting the movement of the atoms to reduce the velocity dependent Doppler broadening and the interrogation time dependent Fourier broadening. The atoms cannot simply be held in a magneto-optical trap since the scattering causes decoherence which reduces the contrast of the atomic transition.

This lead to the invention of the ion clock and the lattice clock which both rely on tightly confining atoms in a specifically engineered potential which causes the first order Doppler effect to vanish completely.

The ion clocks use rf traps to confine ions which allows for very long interrogation times. However since ions interact very strongly with each other ion clocks preferably work with just a single atom at a time which puts a significant limit on the signal to noise ratio. By averaging over enough measurements this limit can be overcome and ion clocks working with the $Al^+$ ion have achieved a fractional instability of $8.6 \cdot 10^{-18}$ in just under two days[5].

The lattice clocks rely on trapping neutral atoms in a periodic potential structure created by counter propagating beams forming a standing wave. By using ultra cold fermions, the interaction between the atoms becomes very small. It is therefore possible to have many hundreds or even thousands of atoms at once which leads to very high signal to noise ratios. As each atom is confined to its own potential well a lattice clock can be thought of as hundreds of ion clocks running in parallel. Optical lattice clocks based on Sr have achieved fractional stabilities of $10^{-18}$ in two hours of averaging time[26], beating the stability of the primary frequency standard with two orders of magnitude.

The lattice however, is a double edged sword as the strong electromagnetic fields used for trapping can, and will, perturb the atomic transition through AC stark shifts. This was partly solved in 2003 when Katori, Takamoto, Palchikov and Ovsiannikov[9] suggested using a well chosen, "Magic" wavelength, which would leave the atomic transition frequency undisturbed. However, as the fractional stability of the optical lattice clocks keeps improving it becomes increasingly important to understand and characterize these tiny AC stark shifts at the level of $10^{-18}$.

## 1.2   Outline

The work in this thesis will focus on experimentally investigating and determining the lattice induced AC stark shifts in the ytterbium optical lattice clock located at the Riken Quantum Metrology Laboratory in Japan.

Chapter 2 will go through the theoretical derivation of the dipole interaction between light and atoms and how this leads to an optical lattice capable of trapping atoms. The derivation of the full light shift model from [16] will be outlined and slightly modified.

In Chapter 3 I will discuss the latest published error budget of the Riken Yb clock.

Chapter 4 will describe the experimental setup, the lasers and levels involved, and the experimental procedure of running the Riken Yb clock.

Chapter 5 will detail the data analysis, starting with the extraction of the frequency measurements of the interleaved measurement data. I will then go through the analysis of the sideband spectra used to determine the operational parameters. Finally the analysis done to characterizer the variables of the light shift model will be presented.

# The theory

Ytterbium (Yb) is a rare earth metal and the second last of the lanthanide elements with atomic number 70 and two electrons in its outermost shell. It can be regarded as a two electron atom with a charged core consisting of the atomic nucleus and 68 electrons and two valence electrons.

The energy of a free atom at rest is given by the potential energy from the Coulomb attraction between the core and the electrons. The eigenstates of such a system can be thought of as different spatial orbitals the electrons follow around the core.

The lowest energy configuration, i.e. the ground state, of Yb consists of the two electrons in the orbit closest to the core with their spins aligned anti parallel due to Pauli's exclusion principle. Using atomic term symbols this is $6s^2\ ^1S$ where the 6 represent the electrons being in the 6'th shell as the previous 5 shells are filled with the 68 other electrons and constitute part of the core.

The closest higher lying energy configurations involve a single of the two electrons in a higher energy orbital which can be further from the core ($6s7s\ ^1S$), include an angular momentum ( $6s6p\ ^1P$), have a different spin alignment ($6s6p\ ^3P$), or all of the above.

If we then include the coupling between the angular momentum of the orbit and the spin of the electrons, also called the LS coupling, the energy levels with angular momentum will split depending on $J$, the sum of the angular momentum and the total spin of the electrons:

$$J = \mathbf{L} + \mathbf{S}. \tag{2.1}$$

where $\mathbf{L}$ is the angular momentum of the level and $\mathbf{S}$ is the total spin of the two electrons. The angular momentum can either be parallel, antiparallel, or orthogonal to the total electron spin, leading to three values for $J$ if the spin of the electrons are parallel, or one value for $J$ if they are anti parallel. These two groups of states are commonly referred to as triplets and singlets.

The level structure for the first few levels of Yb have been illustrated on Figure 2.1 where we have separated the singlet states to the left and the triplet states to the right. The labels follow the standard atomic term symbol notation.
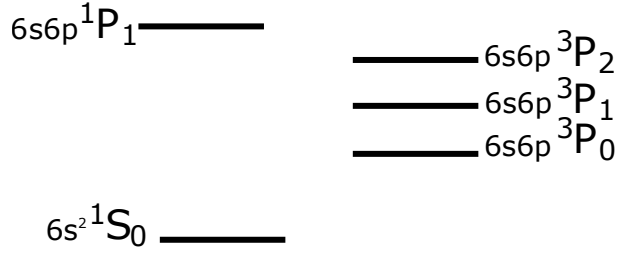
**Figure 2.1:** *The energy level diagram for Yb only illustrating the first 5 levels in the LS coupling scheme.*

In the following section we will look at how oscillating electromagnetic fields interact with atoms with such a level structure.

## 2.1   The dipole interaction

When an electric field interacts with an atom, the electrons are displaced by the electric field, and a dipole moment $\mathbf{d}$ is induced in the atom:

$$\mathbf{d} = -e\mathbf{r}, \tag{2.2}$$

where $e$ is the elementary charge, $\mathbf{r}$ is the distance from the electron to the nucleus, and $\mathbf{E}$ is the electrical field.

The energy from the induced dipole moment is described by the atom-field interaction Hamilton:

$$\mathcal{H}_{\text{AF}} = -\mathbf{d} \cdot \mathbf{E}, \tag{2.3}$$

where the factor of $\mathbf{E}$ comes from the fact that the induced dipole itself interacts with the field which induced it.

We now focus our attention on the interaction with a laser which produces an oscillating electrical field of the form:

$$E = E_0 \cos\left(\mathbf{k} \cdot \mathbf{R} - \omega t\right) \hat{\epsilon} = \frac{E_0}{2}\hat{\epsilon}\left(e^{i(\mathbf{k} \cdot \mathbf{R} - \omega t)} + e^{-i(\mathbf{k} \cdot \mathbf{R} - \omega t)}\right), \tag{2.4}$$

where $\mathbf{k}$ is the wave vector of the laser, $\mathbf{R}$ is the position of the atom, relative to the electric field, $\hat{\epsilon}$ is the polarization of the field and $\omega$ is the angular frequency of the laser. Throughout this thesis $\omega$ will always refer to angular frequency and $\nu$ always to frequency.

The dipole interaction then becomes:

$$\mathcal{H}_{\text{AF}} = -\mathbf{d} \cdot \frac{E_0}{2}\hat{\epsilon}\left(e^{i(\mathbf{k} \cdot \mathbf{R} - \omega t)} + e^{-i(\mathbf{k} \cdot \mathbf{R} - \omega t)}\right), \tag{2.5}$$

In the interaction picture, the interaction Hamilton takes the form:

$$\mathcal{H}_I = e^{i\mathcal{H}_0 \frac{t}{\hbar}}\mathcal{H}_{\text{AF}}e^{-i\mathcal{H}_0 \frac{t}{\hbar}}. \tag{2.6}$$

We then solve the time dependent Schrödinger equation in a basis of electronic eigenstates:

$$i\hbar\frac{\partial|\Psi\rangle}{\partial t} = \mathcal{H}_I|\Psi\rangle \tag{2.7}$$

$$i\hbar\sum_n \dot{a}_n|\psi_n\rangle = e^{i\mathcal{H}_0 \frac{t}{\hbar}}\left(-\mathbf{d} \cdot \mathbf{E}\right)e^{-i\mathcal{H}_0 \frac{t}{\hbar}}\sum_m a_m|\psi_m\rangle \tag{2.8}$$

and insert the electric field from Equation 2.4 while rewriting $E_n/\hbar = \omega_n$:

$$i\hbar\dot{a}_n = -\frac{E_0}{2}\sum_m e^{i\omega_n t}e^{-i\omega_m t}a_m\langle\psi_n|\mathbf{d}\cdot\hat{\epsilon}\left(e^{i(\mathbf{k}\cdot\mathbf{R}-\omega t)} + e^{-i(\mathbf{k}\cdot\mathbf{R}-\omega t)}\right)|\psi_m\rangle$$

(2.9)

We now define $\omega_n - \omega_m = \omega_{nm}$ and use the dipole approximation where the wavelength of the applied field is considered much longer than the size of the atom, such that $e^{\mathbf{k}\cdot\mathbf{R}} = 1 + i\mathbf{k}\cdot\mathbf{R}\ldots \approx 1$:

$$i\hbar\dot{a}_n = -\frac{E_0}{2}\sum_m a_m\langle\psi_n|\mathbf{d}\cdot\hat{\epsilon}|\psi_m\rangle\left(e^{i(\omega_{nm}-\omega)t} + e^{i(\omega_{nm}+\omega)t}\right).$$

(2.10)

Equation 2.10 tells us how the coefficients of the eigenstates evolve in time, such that $|a_n(t)|^2$ becomes the probability of finding the atom in state $|\psi_n\rangle$ at time $t$. In the LS coupling scheme $|\psi_n\rangle$ can be expressed by the two quantum numbers $n$ and $J$

The dipole matrix element $\langle\psi_k|\mathbf{d}\cdot\hat{\epsilon}|\psi_g\rangle$ determines the part of the transition strength which is independent from the applied field and describes the overlap between the initial state wave function $|\psi_g\rangle$ and the final state wave function $|\psi_k\rangle$.

By focusing on a two level system with only one initial state and one final state we can arrive[1] at the well known Rabi oscillations:

$$P_e(t) = |a_e(t)|^2 = \left|\frac{\Omega_{eg}}{\sqrt{\Delta^2 + \Omega^2}}\right|^2 \sin^2\left(\frac{\sqrt{\Delta^2 + \Omega^2}}{2}t\right).$$

(2.11)

where $P_e$ is the probability of finding the atom in the state $|\psi_e\rangle$, $\Delta$ is the detuning:

$$\Delta = \omega_{eg} - \omega,$$

(2.12)

and $\Omega_{eg}$ is the Rabi frequency:

$$\Omega_{eg} = -\frac{\langle\psi_e|d|\psi_g\rangle E_0}{\hbar},$$

(2.13)

While Rabi oscillations show us that the dipole interaction can cause the atom to change state if we are sufficiently close to resonance, there still are some limitations. If we insert the definition of the dipole momentum into the dipole matrix element we get:

$$\langle\psi_n| - e\mathbf{r}\cdot\hat{\epsilon}|\psi_g\rangle.$$

(2.14)

Because $r$ is odd, transitions between states with the same parity cannot happen. Furthermore, because the dipole interaction couples the position of the electron with the electromagnetic field, there is no effect that will cause the spin of the electron to change. As a consequence dipole interactions cannot cause transitions between singlet and triplet states.

Transitions that violate these rules still happen for two electron atoms since the eigenstates are in fact not true eigenstates[8]. The state $^3P_1$ has a tiny admixture of $^1P_1$ and $^3P_0$ a tiny admixture of $^3P_1$ which causes the transitions

---

[1]See Appendix A for a full derivation

to happen, but at a much lower rate. This is one of the reasons why Yb is a good candidate for clock operation since it makes the line width of the clock transition $^1S_0 \leftrightarrow {}^3P_0$ only $\sim 50$ ms[18] which is very narrow.

One other advantage of Yb is that the energy difference between the ground state and the first few excited states is small enough to be targeted by lasers in the optical regime. The reason for this is that the two valence electrons are bound very weakly because of the screening of the 68 other electrons.

Moving away from Rabi oscillations which only considered one possible final states, we can now include all final states if we assume the laser is far detuned from all of them. In this case the atom never leaves the ground state and we can treat the dipole interaction as a perturbation.[2] The interaction then turns out to be governed by the polarizability:

$$\mathbf{d} = \alpha(\omega)\mathbf{E} \tag{2.15}$$

where $\alpha$ is the polarizability:

$$\alpha(\omega) = \sum_n \frac{2}{\hbar} \frac{\omega_{ng}\langle\psi_n|\mathbf{d}|\psi_g\rangle\langle\psi_g|\mathbf{d}|\psi_n\rangle}{\omega_{ng}^2 - \omega^2 - i\omega_{ng}\gamma_n}, \tag{2.16}$$

and $\gamma_n$ is the natural line width of the state $|\psi_n\rangle$.

If we then look at the dipole interaction Hamiltonian again:

$$\mathcal{H}_{\mathrm{AF}} = -\mathbf{d}\cdot\mathbf{E} = -\alpha\mathbf{E}\cdot\mathbf{E}, \tag{2.17}$$

we see that the polarizability describes how much the energy levels of the atom get perturbed by an oscillating electrical field if the field is far from any resonances, and is also called the AC stark shift.

One of the differences between Rabi oscillation and the AC stark shift is that the former changes the state of the atom while the latter does not.

### 2.1.1   The Dipole force

Since $\mathcal{H}_{\mathrm{AF}}$ represents the potential energy of the dipole interaction, any gradient will result in a force:

$$\begin{aligned}\mathbf{F}_{\mathrm{Dipole}} &= -\nabla - \mathbf{d}\cdot\mathbf{E} \\ &= \alpha\nabla\mathbf{I}.\end{aligned} \tag{2.18}$$

In our case the electrical fields applied by lasers always have gradients because the laser intensity has a transversal intensity distribution. This leads to the atoms being pushed either to the center or away from the center depending on the sign of $\alpha$.

The polarizability of the ground state of Yb has been plotted in Figure 2.2 where the peaks correspond to resonances at 399 nm and 556 nm arising from transitions between the states $6s^2\ {}^1S_0 \leftrightarrow 6s6p\ {}^1P_1$ and $6s^2\ {}^1S_0 \leftrightarrow 6s6p\ {}^3P_1$ respectively.

To trap an atom, we must apply a laser with a frequency such that $\alpha$ is positive which will cause atoms to be pushed towards the intensity maximum.

---

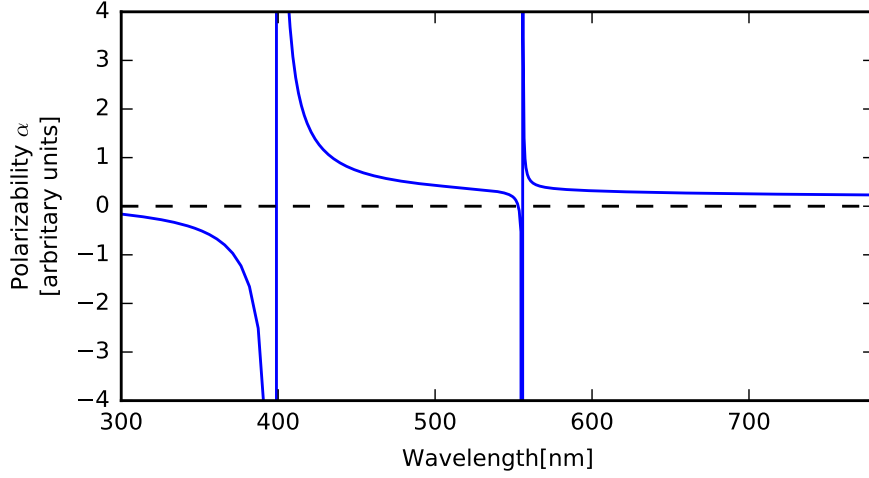[2]See Appendix B for a full derivation.

**Figure 2.2:** *A plot of the polarizability of the ground state of Yb with resonances at 399 nm and 556 nm.*

This is called the dipole trap and has been used to confine atoms in many different applications. Trapping can also be done at a frequency where $\alpha$ is negative where one technique is to use multiple laser beams to surround the trap center and act as optical walls.

## 2.2 Optical lattice trap

In an optical lattice clock, a standing wave is used to confine the atoms. If we assume a standing wave generated by laser of intensity $I = \frac{1}{2}c\epsilon_0 E_0^2$, then the electrical field is given as:

$$E = 2\sqrt{\frac{1}{2}c\epsilon_0}\, E_0 \cos(kz)\sin(\omega t), \tag{2.19}$$

where $E_0$ is the amplitude of the running wave laser, $z$ is the position along the z axis, and $k$ is the wave vector given as $k = {}^{2\pi}/_\lambda$.

We can now focus on the spatial part of the electrical field by looking at the time average. Equation 2.17 then gives us the potential:

$$\begin{aligned}
V_{\text{dipole}} &= -\alpha \mathbf{E}^2 \\
&= -\alpha 4 I_0 \cos^2(kz) \\
&= -U_{\text{trap}} \cos^2\left(kz\right). \tag{2.20}
\end{aligned}$$

This potential has a minimum when $z = 0$ or $z = \frac{2n}{4}\lambda$ with a depth of $U_{\text{trap}}$.

The spatial intensity distribution has been illustrated on Figure 2.3a, which also shows the electrical field (Figure 2.3b) and the dipole potential (Figure 2.3c) for a positive $\alpha$ value. The name lattice comes from the fact that all the potential wells are identical, creating a periodic structure similar to a crystal lattice.
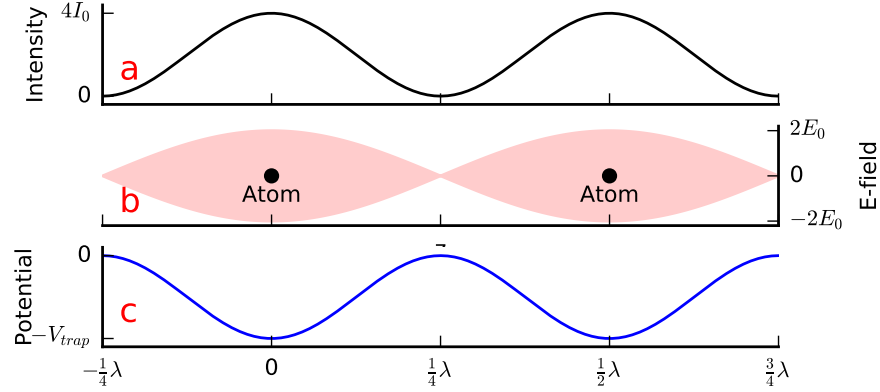
**Figure 2.3:** *An illustration of the peak intensity (a), the electrical field (b) and the dipole potential (c) for a positive $\alpha$. In (b) the shaded area represents the full modulation of the electrical field. Potential in (c) should be $-U$trap.*

Since all the wells are identical, we can focus, without a loss of generality, on just a single one, with just a single atom. We can do a Taylor expansion of the potential around the minimum at $z = 0$:

$$V_{\text{dipole}} \approx -U_{\text{trap}}\Bigg[ \cos^2{(k \cdot 0)} - \sin{(2k \cdot 0)}\, k(z - 0)$$

$$-\frac{1}{2}\cos{(2k \cdot 0)}\, 2k^2(z-0)^2$$

$$+\frac{1}{6}\sin{(2k \cdot 0)}\, 4k^3(z-0)^3$$

$$+\frac{1}{24}\cos{(2k \cdot 0)}\, 8k^4(z-0)^4 + \ldots \Bigg]$$

$$V_{\text{dipole}} \approx -U_{\text{trap}}\left[1 - k^2 z^2 + \frac{1}{3}k^4 z^4 + \mathcal{O}(z^{2n})\right] \tag{2.21}$$

This potential is very similar to the harmonic oscillator potential with an anharmonic correction:

$$V_{\text{dipole}} = -U_{\text{trap}} + \frac{1}{2}m_{\text{atom}}\omega_T^2 z^2 - U_{\text{trap}}\frac{1}{3}k^4 z^4, \tag{2.22}$$

where we have thrown away higher orders of the anharmonic correction and only kept the first. The offset is the AC stark shift and is thus proportional to the polarizability and the harmonic part represents the kinetic energy of the atom while the anharmonic is a correction to the kinetic energy.

We can now identify the characteristic oscillation frequency of the trap $\omega_T$:

$$\omega_T = \sqrt{\frac{2k^2}{m_{\text{atom}}}U_{\text{trap}}} = 2\sqrt{\frac{E_{\text{recoil}}}{\hbar}\frac{U_{\text{trap}}}{\hbar}}, \tag{2.23}$$

where we have further rewritten it by using the recoil energy, which is the kinetic energy a stationary atom gains by emitting a trapping laser photon:

$$E_{\text{recoil}} = \frac{p^2}{2m_{\text{atom}}} = \frac{\hbar^2 k^2}{2m_{\text{atom}}}. \tag{2.24}$$

The interaction Hamiltonian for an atom trapped in such a potential then takes the form:

$$\mathcal{H}_{\text{AF}} = -U_{\text{trap}} + \frac{1}{2} m_{\text{atom}} \omega_T^2 z^2 - U_{\text{trap}} \frac{1}{3} k^4 z^4, \tag{2.25}$$

The stationary eigenstates to this Hamiltonian represents the trapped atoms vibrational motion and has the energies:

$$E = - \overset{\text{AC stark shift}}{E_{\text{trap}}} + \overset{\text{Harm Osc}}{E_n} - \overset{\text{Correction}}{E_{\text{anh}}}, \tag{2.26}$$

where we know the energies of the harmonic oscillator:

$$E_n = \hbar \omega_T \left( \frac{1}{2} + n \right), \tag{2.27}$$

The anharmonic energies can be found by using perturbation theory:

$$E_{\text{anh}} = U_{\text{trap}} \frac{1}{3} k^4 \frac{3}{2} \left( n^2 + n + \frac{1}{2} \right) \frac{\hbar^2}{m_{\text{atom}}^2 \omega_T^2}$$
$$= \frac{E_{\text{recoil}}}{2} \left( n^2 + n + \frac{1}{2} \right) \tag{2.28}$$

The anharmonic correction has the opposite sign of the oscillator energy so it pulls the higher lying energy levels closer together. This has been illustrated on Figure 2.4 where the vibrational energies with and without corrections have been plotted in the left and right well respectively. The approximation with an harmonic oscillator and an anharmonic correction is only good for the few lowest energy levels. For higher lying energy levels we should include more than just the first order anharmonic correction.
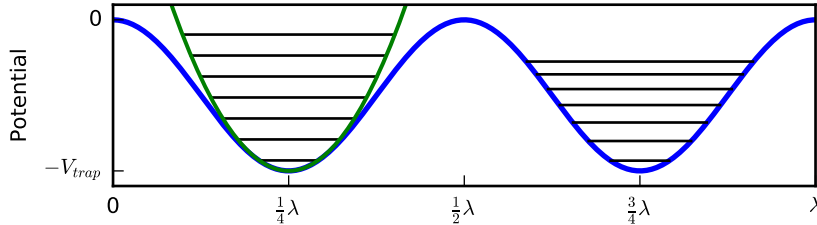


**Figure 2.4:** *The blue line is the $\cos^2$ potential, and the green is the harmonic oscillator approximation without the anharmonic correction. The first 7 levels are illustrated for the harmonic approximation, with and without the anharmonic correction, in the left and right well respectively.*

### 2.2.1 Probing a trapped atom

The full advantage of trapping an atom in a lattice is revealed if we imagine doing spectroscopy with a second laser which we will call the probe laser. The full system Hamiltonian for an atom in a trap and getting probed by a second laser can then be written as:

$$\mathcal{H} = \mathcal{H}_0 + \left( -U_{\text{trap}} + \frac{1}{2} m_{\text{atom}} \omega_T^2 z^2 - U_{\text{trap}} \frac{1}{3} k^4 z^4 \right) + \mathcal{H}_{\text{AF}}, \tag{2.29}$$

where $\mathcal{H}_0$ is the Hamiltonian describing the electronic configuration and $\mathcal{H}_{\mathrm{AF}}$ is the new interaction Hamiltonian describing the interaction of a trapped atom with a probe laser.

The eigenstates to $\mathcal{H}$ can be factorized into two independent parts, one dealing with the 'internal' electron configuration, and one dealing with the 'vibrational' motion of the atomL

$$|\Psi\rangle = |\Psi\rangle^{(int)} \otimes |\Psi\rangle^{(vib)}$$
$$= \sum_{m,n} a_m a_n |\psi_m^{(int)}, n\rangle. \tag{2.30}$$

where $n$ is the quantum number for the vibrational levels.

The interaction between the trapped atom and the probe laser is then:

$$\mathcal{H}_{\mathrm{AF}} = -\mathbf{d} \cdot \hat{\epsilon} E_{0_p} \cos\left(\mathbf{k}_p \cdot \mathbf{R} - \omega_p t\right), \tag{2.31}$$

with the subscript $p$ denoting the probe laser.

The two major differences between the probe and the trapping laser is that the probe is close to resonance and not a standing wave. We can then calculate the interaction with the probe like we did with the free atom except now our basis of eigenstates consist of both the internal and vibrational parts.

Like before the frequency independent strength of a transition from one electronic state to another, and from one vibrational state to another is determined by the dipole matrix element:

$$\langle \psi_g, n' | \mathbf{d} \cdot \hat{\epsilon} e^{i\mathbf{k}_p \cdot \mathbf{R}} | \psi_e, n \rangle. \tag{2.32}$$

This time we have not used the dipole approximation yet. This is because while the size of the atom is still much smaller than the wavelength of the probe, the vibrational motion of the atom is not. On the other hand the vibrational states do not interact with the electron or the dipole operator. Therefore the dipole matrix element factorizes into two parts:

$$\langle \psi_g | \mathbf{d} \cdot \hat{\epsilon} | \psi_e \rangle \langle n' | e^{i\mathbf{k}_p \cdot \mathbf{R}} | n \rangle. \tag{2.33}$$

The first factor is the same as in the free atom case, so we will focus on the second factor.

For a probe beam aligned parallel to the trap laser, and hence parallel to the direction of vibration, the position operator takes the form:

$$\mathbf{k}_p \cdot \mathbf{R} = k_p \tilde{z} = k_p \sqrt{\frac{\hbar}{2m_{\mathrm{atom}}\omega_T}} \left(a^\dagger + a\right). \tag{2.34}$$

where $a^\dagger$ and $a$ are the normal ladder operators. The product $k_p \sqrt{\frac{\hbar}{2m_{\mathrm{atom}}\omega_T}}$ is also called the Lamb-Dicke parameter $\eta$:

$$\eta = \sqrt{\frac{k_p^2 \hbar}{2m_{\mathrm{atom}}\omega_T}} = \sqrt{\frac{E_{\mathrm{recoil}}^p}{\hbar\omega_T}}, \tag{2.35}$$

where the recoil energy is now that of the probe laser, and not of the lattice laser.

The matrix element is now:

$$\langle n' | e^{i\eta\left(a^\dagger + a\right)} | n \rangle, \tag{2.36}$$

which can be solved by following the steps in [27] from eq (30) to eq (32), making use of the identity $e^{a+b} = e^{a^\dagger} e^a e^{-\frac{1}{2}[a^\dagger, a]}$:

$$\langle n'|e^{i\eta(a^\dagger + a)}|n\rangle = e^{-\frac{1}{2}\eta^2} \sqrt{\frac{n_<!}{(n_< + \Delta n)!}} \, (i\eta)^{\Delta n} L_{n_<}^{\Delta n}\left(\eta^2\right). \qquad (2.37)$$

Here $\Delta n = |n' - n|$, $n_<$ is the smallest of $n$ and $n'$ and $L_{n_<}^{\Delta n}\left(\eta^2\right)$ is the generalized Laguerre polynomial. A plot of Equation 2.37 for $\Delta n = 0, 1, 2$ and $n_< = 0, 1, 2$ can be seen on Figure 2.5 as a function of $\eta$. We see that the matrix elements involving no change in vibrational level are generally much stronger than when $\Delta n \neq 0$ especially for small $\eta$. This effect is furthermore increased for lower $n_<$.
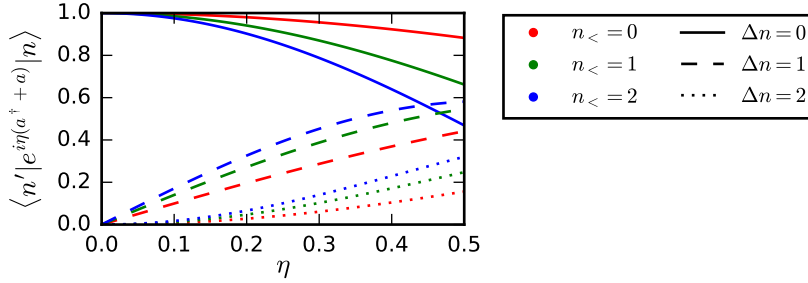


**Figure 2.5:** *A plot of Equation 2.37 for three values of $n_<$ and three values of $\Delta n$ as a function of the Lamb Dicke parameter $\eta$.*

In our setup the clock transition is 578 nm and we use the 171 isotope of Yb with a mass of 170.9 u. This leads to a recoil energy of:

$$E_{\text{recoil}}^p = h \cdot 3.494 \text{ kHz}. \qquad (2.38)$$

Our typical trap frequencies range from $2\pi \cdot 25$ kHz to $2\pi \cdot 120$ kHz which leads to small Lamb-Dicke parameters:

$$\eta < \sqrt{\frac{3.494 \text{ kHz}}{25 \text{ kHz}}} = 0.37. \qquad (2.39)$$

meaning we are in the Lamb-Dicke regime where $\eta \ll 1$. In this regime any transitions involving changes in vibrational level ($\Delta n \neq 0$) will be suppressed compared to those that do not ($\Delta n = 0$).

The energy difference between the electronic eigenstates is $\sim 10^{15}$ Hz, whereas the difference in vibrational states is typically, for our experiments, in the range of $10^4 - 10^5$ Hz, but depends on the trap depth as seen by combining Equation 2.23 with Equation 2.27.

Since the energy separation of the harmonic levels is inaccessible with a laser, they are instead excited by detuning the laser slightly from an electronic transition, called the carrier, and used to excite both an electronic and a vibrational transition simultaneously, called a sideband.

If the line width of the electronic excitation is smaller than the trap frequency $\omega_T$, then we are able to resolve the sidebands in the spectrum as seen on Figure 2.6 and Figure 2.7 for atoms starting in $n = 1$ .

The lower height of the sidebands compared to the carrier is due to the matrix element in Equation 2.37 as seen as the difference between the solid and dashed lines in Figure 2.5. The red sideband is lower than the blue sideband because going from $n = 0 \rightarrow 1$ has smaller matrix element than $n = 1 \rightarrow 2$ as $n_<$ is smaller. This is also visible in Figure 2.5 as the difference between the blue dashed and the red dashed lines.

The inwards shifts of the blue and red sideband is because of the anharmonic correction. It reduces the energy gap between two adjacent levels by $nE_{\text{recoil}}$ where $n$ is the highest level involved, thus moving the blue sideband slightly more inwards than the red.

Being in the Lamb-Dicke regime makes it possible to do Doppler free spectroscopy since the motion of the atom, which is quantized in the vibrational levels, does not change the transition frequency of the carrier. Furthermore, because the trap frequency, and thus the motional level spacing, is much larger than the recoil energy, the atom cannot gain any momentum by interacting with photons. The momentum is instead absorbed by the lattice and allows for recoil free spectroscopy.
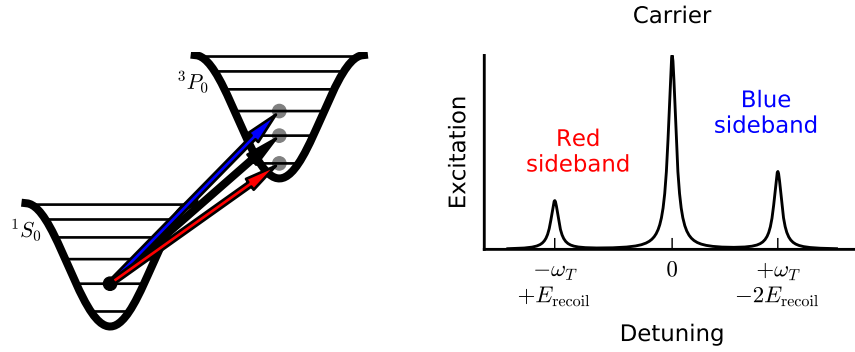


**Figure 2.6:** *An illustration of excitation of the atom in an optical lattice well. The atom starts in $n = 1$ and can be excited to three different final vibrational states depending on the frequency of the laser.*

**Figure 2.7:** *Spectrum of the sideband excitation for an atom starting in $n = 1$.*

### 2.2.2  Not a perfect world

Up until now we have only focused on the trapping along the axis parallel to the lattice laser, also called the axial direction. But a single, standing wave beam will not only trap an atom in the axial direction, but also in the two others due to the transversal Gaussian intensity distribution. The two transversal axis can be treated identically due to symmetry and are collectively referred to as the radial directions.

The axial trap is much smaller, since the lattice confines atoms to less that $\frac{\lambda}{2}$, whereas the radial confinement is limited by the beam diameter, typically being on the order of microns:

$$V_{\text{dipole}} = -\alpha 4 I(z,r)$$

$$= -\alpha 4 I_0 \cos^2(kz) e^{-\frac{2r^2}{\text{w}_0^2}} \tag{2.40}$$

$$= -U_{\text{trap}} \cos^2(kz) e^{-\frac{2r^2}{\text{w}_0^2}}. \tag{2.41}$$

Here $r$ is the radial distance from the beam center and $\text{w}_0$ is the beam waist. We can imagine that the beam waist overlaps perfectly with the center of a lattice site and do a Taylor expansion to second order around the beam center $r = 0$:

$$V_{\text{dipole}} = -U_{\text{trap}} e^{-\frac{2r^2}{\text{w}_0^2}}$$

$$\overset{Taylor}{\approx} -U_{\text{trap}} \left( 1 - \frac{4}{\text{w}_0^2} r^2 \right) \tag{2.42}$$

which leads to a radial trap frequency given as:

$$\omega_T^{\text{radial}} = \sqrt{\frac{8 U_{\text{trap}}}{m_{\text{atom}} \text{w}_0^2}}. \tag{2.43}$$

Since the beam waist is typically on the order of tens of microns, and the trapping wavelength hundreds of nanometers, the radial trap frequency will two to three orders of magnitude smaller than the axial trap frequency.

Looking in the axial direction the atom will therefore see a slowly changing 'instantaneous' trap depth as it moves radially in the trap. The instantaneous trap depth is always equal or smaller than the 'full' trap depth which is the depth at the center of the beam. This is illustrated in Figure 2.8 where the colored slices represent the 'instantaneous' axial trapping potential at different points in the radial motion.

## 2.3  The light shift model

From the previous section we learned that an atom can be trapped in a standing wave in order to do Doppler and recoil free spectroscopy. A couple of other advantages of the optical lattice is that many atoms can be probed simultaneously and with long interrogation times, both with are very beneficial to clock operation. Unfortunately the optical lattice it brings its own cohort of problems.
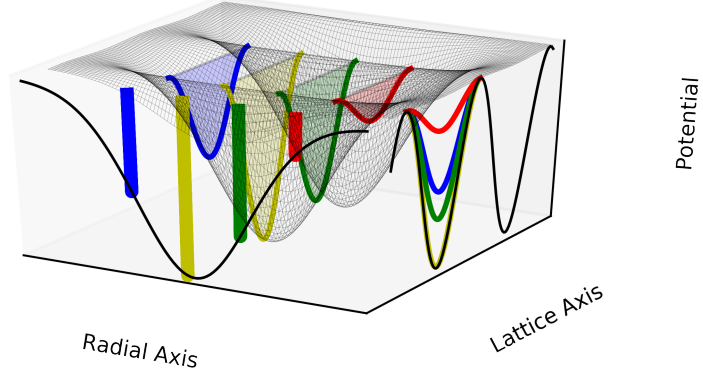
**Figure 2.8:** *The radial axis is a Gaussian potential, and the lattice axis is a $cos^2$. The colored slices illustrates the instantaneous trap depth the atoms feels at different radial positions in the trap.*

The main idea of using atomic clocks is that the electronic transition energy is well defined and constant in time. The lattice, however, creates an AC stark shift of the ground and excited state, which leads to a shift in the transition energy. We can see that by writing up the energy difference between the excited (e) and ground (g) states:

$$\Delta E_{\text{clock}} = \overset{\text{Electronic}}{\left(E_0^{(e)} - E_0^{(g)}\right)} - \overset{\text{AC stark shift}}{\left(E_{\text{trap}}^{(e)} - E_{\text{trap}}^{(g)}\right)} + \overset{\text{Harmonic}}{\left(E_n^{(e)} - E_n^{(g)}\right)} - \overset{\text{Anharmonic}}{\left(E_{anh}^{(e)} - E_{anh}^{(g)}\right)}.$$
$$(2.44)$$

We must therefore determine and correct our measurements for the contributions from the lattice induced shifts:

$$\Delta E_{\text{clock}}^{\text{lattice}} = -\Delta U_{\text{trap}} + \hbar \Delta \omega_T \left(\frac{1}{2} + n\right) - \left[\frac{E_{\text{recoil}}}{2}\left(n^2 + n + \frac{1}{2}\right) - \frac{E_{\text{recoil}}}{2}\left(n^2 + n + \frac{1}{2}\right)\right].$$
$$(2.45)$$

We then use Equation 2.23 to express the trap frequency in terms of trap depth:

$$\Delta E_{\text{clock}}^{\text{lattice}} = -\Delta U_{\text{trap}} + 2\sqrt{E_{\text{recoil}}\Delta U_{\text{trap}}}\left(\frac{1}{2} + n\right), \tag{2.46}$$

And use the fact that $U_{\text{trap}} = \alpha I$:

$$\Delta E_{\text{clock}}^{\text{lattice}} = -I\left(\alpha^{(e)} - \alpha^{(g)}\right) + 2\sqrt{E_{\text{recoil}}I}\left(\sqrt{\alpha^{(e)}} - \sqrt{\alpha^{(g)}}\right)\left(\frac{1}{2} + n\right), \tag{2.47}$$

where $I$ is the intensity of the standing wave, thus making the clock transition frequency dependent on the intensity of the lattice laser. Any fluctuations

in lattice laser intensity will then result in fluctuations in the measured clock transition.

An elegant solution to this problem was proposed in 2003[9] and implemented later the same year [25] with strontium-87 (Sr). The idea was to find a wavelength, coined the "magic wavelength", where the polarizability of the ground state was equal to the polarizability of the excited state, effectively making the differential light shift disappear completely. The plot from the original article[9] is shown in Figure 2.9, where the AC stark shift, i.e. the dipole potential is plotted for the ground and excited state of the $^1S_0 \leftrightarrow {}^3P_0$ clock transition. Note that the polarizabilities must not only be equal but also positive[3].
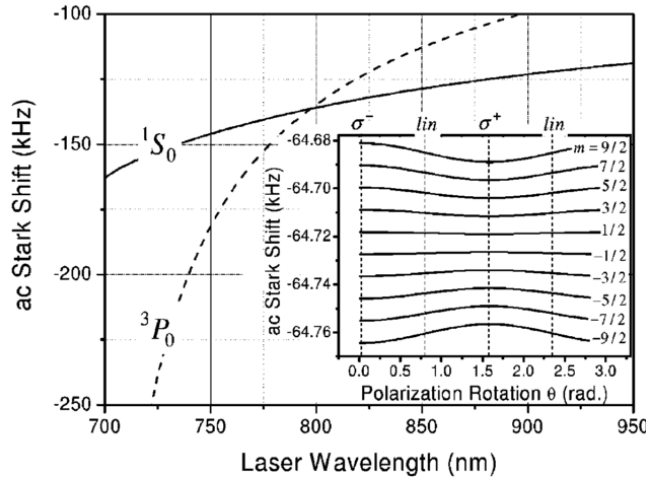


**Figure 2.9:** *The original plot from the article[9] proposing the magic wavelength scheme. The interesting point is the crossing of the stark shift for the $^1S_0$ and $^3P_0$ state.*

### 2.3.1 The full light shift model

While Equation 2.47 is a good start, it is only an approximation as it only considers electric dipole interactions.

The next step is to include the two-photon interaction and the magnetic dipole and electric quadrupole interactions. To do that, we follow the derivations of [16]:

From the dipole interaction Hamiltonian in Equation 2.17, with a standing electrical field, we saw that:

$$V_{\text{dipole}}^{\text{E1}} = -\alpha I \cos^2 (kz) = -\alpha^{E1} I \cos^2 (kz), \qquad (2.48)$$

which we have relabeled to remember that it stems from the electric dipole (E1) interaction. The magic wavelength for Ytterbium is known, both from experimental observations and theoretical calculations to be around 759 nm[10,

---

[3]A positive polarizability will lead to a negative AC stark shift, in accordance with Figure 2.9.

7]. This is very close to three two photon transitions [2] which means we must include the two-photon interaction even though it is normally very weak:

$$V_{2\text{photon}} = -\beta I^2 \cos^4(kz),\tag{2.49}$$

since it depends on the interaction with two photons and not only one.

The magnetic dipole interaction is proportional to the magnetic field, which is a quarter out of phase from the electric field:

$$V_{\text{Mag dipole}} = -\alpha^{M1} I \sin^2(kz),\tag{2.50}$$

where we have included all conversion factors between $E_0$ and $B_0$ in $\alpha^{M1}$.

The electric quadrupole interaction is proportional to the gradient of the electric field, so it must also be out of phase:

$$V_{\text{El quad}} = -\alpha^{E2} I \sin^2(kz).\tag{2.51}$$

Now we group all these together, and do a Taylor expansion around $z = 0$ as before:

$$\begin{aligned}
V_{\text{Lattice}} = &- \left[\alpha^{E1}\cos^2(kz) + \left(\alpha^{E2} + \alpha^{M1}\right)\sin^2(kz)\right] I - \beta\cos^4(kz) I^2 \\
\approx &- \alpha^{E1} I - \beta I^2 \\
&+ \left[\left(\alpha^{E1} - \alpha^{M1} - \alpha^{E2}\right) I + 2\beta I^2\right] k^2 z^2 \\
&- \left[\left(\alpha^{E1} - \alpha^{M1} - \alpha^{E2}\right) I + 5\beta I^2\right]\frac{k^4}{3}z^4.
\end{aligned}\tag{2.52}$$

Seeing the parallels to Equation 2.21, we recognize the first two terms as the depth of the potential well and the next term as the harmonic oscillator, with the third term being the first order anharmonic correction. The axial trap frequency is now given as:

$$\omega_T = 2\sqrt{\frac{E_{\text{recoil}}}{\hbar^2}}\sqrt{\left(\alpha^{E1} - \alpha^{M1} - \alpha^{E2}\right) I + 2\beta I^2}.\tag{2.53}$$

and the anharmonic correction energy:

$$E_{\text{anh}} = \left[\left(\alpha^{E1} - \alpha^{M1} - \alpha^{E2}\right) I + 5\beta I^2\right]\frac{1}{2}k^4\left(n^2 + n + \frac{1}{2}\right)\frac{\hbar^2}{m_{\text{atom}}^2\omega_T^2}\tag{2.54}$$

Using Equation 2.53 and $E_{\text{recoil}} = \frac{\hbar^2 k^2}{2m_{\text{atom}}}$ we can rewrite this to:

$$\begin{aligned}
E_{\text{anh}} &= \frac{E_{\text{recoil}}}{2}\left(\frac{1 + 5\frac{\beta I}{\alpha^{E1} - \alpha^{M1} - \alpha^{E2}}}{1 + 2\frac{\beta I}{\alpha^{E1} - \alpha^{M1} - \alpha^{E2}}}\right)\left(n^2 + n + \frac{1}{2}\right) \\
&= \frac{E_{\text{recoil}}}{2}\left(1 + 3\frac{\beta}{\alpha^{E1} - \alpha^{M1} - \alpha^{E2}}I\right)\left(n^2 + n + \frac{1}{2}\right).
\end{aligned}\tag{2.55}$$

To get to the last line, we have used a Taylor approximation around zero in $\frac{\beta}{\alpha^{E1} - \alpha^{M1} - \alpha^{E2}}$ since the electric dipole polarizability is roughly $10^6$ times larger than the others: $\alpha^{E1} \ggg \alpha^{M1}, \alpha^{E2}, \beta$.

The energy of the atom, due to the lattice interactions, can then be written as:

$$E_{\text{clock}}^{\text{Lattice}} = -\overbrace{D}^{\alpha^{E1}I + \beta I^2} + \omega_T\left(\frac{1}{2} + n\right) - E_{\text{anh}}\left(n^2 + n + \frac{1}{2}\right),\tag{2.56}$$

We now once again look at the clock energy difference $\Delta E_{\text{clock}}^{\text{Lattice}}$, and group the terms in powers of $I$:

$$\Delta E_{\text{clock}}^{\text{Lattice}} = \sqrt{E_{\text{recoil}}} \left( \sqrt{\alpha^{E1(e)} - \alpha^{M1(e)} - \alpha^{E2(e)}} - \sqrt{\alpha^{E1(g)} - \alpha^{M1(g)} - \alpha^{E2(g)}} \right) (2n+1) \cdot I^{1/2}$$

$$+ \left( - \left[ \alpha^{E1(e)} - \alpha^{E1(g)} \right] \right.$$

$$\left. - \frac{3E_{\text{recoil}}}{4} \left( \frac{\beta^{(e)}}{\alpha^{E1(e)} - \alpha^{M1(e)} - \alpha^{E2(e)}} - \frac{\beta^{(g)}}{\alpha^{E1(g)} - \alpha^{M1(g)} - \alpha^{E2(g)}} \right) (2n^2 + 2n + 1) \right) \cdot I$$

$$+ \sqrt{E_{\text{recoil}}} \left( \frac{\beta^{(e)}}{\sqrt{\alpha^{E1(e)} - \alpha^{M1(e)} - \alpha^{E2(e)}}} - \frac{\beta^{(g)}}{\sqrt{\alpha^{E1(g)} - \alpha^{M1(g)} - \alpha^{E2(g)}}} \right) (2n+1) \cdot I^{3/2}$$

$$- \left[ \beta^{(e)} - \beta^{(g)} \right] \cdot I^2, \tag{2.57}$$

We now consider the case where we are at the magic wavelength, such that $\alpha^{E1(e)} \approx \alpha^{E1(g)}$. Still following [16] we make a series of clever rewrites, using again the large magnitude difference of $\alpha^{E1}, \alpha^{M2}$, and $\beta$, which reduces Equation 2.57 to:

$$\Delta E_{\text{clock}}^{\text{Lattice}} = - \left[ \overset{<<0}{\Delta \alpha^{E1}} - \left( \Delta \alpha^{M1} + \Delta \alpha^{E2} \right) \right] \sqrt{\frac{E_{\text{recoil}}}{\alpha^{E1}}} (n + {}^1\!/\!{}_2) \cdot I^{1/2}$$

$$- \left[ \overset{<<0}{\Delta \alpha^{E1}} + \Delta \beta \frac{3E_{\text{recoil}}}{4\alpha^{E1}} (2n^2 + 2n + 1) \right] \cdot I$$

$$+ \Delta \beta \sqrt{\frac{E_{\text{recoil}}}{\alpha^{E1}}} (2n+1) \cdot I^{3/2}$$

$$- \Delta \beta \cdot I^2. \tag{2.58}$$

Here we have assumed that $\Delta \alpha^{E1}$ is not completely zero for reasons that will be clear in a moment.

The first thing to notice about Equation 2.58 is, that there is no way to make everything cancel out. In order to minimize the light shifts we can consider the case where we have detuned the lattice frequency slightly from the magic wavelength:

$$\Delta \alpha^{E1} = \frac{\partial \Delta \alpha^{E1}}{\partial \omega} \left( \omega_{\text{lattice}} - \omega_{\text{E1}} \right), \tag{2.59}$$

where $\omega_{\text{lattice}}$ is the frequency of the lattice laser and $\omega_{\text{E1}}$ is the E1 magic wavelength.

Plugging this in leads to:

$$\Delta E_{\text{clock}}^{\text{Lattice}} = \left( \frac{\partial \Delta \alpha^{E1}}{\partial \omega} \left( \omega_{\text{lattice}} - \omega_{\text{E1}} \right) - \left( \Delta \alpha^{M1} + \Delta \alpha^{E2} \right) \right) \sqrt{\frac{E_{\text{recoil}}}{\alpha^{E1}}} (n + {}^1\!/\!{}_2) \cdot I^{1/2}$$

$$- \left( \frac{\partial \Delta \alpha^{E1}}{\partial \omega} \left( \omega_{\text{lattice}} - \omega_{\text{E1}} \right) - \Delta \beta \frac{3E_{\text{recoil}}}{4\alpha^{E1}} (2n^2 + 2n + 1) \right) \cdot I$$

$$+ \Delta \beta \sqrt{\frac{E_{\text{recoil}}}{\alpha^{E1}}} (2n+1) \cdot I^{3/2}$$

$$- \Delta \beta \cdot I^2. \tag{2.60}$$

where we see we can choose the lattice wavelength such that it either cancels the $\propto \sqrt{I}$ contribution or $\propto I$ contribution.

We have, in principle, all we need now, but to make it slightly more useful for us, we wish to parameterize it in some quantities we can easily determine experimentally. Recalling from from the first line of Equation 2.52 that the trap depth is given as $D = \alpha^{E1}I + \beta I^2$, and because $\beta$ is negligible compared to $\alpha^{E1}$, we can approximate the intensity in terms of the trap depth:

$$D = U_{\text{trap}} \approx \alpha^{E1}I \tag{2.61}$$

and reduce Equation 2.60 to:

$$\begin{aligned}
\Delta\nu_{\text{clock}}^{\text{lattice}} = {} & \left(a\left(\nu_{\text{lattice}} - \nu_{\text{E1}}\right) - b\right)\left(n + {}^{1}\!/{}_{2}\right)\sqrt{\frac{U_{\text{trap}}}{E_{\text{recoil}}}} \\
& - \left(a\left(\nu_{\text{lattice}} - \nu_{\text{E1}}\right) - \frac{3}{4}d(2n^2 + 2n + 1)\right)\frac{U_{\text{trap}}}{E_{\text{recoil}}} \\
& + d(2n + 1)\left(\frac{U_{\text{trap}}}{E_{\text{recoil}}}\right)^{3/2} \\
& - d\left(\frac{U_{\text{trap}}}{E_{\text{recoil}}}\right)^2,
\end{aligned} \tag{2.62}$$

where we have divided everything by planck's constant $h$ to convert the energy shift to frequency which is what we measure in the lab. We then converted the angular frequencies to frequencies and collected many of the constants in a,b, and d:

$$\begin{aligned}
a &= \frac{1}{h}\frac{\partial\Delta\alpha^{E1}}{\partial\nu}\frac{E_{\text{recoil}}}{\alpha^{E1}} \\
b &= \frac{1}{h}\left(\Delta\alpha^{M1} + \Delta\alpha^{E2}\right)\frac{E_{\text{recoil}}}{\alpha^{E1}} \\
d &= \frac{1}{h}\Delta\beta\left(\frac{E_{\text{recoil}}}{\alpha^{E1}}\right)^2.
\end{aligned} \tag{2.63}$$

Note that the recoil energy used here is not the recoil energy of the probe laser as in the previous section, but rather the recoil energy of the lattice laser:

$$E_{\text{recoil}} = h \cdot 2.026 \text{ kHz.} \tag{2.64}$$

$a$ now describes the slope of the the differential electric dipole polarizability $\Delta\alpha^{\text{E1}}$ close to the magic frequency $\nu_{\text{E1}}$. $b$ is related to the differential magnetic dipole polarizability and the electric quadrupole polarizability, and $d$ is related to the differential hyperpolarizability arising from the two photon electric dipole interactions.

The trap depth in Equation 2.62 is not the full trap depth of the potential, but rather the instantaneous axial trap depth the atom experiences which, as explained in Section 2.2.2, depends on the radial position of the atoms.

Under normal operating conditions the interrogation period is long enough for the atoms to oscillate significantly in the radial directions, leading to the atoms experiencing a light shift which varies in time. Any observed light shift

will therefore be an average over the radial motion and we must therefore modify Equation 2.62 to deal with the average axial trap depth experienced by the atoms.

We do this by modeling the average trap depth as a fraction of the full trap depth $U_{\text{trap}}^0$:

$$\frac{\langle U_{\text{trap}} \rangle}{U_{\text{trap}}^0} = \zeta$$

$$\langle U_{\text{trap}} \rangle = \zeta U_{\text{trap}}^0 \tag{2.65}$$

Here $U_{\text{trap}}^0$ is the full trap depth, i.e. the axial trap depth at the center of the beam and therefore only depends on the lattice laser intensity, while $\zeta$ is called the intensity reduction parameter.

Because the light shift model is non linear in axial trap depth we must use four different intensity reduction parameters:

$$\left\langle \sqrt{U_{\text{trap}}} \right\rangle = \sqrt{\zeta_{\frac{1}{2}} U_{\text{trap}}^0}$$

$$\langle U_{\text{trap}} \rangle = \zeta_1 U_{\text{trap}}^0$$

$$\left\langle (U_{\text{trap}})^{\frac{3}{2}} \right\rangle = \left( \zeta_{\frac{3}{2}} U_{\text{trap}}^0 \right)^{\frac{3}{2}}$$

$$\left\langle (U_{\text{trap}})^2 \right\rangle = \left( \zeta_2 U_{\text{trap}}^0 \right)^2 \tag{2.66}$$

This however has the down side of introducing four additional parameters. If we assume the radial positions of an atom throughout the interrogation period follow a Gaussian distribution, then we can do a Taylor expansion to first order of all four averages:

$$\left\langle \sqrt{e^{-\frac{r^2}{2\sigma^2}}} \right\rangle \approx \left\langle 1 - \frac{1}{2}\frac{r^2}{\sigma^2} \right\rangle = 1 - \frac{1}{2}\left\langle \frac{r^2}{\sigma^2} \right\rangle,$$

$$\left\langle e^{-\frac{r^2}{2\sigma^2}} \right\rangle \approx \left\langle 1 - \frac{r^2}{\sigma^2} \right\rangle = 1 - \left\langle \frac{r^2}{\sigma^2} \right\rangle,$$

$$\left\langle \left( e^{-\frac{r^2}{2\sigma^2}} \right)^{\frac{3}{2}} \right\rangle \approx \left\langle 1 - \frac{3}{2}\frac{r^2}{\sigma^2} \right\rangle = 1 - \frac{3}{2}\left\langle \frac{r^2}{\sigma^2} \right\rangle,$$

$$\left\langle \left( e^{-\frac{r^2}{2\sigma^2}} \right)^2 \right\rangle \approx \left\langle 1 - 2\frac{r^2}{\sigma^2} \right\rangle = 1 - 2\left\langle \frac{r^2}{\sigma^2} \right\rangle. \tag{2.67}$$

Here $r$ is the radial distance from the center and $\sigma$ is the width of the Gaussian distribution. To this order we can express all the averages as the linear average with a correction applied:

$$\left\langle \sqrt{e^{-\frac{r^2}{2\sigma^2}}} \right\rangle \approx \left\langle e^{-\frac{r^2}{2\sigma^2}} \right\rangle + \frac{1}{2}\left\langle \frac{r^2}{\sigma^2} \right\rangle,$$

$$\left\langle \left( e^{-\frac{r^2}{2\sigma^2}} \right)^{\frac{3}{2}} \right\rangle \approx \left\langle e^{-\frac{r^2}{2\sigma^2}} \right\rangle - \frac{1}{2}\left\langle \frac{r^2}{\sigma^2} \right\rangle,$$

$$\left\langle \left( e^{-\frac{r^2}{2\sigma^2}} \right)^2 \right\rangle \approx \left\langle e^{-\frac{r^2}{2\sigma^2}} \right\rangle - \left\langle \frac{r^2}{\sigma^2} \right\rangle \tag{2.68}$$

Going back to Equation 2.66 we define the correction as he difference between the quadratic average and the linear average:

$$\delta\zeta = \zeta_2 - \zeta_1, \tag{2.69}$$

which then leads to the other averages being defined as:

$$\left\langle \sqrt{U_{\text{trap}}} \right\rangle = \sqrt{\left(\zeta_1 - \frac{1}{2}\delta\zeta\right) U_{\text{trap}}^0}$$

$$\langle U_{\text{trap}} \rangle = \zeta_1 U_{\text{trap}}^0$$

$$\left\langle (U_{\text{trap}})^{\frac{3}{2}} \right\rangle = \left(\left(\zeta_1 + \frac{1}{2}\delta\zeta\right) U_{\text{trap}}^0\right)^{\frac{3}{2}}$$

$$\left\langle (U_{\text{trap}})^2 \right\rangle = \left((\zeta_1 + \delta\zeta) U_{\text{trap}}^0\right)^2 \tag{2.70}$$

When inserting this into Equation 2.62 we arrive at:

$$\begin{aligned}
\Delta\nu_{\text{clock}}^{\text{lattice}} = {}& (a\left(\nu_{\text{lattice}} - \nu_{\text{E1}}\right) - b)\left(n_{\text{avg}} + \tfrac{1}{2}\right)\sqrt{\left(\zeta_1 - \frac{1}{2}\delta\zeta\right)\frac{U_{\text{trap}}^0}{E_{\text{recoil}}}} \\
& - \left(a\left(\nu_{\text{lattice}} - \nu_{\text{E1}}\right) - \frac{3}{4}d(2n_{\text{avg}}^2 + 2n_{\text{avg}} + 1)\right)\zeta_1\frac{U_{\text{trap}}^0}{E_{\text{recoil}}} \\
& + d(2n_{\text{avg}} + 1)\left(\left(\zeta_1 + \frac{1}{2}\delta\zeta\right)\frac{U_{\text{trap}}^0}{E_{\text{recoil}}}\right)^{3/2} \\
& - d\left((\zeta_1 + \delta\zeta)\frac{U_{\text{trap}}^0}{E_{\text{recoil}}}\right)^2 . \tag{2.71}
\end{aligned}$$

where we have also replaces $n$ with the average $n_{\text{avg}}$. We can do this because even though the light shift model is non linear in $n$, our experiments only use $n$ either very close to zero or very close to one, in which case the non linear terms can be approximated as linear.

CHAPTER 3

# The motivation for investigating the hyperpolarizability

As mentioned in the introduction, atomic clocks are not very sensitive to external parameters. But on the levels of accuracy we are measuring even the smallest perturbations will cause a significant shift in the clock transition. Things like constant magnetic fields or finite temperatures cause systematic effects which can be measured and corrected for, but still add an uncertainty based on how well we can measure them. The next section will describe the error budget for the most recent published results of the Yb clock [14].

## 3.1   The previous error budget

Table 3.1 lists the error budget reported in [14] which is the latest official clock measurement using the Yb clock at Riken. This measurement was not an absolute frequency measurement but rather a ratio measurement between strontium-87 and ytterbium-171. The error budget here only represents the uncertainty of the Yb clock and not that of the final measurement.

The values are the fractional uncertainties, meaning they have been divided by the clock frequency. Corrections indicate systematic offsets that have been determined and can be corrected for.

From Table 3.1 we see that the lattice light shift is the largest uncertainty. It is split into three contributions: Running wave contributions arising from power imbalances, lattice laser impurity from the spectral shape of the lattice laser, and the uncertainty of the applied light shift model.

### Running wave contributions

Any power imbalance between the forwards and backwards going beam creating the standing wave lattice will lead to a non-ideal standing wave. This will result in the nodes not having zero intensity, which will change the shape of the potential. Since the light shift model is based on the assumption of a perfect

| Effect | Correction $(10^{-18})$ | Uncertainty $(10^{-18})$ |
|---|---|---|
| Quadratic Zeeman effect | 67.7 | 9.8 |
| BBR shift | 27.5 | 0.7 |
| Probe light shift | -0.8 | 3.2 |
| Collisions | 0.0 | 3.4 |
| AOM chirp and switching | 0.0 | 1.1 |
| 1$^{\text{st}}$ order Doppler effect | 0.0 | 2.0 |
| Servo error | 0.8 | 1.1 |
| Lattice Light shift | 8.5 | 32.8 |
| **Total** | **103.7** | **34.7** |

**Table 3.1:** *The error budget from the last published results of the Yb clock [14]. The numbers are the fractional corrections and uncertainties averaged over the operating conditions encountered during the measurements in [14] .*

standing wave any deviations will lead to an error. The fractional uncertainty contribution from a running wave was determined to $5.9 \cdot 10^{-18}$[14].

## Lattice light impurity

The spectral impurity of the lattice light either due to Amplified Spontaneous Emission (ASE) or spurious frequency components from the laser system was estimated to contribute $1.2 \cdot 10^{-17}$ to the fractional uncertainty.[14]

## The variables and parameters of the light shift model

The lattice laser creates light shifts which we are able to correct for by using the light shift model, but there is an uncertainty on the correction arising from the uncertainty on the input to the model.

The error budget presented here used a light shift model slightly different from the one we derived in Equation 2.71 as it contained only a single parameter for the average trap depth $\zeta$ instead of both $\zeta_1$ and $\delta\zeta$:

$$
\begin{aligned}
\Delta\nu_{\text{clock}}^{\text{lattice}} = {} & (a\,(\nu_{\text{lattice}} - \nu_{\text{E1}}) - b)\,(n_{\text{avg}} + {}^{1}\!/\!{}_{2})\sqrt{\zeta\frac{U_{\text{trap}}^0}{E_{\text{recoil}}}} \\
& - \left(a\,(\nu_{\text{lattice}} - \nu_{\text{E1}}) - \frac{3}{4}d(2n_{\text{avg}}^2 + 2n_{\text{avg}} + 1)\right)\zeta\frac{U_{\text{trap}}^0}{E_{\text{recoil}}} \\
& + d(2n_{\text{avg}} + 1)\left(\zeta\frac{U_{\text{trap}}^0}{E_{\text{recoil}}}\right)^{3/2} \\
& - d\left(\zeta\frac{U_{\text{trap}}^0}{E_{\text{recoil}}}\right)^2 .
\end{aligned}
\tag{3.1}
$$

where variables $a$, $b$ $d$, and $\omega_{\mathrm{E1}}$ are identical to those derived earlier:

$$a = \frac{1}{h} \frac{\partial \Delta \alpha^{E1}}{\partial \nu} \frac{E_{\mathrm{recoil}}}{\alpha^{E1}}$$

$$b = \frac{1}{h} \left( \Delta \alpha^{M1} + \Delta \alpha^{E2} \right) \frac{E_{\mathrm{recoil}}}{\alpha^{E1}}$$

$$d = \frac{1}{h} \Delta \beta \left( \frac{E_{\mathrm{recoil}}}{\alpha^{E1}} \right)^2 . \qquad \text{(Reprint of Equation 2.63)}$$

$a$, $b$ and $\omega_{\mathrm{E1}}$ were experimentally determined in [14], whereas the parameter $d$ was taken from a different Yb clock located at NIST [2] which was running with different operational parameters. $d$ was therefore modified to fit the parameters of the RIKEN clock. This was done because the Riken setup was not built to access trap depths ($U_{\mathrm{trap}}^0$) large enough to determine $d$ accurately.

The variables and operational conditions for the error budget from Table 3.1 were:

$$a = 0.021(6) \ \mathrm{mHz/MHz} \qquad b = -0.68(71) \ \mathrm{mHz}$$

$$d = -1.9(8) \ \mathrm{\mu Hz} \qquad U_{\mathrm{trap}}^0 = 100(2) \ E_{\mathrm{recoil}}$$

$$\zeta = 0.72(5) \qquad n_{\mathrm{avg}} = 0.08(8)$$

$$\nu_{\mathrm{lattice}} = 394\ 798\ 278(0.1) \ \mathrm{MHz} \qquad \nu_{\mathrm{E1}} = 394\ 798\ 265(9) \ \mathrm{MHz} \qquad (3.2)$$

To determine how much each parameter influences the final uncertainty, we assume normally distributed and uncorrelated uncertainties and do error prop-

agation:

$$
\begin{aligned}
\sigma^2 = & \left[ \left( (\nu_{\text{lattice}} - \nu_{\text{E1}})(n_{\text{avg}} + 1/2)\sqrt{\zeta \frac{U^0_{\text{trap}}}{E_{\text{recoil}}}} - (\nu_{\text{lattice}} - \nu_{\text{E1}})\zeta \frac{U^0_{\text{trap}}}{E_{\text{recoil}}} \right) \sigma_a \right]^2 + \\
& + \left[ \left( -(n_{\text{avg}} + 1/2)\sqrt{\zeta \frac{U^0_{\text{trap}}}{E_{\text{recoil}}}} \right) \sigma_b \right]^2 + \\
& + \left[ \left( \tfrac{3}{4}(2n^2_{\text{avg}} + 2n_{\text{avg}} + 1)\zeta \frac{U^0_{\text{trap}}}{E_{\text{recoil}}} + (2n_{\text{avg}} + 1)\left( \zeta \frac{U^0_{\text{trap}}}{E_{\text{recoil}}} \right)^{3/2} - \left( \zeta \frac{U^0_{\text{trap}}}{E_{\text{recoil}}} \right)^2 \right) \sigma_d \right]^2 + \\
& + \left[ \left( a(n_{\text{avg}} + 1/2)\sqrt{\zeta \frac{U^0_{\text{trap}}}{E_{\text{recoil}}}} - a\zeta \frac{U^0_{\text{trap}}}{E_{\text{recoil}}} \right) \sigma_{\nu_{\text{lattice}}} \right]^2 + \\
& + \left[ \left( -a(n_{\text{avg}} + 1/2)\sqrt{\zeta \frac{U^0_{\text{trap}}}{E_{\text{recoil}}}} + a\zeta \frac{U^0_{\text{trap}}}{E_{\text{recoil}}} \right) \sigma_{\nu_{\text{E1}}} \right]^2 + \\
& + \left[ \left( (a(\nu_{\text{lattice}} - \nu_{\text{E1}}) - b)\sqrt{\zeta \frac{U^0_{\text{trap}}}{E_{\text{recoil}}}} + \tfrac{3}{4}d(4n_{\text{avg}} + 2)\zeta \frac{U^0_{\text{trap}}}{E_{\text{recoil}}} + 2d\left( \zeta \frac{U^0_{\text{trap}}}{E_{\text{recoil}}} \right)^{3/2} \right) \sigma_{n_{\text{avg}}} \right]^2 + \\
& + \left[ \left\{ (a(\nu_{\text{lattice}} - \nu_{\text{E1}}) - b)(n_{\text{avg}} + 1/2)\sqrt{\frac{U^0_{\text{trap}}}{E_{\text{recoil}}}} \tfrac{1}{2}\zeta^{-\frac{1}{2}} \right. \right. \\
& \left. - (a(\nu_{\text{lattice}} - \nu_{\text{E1}}) - \tfrac{3}{4}d(2n^2_{\text{avg}} + 2n_{\text{avg}} + 1)) \frac{U^0_{\text{trap}}}{E_{\text{recoil}}} \right. \\
& \left. + d(2n_{\text{avg}} + 1)\left( \frac{U^0_{\text{trap}}}{E_{\text{recoil}}} \right)^{3/2}\tfrac{3}{2}\sqrt{\zeta} - d\left( \frac{U^0_{\text{trap}}}{E_{\text{recoil}}} \right)^2 2\zeta \right\} \sigma_\zeta \right]^2 + \\
& + \left[ \left\{ (a(\nu_{\text{lattice}} - \nu_{\text{E1}}) - b)(n_{\text{avg}} + 1/2)\sqrt{\frac{\zeta}{E_{\text{recoil}}}} \tfrac{1}{2}\left( U^0_{\text{trap}} \right)^{-\frac{1}{2}} \right. \right. \\
& \left. - (a(\nu_{\text{lattice}} - \nu_{\text{E1}}) - \tfrac{3}{4}d(2n^2_{\text{avg}} + 2n_{\text{avg}} + 1)) \frac{\zeta}{E_{\text{recoil}}} \right. \\
& \left. + d(2n_{\text{avg}} + 1)\left( \frac{\zeta}{E_{\text{recoil}}} \right)^{3/2}\tfrac{3}{2}\sqrt{U^0_{\text{trap}}} - d\left( \frac{\zeta}{E_{\text{recoil}}} \right)^2 2U^0_{\text{trap}} \right\} \sigma_{\left( U^0_{\text{trap}} \right)} \right]^2
\end{aligned}
$$

$$(3.3)$$

By plugging in the values from Equation 3.2 we get the uncertainty contributions listed in Table 3.2 that almost sum to the value listed in Table 3.1.

The dominating uncertainty contribution comes from the E1 magic frequency $\nu_{\text{E1}}$ which is largely because the uncertainty was determined to 9 MHz.

From previous works [15] it can be seen that a large part of this uncertainty was due to the borrowed $d$ from NIST. It therefore seems paramount to investigate and characterize $d$ for the Riken Yb clock, with the expectation that it will bring down, not only the uncertainty on $\nu_{\text{E1}}$, but also on the other variables $a$, $b$ and $d$.

| Coefficient | Uncertainty contribution ($\frac{1}{\nu_{\text{clock}}} \times 10^{-18}$) |
|---|---|
| a | 10.1 |
| b | 6.7 |
| d | 6.8 |
| $\zeta$ | 2.6 |
| $n_{\text{avg}}$ | 0.85 |
| $\nu_{\text{E1}}$ | 26.0 |
| $\nu_{\text{lattice}}$ | 3.5 |
| $U_{\text{trap}}^0$ | 0.6 |
| Running wave | 5.9 |
| Lattice light impurity | 12.0 |
| **Total** | 32.7 |

**Table 3.2:** *Contribution to the fractional uncertainty from the lattice light shift model, given the nominal experimental parameters used in [14].*
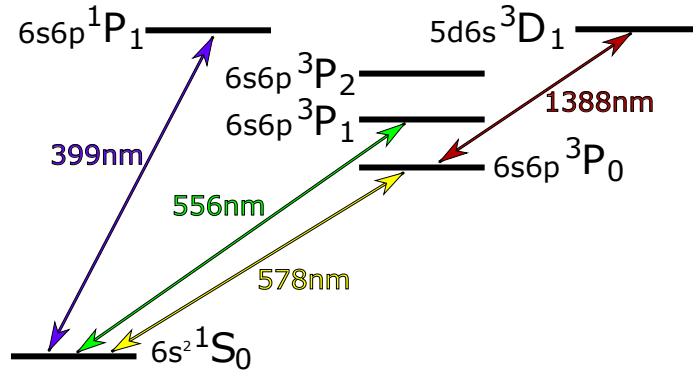
# The experimental setup



**Figure 4.1:** *The level diagram for ytterbium-171. Only the levels relevant for clock operation are displayed.*

The Yb optical lattice clock at Riken operates with $^{171}$Yb, which has a range of beneficial properties such as a nuclear spin of $I = \frac{1}{2}$ which not only simplifies the clock operation as we will see in Section 4.3, but also removes any kind of tensor[1] light shifts[6].

As stated earlier Yb is a two electron atom and has a level structure (Figure 4.1) well suited for clock spectroscopy. It has a clock transition at 578 nm with a natural linewidth of $\sim 50$ mHz and a magic wavelength at 759 nm, together with a set of transitions suitable for cooling the atoms enough to trap them in the optical lattice lattice.

In general terms the Yb clock works by loading atoms into the lattice and preparing them in a known initial state. A probe laser is then used to excite them and the excitation fraction is detected. Because the detection process

---

[1]Only scalar light shifts were considered in Section 2.3 because $^{171}$Yb has no tensor light shifts and no vector light shifts when the polarization of the clock laser is identical to the lattice. This will be explained in the following sections.

heats the atoms out of the lattice we must repeatedly reload the lattice, excite, and detect again. Each reload and measurement is called a shot and the clock transition frequency is measured by averaging over many repeated shots.

The experimental setup is mostly identical to the one described in both [15] and [14]. A few major changes have been made, mostly to the lattice, to allow investigation of larger trap depths primarily to determine the hyperpolarizability.

Each shot follows a special sequence of actions which will be explained step by step in the following sections along with the lasers and atomic levels involved. The full experimental setup and timings diagram can be seen on Figure 4.19 and Figure 4.17, but will make more sense to the reader after the next sections.

Many techniques such as magneto-optical traps[19] and fiber noise cancellation[12] will be mentioned but the details will be assumed known to the reader. As the systems for generating the lasers were already built when I joined the group the technical details will also mentioned but not elaborated upon.

## 4.1   The Lattice

The lattice is one of the most fundamental parts of the lattice clock. It is what allows us to do Doppler free and recoil free spectroscopy, motional sideband cooling and long interaction times, but also what creates the light shifts that dominate the clock uncertainty.

Figure 4.2 shows the experimental setup with the part relating to the lattice highlighted. The lattice laser is on during the entire sequence but its intensity is varied systematically.

The lattice laser is generated by a Ti:Sapphire (TiSa) laser system, which is able to output high power (roughly 4 W) at the magic wavelength of $^{171}$Yb $\sim 759$ nm.

After the TiSa the lattice laser is filtered by a Volume Bragg Grating with a FWHM of roughly 40 GHz. This is not depicted Figure 4.2, but details can be found in [15]. The lattice is then sent through an AOM for power and frequency control before it is brought to the clock setup by a 1 m end-capped (EC) fiber.

The high power of the lattice laser could easily burn the surface of an ordinary fiber, but the EC fiber has a small piece of glass attached to each end. This allows the beam to have a larger diameter at the air/glass interface, thus reducing the power density and minimizing the chance of burning the surface. For our experiments we need at most 1.3 W of transmitted power but we have tested the fiber up to 2.4 W transmitted power without visible damage when inspected under a microscope.

After leaving the fiber, the lattice laser is focused by a microscope objective lens to a width of about 43 μm at the beam waist. The first mirror after the lens is marked "Bad" because it deliberately leaks some of the light through. The leaked light is monitord by a photo diode (PD 1) and used to control the power of the lattice through feedback to the AOM.

After the "Bad" mirror the lattice is reflected off a dichroic mirror (DM) and finally off a polarizing beam splitter (Rotated PBS). All the elements inside the
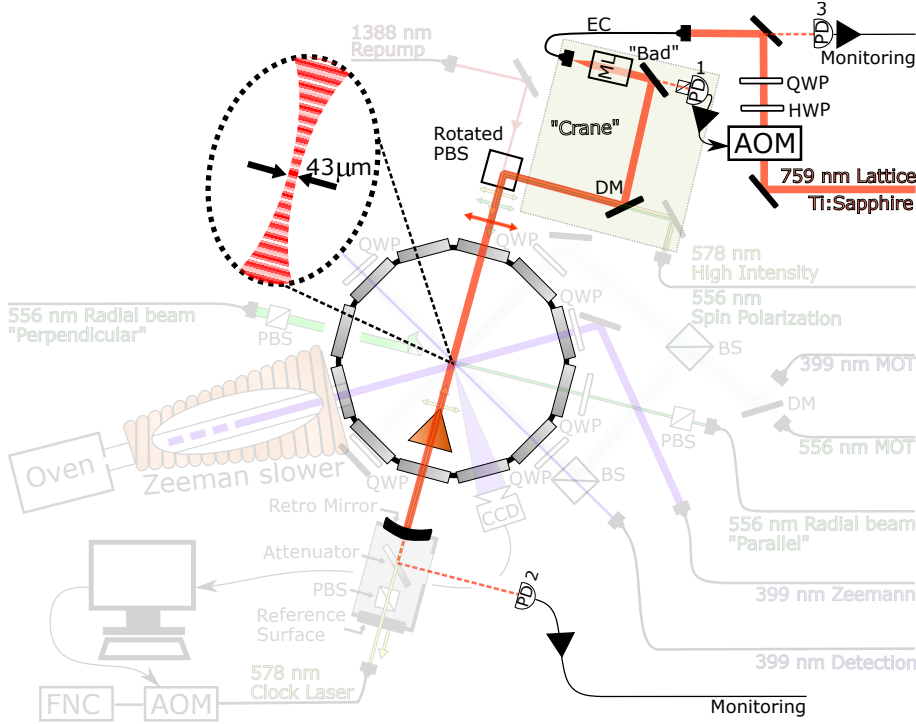
**Figure 4.2:** *The clock setup with the parts not relating to the lattice lattice laser faded. The round main structure in the center is a vacuum chamber. The lattice laser comes from a TiSa system and passes through a quarter- and half-wave plate (QWP and HWP) before entering an endcapped (EC) fiber. It is then focused by a microscope objective lens (ML) and reflected off a "bad" mirror, then a dichroic mirror (DM) and a polarizing beam splitter (Rotated PBS) before entering the vaccum chamber. All the elements inside the shaded region marked "Crane" are mounted 20 cm above the rest as shown on Figure 4.3. A meniscus shaped mirror at the bottom of the setup reflects the lattice laser back on itself, creating a standing wave. Various photodiodes (PD) are used to monitor the lattice laser pointing, power and polarization. Power control is done with the acousto-optic modulator(AOM).*

shaded area labeled "Crane" in Figure 4.2 are mounted in a crane structure, in a different plane than the rest. The lattice therefore enters the rotated PBS from above as illustrated on Figure 4.3.

After passing through the vaccum chamber the lattice laser is retro reflected upon itself by a meniscus shaped mirror below the chamber as seen on Figure 4.2, thus creating a standing wave which has 4 times the single beam intensity at the anti nodes.

A third photo diode (PD 3) is installed before the EC fiber but looks at the light reflected off the meniscus mirror and returning back through the fiber. With this signal we can optimize the overlap of retro reflected beam and ensuring a good standing wave. The waist position of the lattice is determined by the radius of curvature of the retro reflecting surface and is approximately in the center of the vaccum chamber. The collimation of the lattice laser is changed by translating the fiber mount relative to the microscope objective
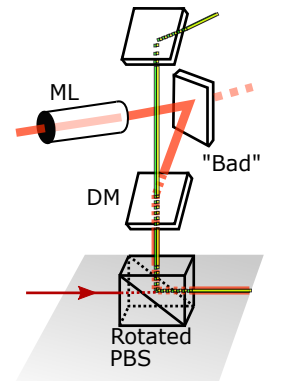


**Figure 4.3:** *Sideways illustration of the elements included in the shaded area in Figure 4.2 marked "Crane".*

lens until the curvature of the beam matches the curvature of the meniscus mirror.

In the previous setup the lattice was created by two counter propagating lattice beams brought in from the top and the bottom separately and used to create a 'moving' standing wave by detuning the frequency of one beam from the other. This could transport the atoms several mm into the cryogenic chamber[2] where they were then excited by the clock laser. This was done to reduce the effect of environmental black body radiation[26] by cooling the entire cryogenic chamber to 96 K and only allowing tiny access holes of 500 μm and 1000 μm in diameter. Since our goal is to investigate the hyperpolarizability we do not need to minimize the black body radiation.

Even though the EC fiber is polarization maintaining we still observe a slow drift of the transmitted polarization over the course of hours. The polarizing beam splitter (PBS) in front of the chamber ensures a constant polarization in the chamber, but it still leads to drops in lattice power. The "Bad" mirror leaks mostly p-polarized light, which is the "wrong" polarization of the EC fiber and the polarization that gets filtered out by the rotated PBS. Because PD 1 is places behind the "Bad" mirror it will overestimate the lattice power when the polarization drifts, resulting in the feedback system not accurately controlling the lattice power in the vacuum chamber. To alleviate this a small PBS is glued directly in front of PD 1 as seen on Figure 4.2, unfortunately the small PBS is angled slightly different than the rotated PBS and therefore does not completely fix the problem.

Instead we place a quarter wave plate (QWP) and a half wave plate (HWP) in front of the EC fiber and by measuring the light leaking from the curved mirror with PD 2, we can adjust the wave plates to compensate for any drift. We cannot power stabilize directly to PD 2 as the polarization drift would lead to the feedback system simply increasing the lattice power. The lattice power in the chamber would be kept constant but the transmitted power through the fiber might get dangerously high.

We suspect that the polarization drift is due to stress induced birefringence in the collimation lens (not drawn) before the EC fiber as a result of the lattice laser heating the mount holding both the lens and the fiber, so increasing the lattice power to compensate for polarization changes would then create a run away effect.

Because the new lattice setup has no way of making a 'moving' lattice we will need to convert the setup back to the previous configuration when we are done determining the coefficients of the light shift model. We therefore did not want to change any optical elements that the previous lattice setup used and instead had to retrofit the old setup by installing new elements 'above' the old ones, on a crane structure. A picture of the crane can be seen on Figure 4.4 where the right image is the crane structure before it was put into the clock setup and the left picture is the clock setup with the crane structure in place.

---

[2]The cryogenic chamber is illustrated on Figure 4.2 as a copper triangle inside the main chamber.

The rotated PBS was installed on a flip mount to allow fast conversion back to the old lattice setup. The rotation mount visible right after the Rotated PBS is empty.

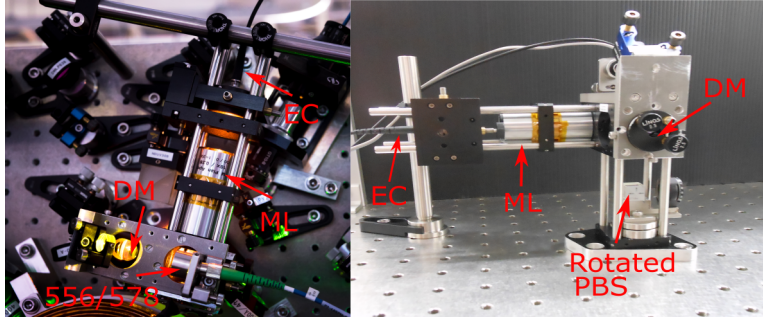

**Figure 4.4:** *Two pictures of the crane structure illustrated in Figure 4.3. The right picture is the structure before it was placed in the clock setup, the left picture is after. The "Bad" mirror is not visible on any of these two pictures.*
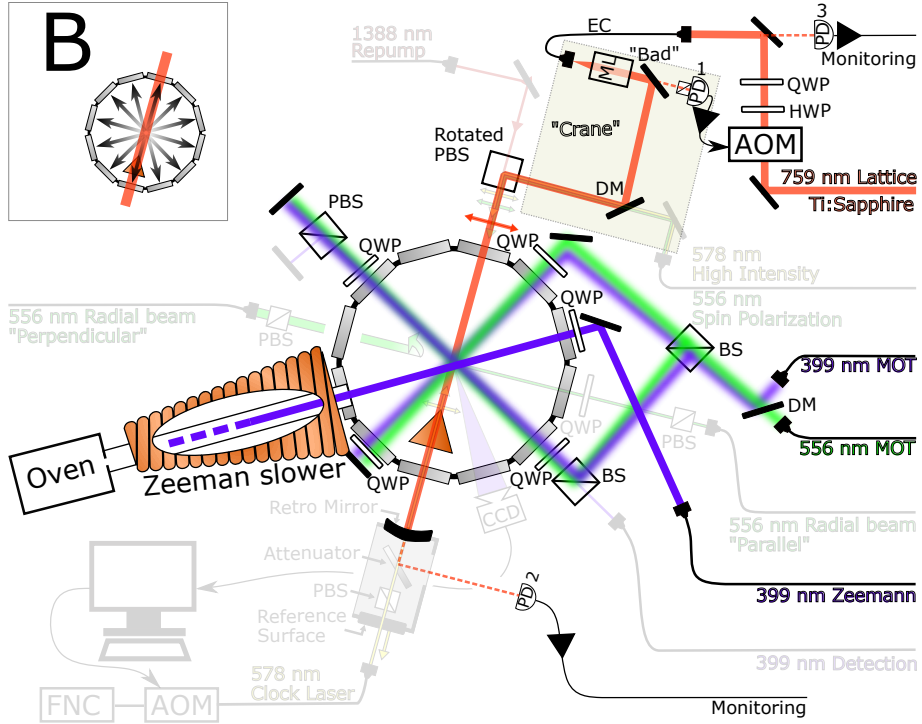
**Figure 4.5:** *The clock setup with the parts not relating to the loading sequence faded. The atoms from the oven are cooled by a Zeeman slower and then further cooled by a two stage MOT, working first on the 399 nm transition and then on the 556 nm transition. The vacuum chamber has 11 windows for radial optical access, while the atomic beam enters through the 12. radial port. There are MOT beams in all three directions but only two of them are shown here as the last one is perpendicular to the two drawn here. After the second stage MOT the atoms are loaded into the lattice.*
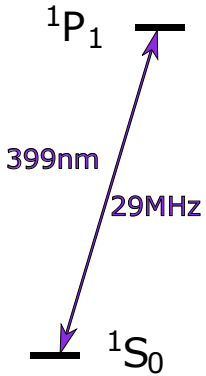
## 4.2 Loading sequence

Inside the oven seen on Figure 4.5 the atoms are heated to $\sim 450$ °C and leave as a collimated beam, but before the atoms can enter the lattice, they must be cooled to temperatures where they are actually confined by the lattice potential.

This is done in a series of steps, where the first uses the $^1S_0 \leftrightarrow {}^1P_1$, fully allowed dipole transition. The transition is at 399 nm and has a line width of 28 MHz as illustrated on Figure 4.6.

The hot atomic beam first enters an increasing field Zeeman slower where the atoms are slowed down by a counter propagating 399 nm beam. Once the atoms leave the Zeeman slower and enter the main chamber they are caught in an magneto-optical trap (MOT). This MOT is called the first stage MOT and also works on the 399 nm transition. The MOT is detuned 30 MHz from the resonance while the Zeeman slower beam is detuned 750 MHz to be able to target the fast atoms leaving the oven with $\sim 300$ m ⊥ s.

The 399 nm light is generated by using a BIBO crystal to frequency double



**Figure 4.6:** *Level diagram.*

1 W at 798 nm to 200 mW at 399 nm. In our experiment, we generate the Zeeman slower and first stage MOT light in two independent frequency doubling setups. Both 798 nm sources for the two 399 nm setups, are frequency stabilized by a High Finesse wavemeter using a digital PID lock.

The atoms need to be cooled to a temperature low enough that they can be trapped in the lattice. For most of the experiments done here we keep a constant lattice intensity during loading corresponding to a trap frequency of $\omega_T = 2\pi \cdot 93$ kHz from which we can calculate a trap depth:

$$\omega_T = 2\sqrt{\frac{E_{\text{recoil}}}{\hbar}\frac{V_{\text{trap}}}{\hbar}} \qquad \text{(reprint of Equation 2.23)}$$

$$U_{\text{trap}} = \frac{\omega_T^2\hbar^2}{4E_{\text{recoil}}}$$

$$U_{\text{trap}} = \frac{(2\pi \cdot 93 \text{ kHz})^2\hbar}{4 \cdot 2\pi \cdot 2.02 \text{ kHz}}$$

$$\frac{U_{\text{trap}}}{k_{\text{B}}} = 51 \text{ μK} \tag{4.1}$$

where we have converted the trap depth to temperature in the last line by dividing with Boltzmann's constant $k_{\text{B}}$.

The lowest temperature a MOT can theoretically achieve depends on the line width and is called the Doppler limit[8]:

$$T = \frac{\hbar\gamma}{2k_B}. \tag{4.2}$$

where $\gamma$ is the line width in angular frequency. For the 399 nm MOT the Doppler limit is 690 μK. Since this is much higher than the depth of the lattice, we apply a second stage MOT this time working on the $^1S_0 \leftrightarrow {}^3P_1$ transition. The transition has a wavelength of 556 nm and a line width of only 180 kHz (see Figure 4.7), leading to a theoretical Doppler limit of 4.2 μK. Because of the narrow line width the 556 nm laser is artificially broadened by a frequency modulation of 2.5 MHz to ensure that the second stage MOT catches as many atoms as possible when transferring from the first to second stage MOT.

After the atoms have cooled down in the broadened second stage MOT the frequency modulation is removed and the atoms are transferred from the MOT into the lattice. This is done by ramping down the power of the 556 nm beams while bringing them closer to resonance.This compresses the atomic cloud and increases the loading efficiency into the lattice.

Previous experiments show that the atoms at this point have a temperature around $\sim 15$ μK[15] however that was measured without the lattice beam present.

The number of atoms in the lattice can be adjusted by changing the duration of the initial Zeeman slower beam, since a shorter pulse will slow down fewer atoms.

The 556 nm light is generated by a fiber coupled frequency doubling crystal (WG-PPLN) converting 100 mW of 1112 nm, generated by an "orange one" system from MenloSystems, to 30 mW at 556 nm. The 1112 nm light that leaks through the frequency doubling crystal is used to lock the laser to a cavity. A small part of the 556 nm light is used for calibrating the wavemeter controlling the 399 nm lasers.
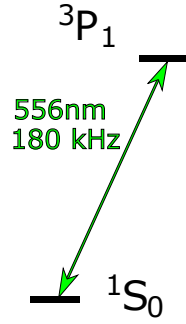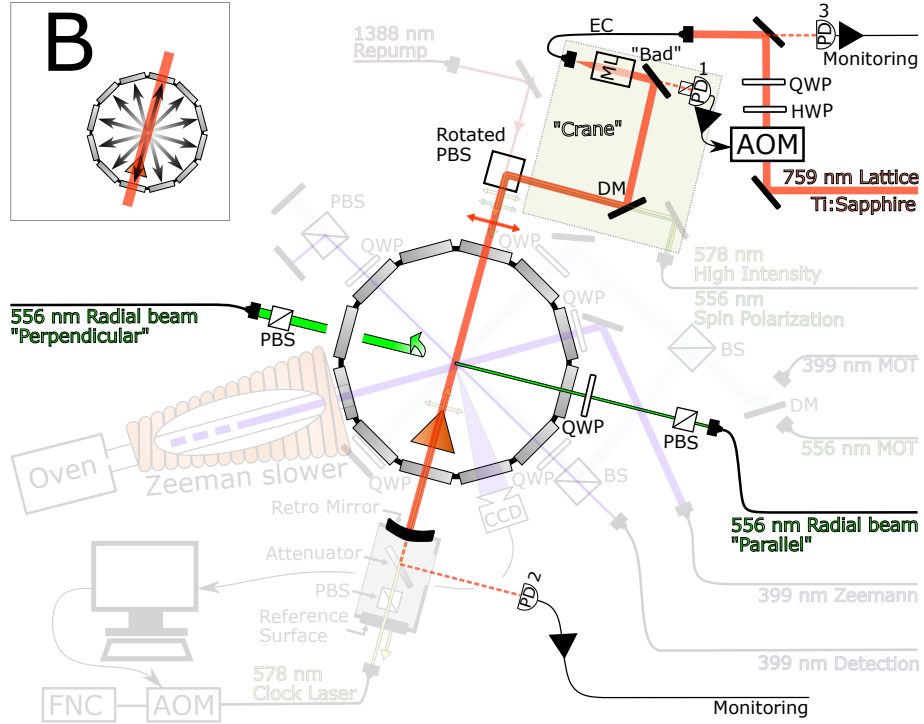


**Figure 4.7:** *Level diagram.*

**Figure 4.8:** *The clock setup with the parts not relating to the settling faded. The settling pulses cool the atoms in the radial directions and increase the number of atoms ending in the lattice.*

## 4.3   Settling the atoms

As this is only a 1D lattice, the confinement in the two other dimensions (referred to as "radial"), is purely due to the Gaussian intensity profile of the lattice beam as explained in Section 2.2.2.

To minimize the radial energy of the atoms we apply a 1 ms pulse of 556 nm light in the two radial directions, one perpendicular and one parallel to the lattice polarization. This is much shorter than the radial oscillation time and is carefully detuned to only target atoms moving towards the beams. This "settles" the radially hot atoms and increases the overall final atom number in the lattice.

The light for the settling pulses comes from the same laser that generates the second stage MOT, but is independently controlled by AOMs and sent onto the atoms through a different set of fiber.
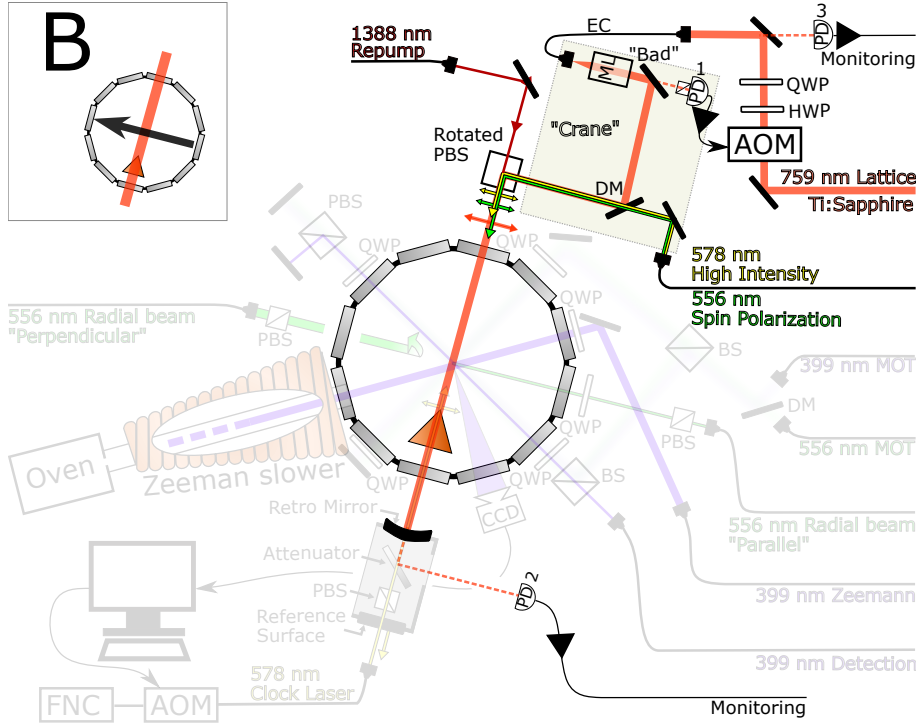
**Figure 4.9:** *The clock setup with elements not used for state preparation faded. The atoms are simultaneously cooled in the axial direction to $n = 0$ using motional sideband cooling and pumped into one of the $m_F \pm \frac{1}{2}$ Zeeman substates of the ground state.*

## 4.4 Clock state preparation

After the loading and settling phase, we move on to the state preparation in which the atoms are prepared for clock interrogation. This consists of two different techniques: Axial motional sideband cooling, and spin polarization. The relevant lasers and elements have been highlighted on Figure 4.9.

The sideband cooling is used to cool the atoms in the axial direction. From the theory in Section 2.2.1 and from Figure 2.7 we know that the axial motional sidebands are clearly resolved. By exciting the atoms on the red sideband, we can decrease the vibrational level of the atoms by one. This is done on the $^1S_0 \leftrightarrow {}^3P_0$ transition at 578 nm which is also the clock transition (see Figure 4.10).

Since the $^3P_0$ state has a lifetime of 20 s[18] we need to "repump" the atoms out of the excited clock state and back into the ground state. This is done with the a 1388 nm laser through the $^3D_1$ state (Figure 4.11). We excite the atoms into $^3D_1$ from which they can spontaneously decay into the $^3P$ manifold with the probabilities 3%, 42%, and 55%[15] for decay into $^3P_2$, $^3P_1$, and $^3P_0$ respectively.

From $^3P_1$ they can decay into the ground state and from $^3P_0$ we can excite them to $^3D_1$ again, but if they end in $^3P_2$ they are stuck since it has a lifetime
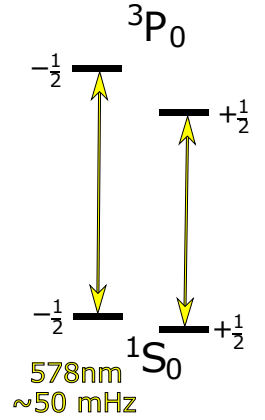


**Figure 4.10:** *Level diagram with Zeeman substates ($m_F$).*
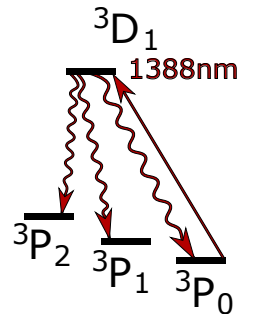


**Figure 4.11:** *Level diagram.*

of 15 s[17].

Since the spontaneous emission in an optical lattice predominantly conserves[3] $n$, the atoms tend to end up in the ground state with their vibrational level reduced relative to their initial state as illustrated on Figure 4.12.

To cool all the atoms to $n = 0$ we must continuously pump both on the red sideband ($^1S_0 \leftrightarrow {}^3P_0$) and on the $^3P_0 \leftrightarrow {}^3D_1$.
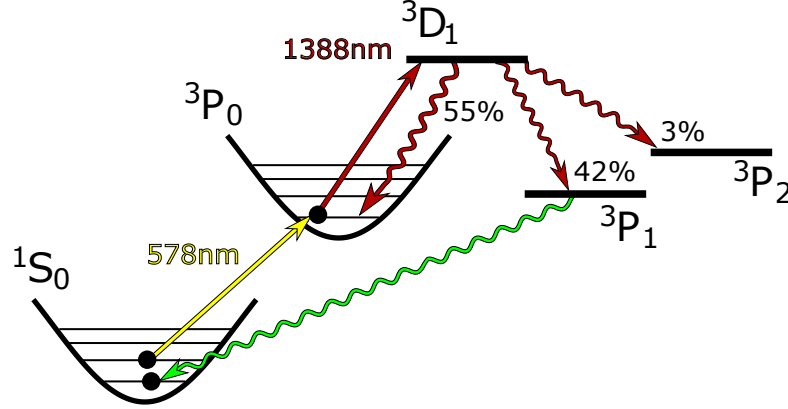


**Figure 4.12:** *The process of vibrational cooling considering an atom in $n > 0$ starting in the ground state $^1S_0$. From here it is excited on the red sideband of the 578 nm transition to $n-1$ in $^3P_0$. The atom is then pumped back to the ground state through the $^3D_1$ state with the 1388 nm laser. From $^3D_1$ it will decay to the $^3P$ manifold with the chance of ending in each state indicated in percent. From $^3P_1$ it can decay back to the ground state.*

The repump laser at 1388 nm is created by an ECDL and locked to the same cavity as the 1112 nm laser used to generate the 556 nm light. The 578 nm laser used to excite the red sideband is branched off from the clock laser used for the main clock interrogation, which will be explained shortly.

The second step of state preparation is spin polarization. Even when loading very few atoms, we will still have a few lattice sites occupied by two atoms. This leads to collisions which are enhanced by the strong confinement and which give rise to a shift of the clock transition[10]. Since the atoms are fermions Pauli's exclusion principle will suppress a large part of these collisions if we prepare them in an identical state. Furthermore, since the clock laser only targets one of the Zeeman substates we increase the signal to noise ratio by only having atoms in the state we wish to excite.

At this point the MOT B-fields have been turned off and a constant bias B-field of $\sim 80$ µT is applied.

Because $^{171}$Yb has a nuclear spin of $\frac{1}{2}$ there is only two configurations of the nuclear spin when the atom is in the ground state $^1S_0$; Either parallel or anti parallel with the B-field. These are commonly called the Zeeman substates, or $m_F$ states.

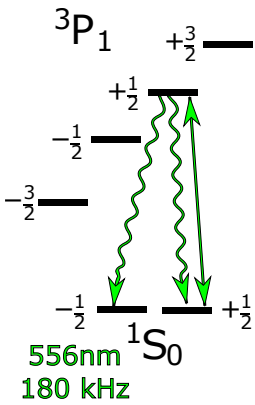The $^3P_1$ state has an electronic angular momentum of one and a combined spin of one.



**Figure 4.13:** *Level diagram with Zeeman substates.*

---

[3]This is due to the matrix element regarding vibrational level changes being suppressed by $\eta$ as explained in Section 2.2.1.

Spin polarization is achieved by pumping on either the $^1S_0 \leftrightarrow {}^3P_1 m_{F_{1/2}}$ or $^1S_0 \leftrightarrow {}^3P_1 m_{F_{-1/2}}$ trasition with $\pi$ polarized light. The $^3P_1$ substates are separated by $\sim 1.2$ MHz, and because the atomic line width is only 180 kHz, the 556 nm laser can selectively target only one of the transitions.

As seen on Figure 4.13 the $^3P_1$ state can decay to either of the two Zeeman substates with either a $\sigma$ or a $\pi$ polarized decay. This pumps all the atoms out of one of the ground state substates, but is a process which requires multiple cycles as the chance of spontaneously decaying with a $\sigma$ polarized photon versus a $\pi$ polarized is 1:2.

If $^{171}$Yb had a larger nuclear spin we would have a larger range of $m_F$ states, meaning it would be more complicated to prepare all atoms in the same state.

The 556 nm light for the spin polarization is generated in the same way as the light used for the settling pulses described previously, but coupling into a different fiber. The spin polarization light is overlapped with the high power clock beam used for sideband cooling and enter the clock setup through the same fiber (as seen on Figure 4.9). The PBS in front of the chamber prevents us from using circular polarized light to do the spin polarization, even though it would be more effective as it would require fewer cycles.

Before the state preparation begins, the lattice depth is reduced adiabatically to a level in the middle of the range we want to investigate, typically 155 $E_{\mathrm{recoil}}$ or 105 $E_{\mathrm{recoil}}$. It is now more useful to define the trap depth in terms of recoil energy than in temperature because it simplifies the light shift model equation (Equation 2.71). The loading point of 51 μK corresponds to a trap depth of 520 $E_{\mathrm{recoil}}$, and after loading the lattice depth is reduced to 155 $E_{\mathrm{recoil}}$ to reduce the vibrational level spacing which makes it easier for the sideband cooling laser to target all atoms with $n > 0$.

Since both the sideband cooling and spin polarization relies on spontaneous emission, one has a tendency of reducing the effect of the other. Sideband cooling mixes up the population in the Zeeman substates, and spin polarization heats up the atoms. We therefore apply the sideband cooling and spin polarization in alternating pulses, with the finishing pulse being either one or the other depending on which effect we wish to increase.

The clock can also be run in "inverted" mode where the atoms are prepared in the excited state instead of the ground state allowing us to prepare the atoms in a pure $n = 1$ state. This is done by following the sideband cooling and spin polarization by a short pulse of the high power clock laser focused on the blue sideband. This increases $n$ by one for some fraction of the atoms and since the excited state has a long life time, we can clear out the ground state with a high power 556 nm pulse, leaving us with only the $n = 1$ atoms in the lattice. We can also prepare atoms in $n = 0$ by targeting the carrier instead of the blue sideband with the short pulse and then similarly clearing out the ground state. Because there is no reliable way of clearing out the excited state it is not possible to create a pure $n = 2, 3, 4 \ldots$ state.
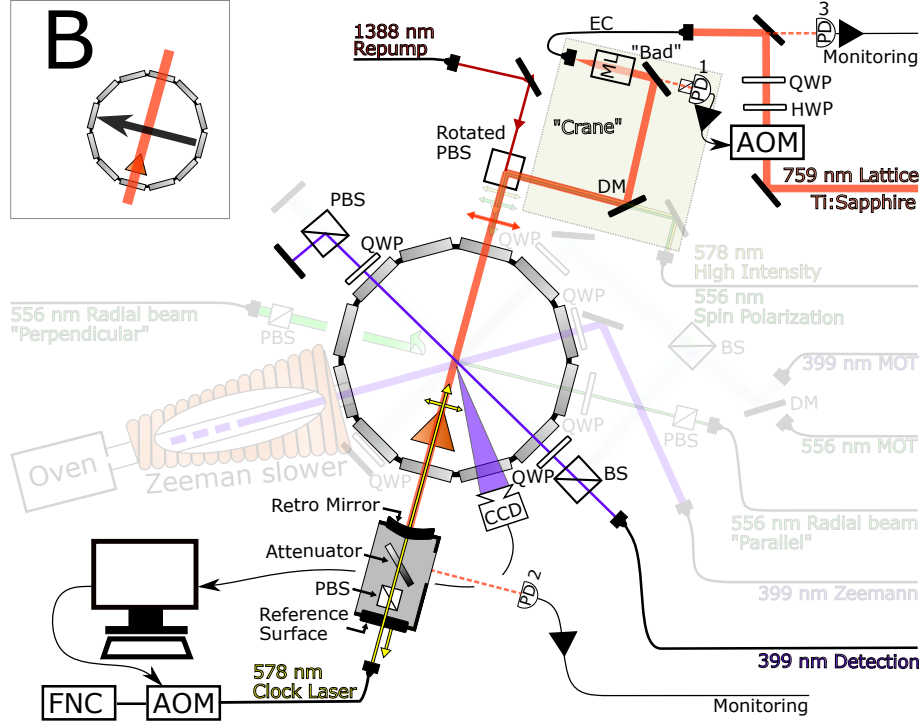
**Figure 4.14:** *The clock setup with the parts not relating to the clock interrogation faded. The atoms are interrogated by the clock beam coming from below the vacuum chamber and passing through the curved mirror used by the lattice. The detection is done by cycling the atoms in the ground state on the $^1S_0 \leftrightarrow ^1P_1$ transition with a 100 $\mu$s pulse of 399 nm light, which removes them from the lattice, and recording the florescence on a CCD camera. The atoms left in the excited state are then repumped to the now empty ground state with the 1388 nm laser. The FNC and AOM of the clock laser feedback are implemented in the opposite order.*

## 4.5   Clock Spectroscopy and detection

With the atoms now both cold and spin polarized, we move on to clock spectroscopy. The clock laser is generated by frequency doubling 1157 nm light in a WG-PPLN. The 578 nm light is pre-stabilized by locking it to a 75 mm cavity and then phase locking to an optical comb, which is generated by a laser that is locked to a 400 mm long cavity.

It is in this setup that the clock laser is divided into two different branches; a high power branch, used for the sideband cooling described previously, and a low power branch used for clock interrogation.

The clock laser is generated far from the chamber and the atoms, and is led there through optical fibers. To prevent phase noise in the fibers originating from fluctuating temperature or stress which changes the optical path length in the fiber, a standard fiber noise cancellation system[12] is implemented in both the high power and low power branch.

The clock laser enters the chamber from the bottom, after passing through first a reference surface for the FNC system, a PBS for polarization cleanup, an

attenuator, and finally the meniscus mirror used for the lattice. The attenuator has a transmission of only 10 % which allows a large FNC signal while still only interrogating the atoms with low power.

Since the placement of the nodes and antinodes of the lattice depends on the position of the meniscus mirror, the FNC reference surface is mounted on the same structure to minimize any phase drift between lattice and the clock laser.

To prevent any unnecessary light shifts, all other lasers except the lattice are blocked by mechanical shutters while the clock laser is exciting the atoms.

Before starting the interrogation the lattice ramps to the desired trap depth. If this is below 200 $E_{\mathrm{recoil}}$, we first dip to 65 $E_{\mathrm{recoil}}$ before ramping up. This is done to remove any atoms with enough radial energy to get close to the edge of the trap. When interrogating at trap depths above 200 $E_{\mathrm{recoil}}$ it is sufficient to ramp up the trap depth.

The 80 μT B-field creates a splitting of the clock state Zeeman substates of 2.1 MHz/T[10] which equals $\sim$ 170 Hz. Because the line width of the clock laser is very narrow we can selectively target either of the two transitions indicated in Figure 4.10 depending on which state we have prepared the atoms in.

After interrogation, the result is detected. This is done by saturating the atoms with a 100 μs pulse of 399 nm light, branched off from the first stage MOT setup, and independently controlled by an AOM. The fluorescence is recorded on a CCD camera equipped with a 400 nm bandpass filter. The 399 nm laser is only resonant with atoms in the ground state and the 100 μs pulse effectively heats all the ground state atoms out of the lattice, so a series of 3 pictures are taken to determine the excited fraction: First the atoms in the ground state are detected and removed. Then the 1388 nm laser repumps the atoms in the excited state into the, now empty, ground state where they are detected as before. With no more atoms left, a third picture is taken while the 399 nm beam pulses again in order to correct the two other pictures for light originating from the detection beam scattering off the windows and walls of the chamber.

The clock laser frequency is then determined based on the measured excitation fraction, and a new shot is initiated.

The clock laser is locked to the atomic transition by correcting the frequency based on the excitation probability measured in each shot. This is possible because we know the underlying probability distribution, which makes us able to calculate the detuning.

In the Yb clock we use two different excitation schemes; Rabi interrogation and Ramsey interrogation, each with its own distinct probability distribution. Both are mentioned here, since some of the data presented later was taken with the Rabi scheme, while other data was taken with the Ramsey scheme.

The Rabi scheme uses a coherent $\pi$ pulse to excite atoms from the ground state to the excited state, and has the distribution:

$$P_e = \left| \frac{\Omega}{\Delta^2 + \Omega^2} \right|^2 \sin^2 \left( \frac{\sqrt{\Delta^2 + \Omega^2}}{2} \tau \right). \qquad \text{(reprint of Equation 2.11)}$$

An excitation using the Rabi scheme with $\tau = 300$ ms can be seen on Figure 4.15 as a function of detuning ($\frac{\Delta}{2\pi}$). The blue points are data and the green

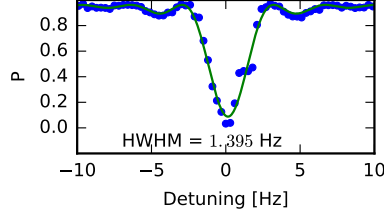line is a fit with the equation above. For this particular spectrum the clock was running in inverted mode.



**Figure 4.15:** *Spectrum taken with the 300 ms Rabi interrogation in inverted mode. The blue is data and the green is a fitted model, with the center and $\Omega$ as the only free parameters.*
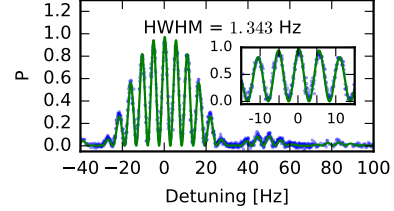
**Figure 4.16:** *Spectrum taken with the Ramsey scheme using $\tau_p = 30$ ms and $T = 150$ ms. The blue is data and the green is a fitted model, with the center and $\Omega$ as the only free parameters. The insert is a zoom of the central fringes.*

The Ramsey scheme is slightly different. It relies on coherently driving the atoms with two $\frac{\pi}{2}$-pulses, separated by a "dark time" where the clock laser is off or off resonant. The first $\frac{\pi}{2}$ pulse brings the atoms into a 50/50 superposition of ground and excited state. During the dark time the atoms pick up a phase relative to the clock laser depending on their detuning. Finally another $\frac{\pi}{2}$ pulse drives the atoms into something between the fully excited state and the ground state depending on the phase. The Ramsey excitation probability is given[23] as:

$$P_e(\tau_p, T) = 4\frac{\Omega^2}{\Delta^2 + \Omega^2}\sin^2\left(\frac{\sqrt{\Delta^2 + \Omega^2}\,\tau_p}{2}\right)\left[\cos\left(\frac{\Delta T}{2}\right)\cos\left(\frac{\sqrt{\Delta^2 + \Omega^2}\,\tau_p}{2}\right)\right.$$
$$\left. - \frac{\Delta}{\sqrt{\Delta^2 + \Omega^2}}\sin\left(\frac{\Delta T}{2}\right)\sin\left(\frac{\sqrt{\Delta^2 + \Omega^2}\,\tau_p}{2}\right)\right]^2$$
$$(4.3)$$

Here $\tau_p$ is the pulse length of one of the $\frac{\pi}{2}$ pulses and $T$ is the time between the two pulses, also called the dark time.

Figure 4.16 shows the excitation probability for $\tau_p = 30$ ms and $T = 150$ ms, note that the detuning in the plot is in frequency whereas the detuning $\Delta$ in Equation 4.3 is in angular frequency.

The fringes in Figure 4.16 appear because the phase picked up during the dark time goes from zero at zero detuning, to $\pi$ at the first minimum, to $2\pi$ at the first maximum away from the center and to $3\pi$ at the second minimum, and so on. We see that the width of the center fringe is comparable to the 300 ms Rabi pulse.

To lock the laser to the atomic transition we choose a pulse time $\tau$ (or $\tau_p$ and $T$) and detune the clock laser by HWHM of the calculated probability distribution.

After a shot, we use the measured excitation fraction to determine how far we are away from the 50% point and correct the clock laser for this. We use

the 50% points because it makes us able to differentiate between being detuned too high or too low, and because the slope is largest here. This also makes a more narrow linewidth desirable since it increases the slope which improves the lock performance in the precense of noise.

In practice we cannot make the pulse length infinitely long as we are limited by the short term stability of the clock laser. If the clock laser frequency changes too much during the pulse we will loose the coherent excitation and thus the contrast of the fringe.

Initially the clock was running with the Rabi scheme but later retro fitted to use the Ramsey scheme after the new lattice configuration was implemented.

Due to space constraints a shutter could not be placed between the FNC reference surface and the curved mirror. This makes it impossible to turn the clock laser off during the Ramsey interrogation dark time without turning off the FNC system which is necessary to avoid loosing the coherence due to phase noise in the clock laser. It is instead detuned  200 kHz which, because the line width of the transition is so narrow, essentially eliminates any interaction.

During the dark time the power of the clock laser is reduced but limited by the minimum power needed for the FNC system.

The full setup can be seen on Figure 4.19. Two timing diagrams, one representing Ramsey interrogation in non inverted mode and one representing Rabi interrogation in inverted mode can be seen in Figure 4.17 and Figure 4.18. The absence of a radial settling pulse in Figure 4.18 is because it was not implemented when the experiments using Rabi interrogation in inverted mode were conducted.
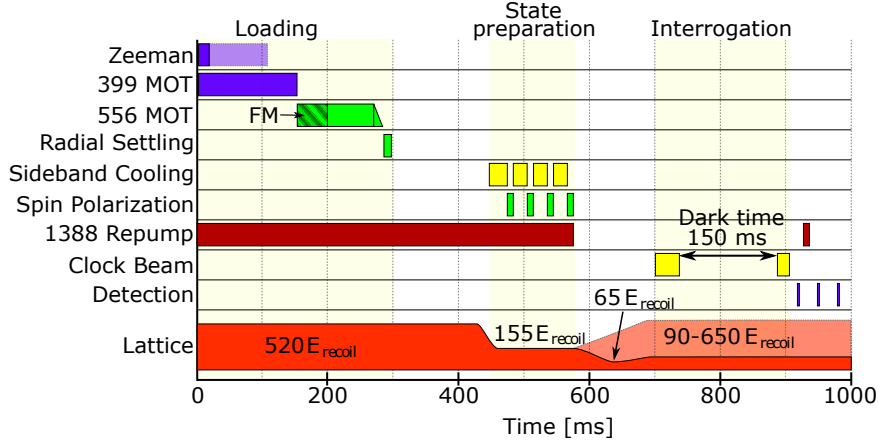


**Figure 4.17:** *The timing diagram for a typical sequence using Ramsey interrogation. The atoms are first slowed by the Zeeman slower and then cooled by the first and second stage MOT. During loading the lattice trap depth is* 520 $E_{recoil}$. *It is ramped to* 155 $E_{recoil}$ *before the clock state preparation and then, depending on whether the interrogation trap depth is above or below* 200 $E_{recoil}$, *dipped to* 65 $E_{recoil}$ *to remove any atoms with enough radial energy to bring them close to the edge of the trap. This timing diagram shows the Ramsey interrogation scheme with two pulses with a dark time of* 150 ms *in between.*
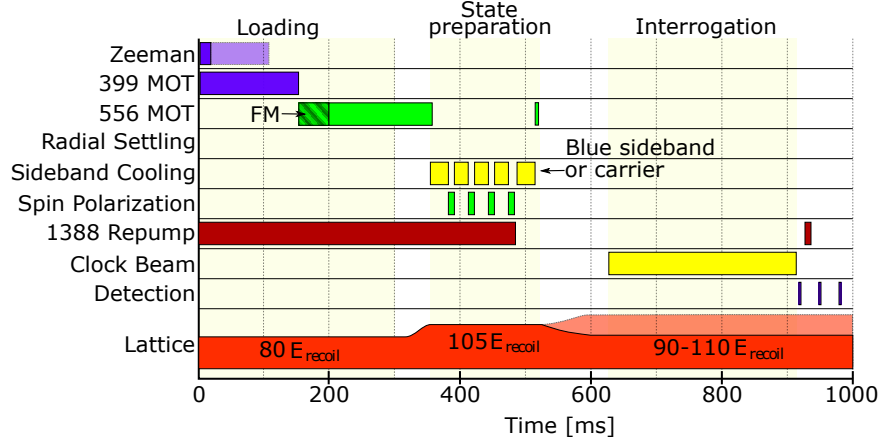
**Figure 4.18:** *The timing diagram for a typical sequence using Rabi interrogation in inverted mode. The atoms are first slowed by the Zeeman slower and then cooled by the first and second stage MOT. During loading the lattice trap depth is 80 $E_{\mathrm{recoil}}$ and is then ramped to 105 $E_{\mathrm{recoil}}$ before the clock state preparation. After the spinpolarization the atoms are excited on either the blue sideband or the carrier and a high power 556 nm pulse is used to clear out the ground state. The lattice is then ramped to the desired interrogation trap depth. The clock excitation is done with a 300 ms Rabi pulse.*
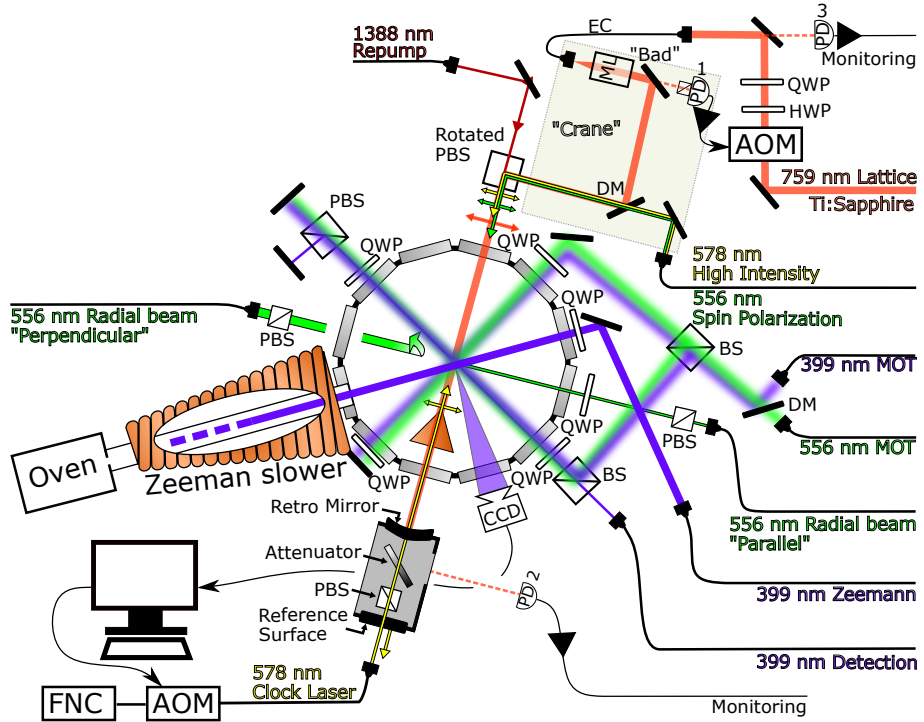


**Figure 4.19:** *The experimental setup for the Yb clock not including the systems generating the lasers involved. Figure 4.2 through Figure 4.14 explain each component in detail.*
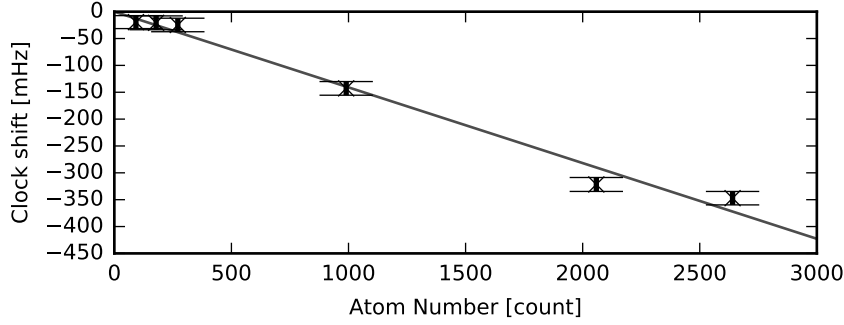
**Figure 4.20:** *A plot of the clock transition shifts arising from varying only the atom number in the lattice. We see that they follow a linear tendency nicely.*

## 4.6 Minimizing collisional shifts

The reason for converting from Rabi interrogating to Ramsey interrogation was to suppress the effects of the collisional shifts we observed from having two atoms in the same lattice site even when spin polarizing the atoms. Other clocks have seen similar behavior and it has been suggested that the observed shifts arise from p-wave interactions between the atoms[10, 11]. As we only populate between 250-500 lattice sites with about the same amount of atoms, there are only at most a few of the sites with more than one atom.

The collisional effects have been studied in [28] and it is seen that by changing the pulse length of the first Ramsey pulse we can minimize the collisional induced shifts.

Figure 4.20 is a plot of the frequency shift arising from varying the atom number and we will for the work presented in this thesis assume that the collisional shifts are linear in atom number.

# 5

# Analyzing the data

## 5.1 Overview

The light shift model which we derived in Section 2.3 describes the expected AC stark shift on the clock transition that arises from the lattice laser:

$$
\begin{aligned}
\Delta\nu_{\text{clock}}^{\text{lattice}} = {} & \left(a\left(\nu_{\text{lattice}} - \nu_{\text{E1}}\right) - b\right)\left(n_{\text{avg}} + {}^1\!/_2\right)\sqrt{\left(\zeta_1 - \frac{1}{2}\delta\zeta\right)\frac{U_{\text{trap}}^0}{E_{\text{recoil}}}} \\
& - \left(a\left(\nu_{\text{lattice}} - \nu_{\text{E1}}\right) - \frac{3}{4}d(2n_{\text{avg}}^2 + 2n_{\text{avg}} + 1)\right)\zeta_1\frac{U_{\text{trap}}^0}{E_{\text{recoil}}} \\
& + d(2n_{\text{avg}} + 1)\left(\left(\zeta_1 + \frac{1}{2}\delta\zeta\right)\frac{U_{\text{trap}}^0}{E_{\text{recoil}}}\right)^{3/2} \\
& - d\left(\left(\zeta_1 + \delta\zeta\right)\frac{U_{\text{trap}}^0}{E_{\text{recoil}}}\right)^2. \qquad \text{(reprint of Equation 2.71)}
\end{aligned}
$$

The goal of our experiments is to determine the variables $a$, $b$, $d$ and $\nu\text{E1}$. This can be done by systematically varying the parameters $\nu_{\text{lattice}}$, $n_{\text{avg}}$ and $U_{\text{trap}}^0$ and measuring the resulting clock transition shift.

The lattice laser frequency $\nu_{\text{lattice}}$ is frequency locked to a frequency comb with a delay-line lock[22] and can be varied by changing the lock point.

The parameter $n_{\text{avg}}$ describes the axial energy level and can only be accuratly varied between $n = 0$ and $n = 1$ by running the clock in inverted mode as explained in Section 4.4.

$U_{\text{trap}}^0$ is the peak trap depth at the radial center of the lattice beam and can thus be varied by changing the lattice laser intensity. The two last parameters in the model $\zeta_1$ and $\delta\zeta$ are introduced to account for the radial motion of the atoms by averaging over the radial positions but in the experiments presented here we do not purposely vary these.

Close to the E1 magic frequency the resulting light shift from varying the lattice frequency, lattice intensity and $n_{\text{avg}}$ will only shift the clock transition

frequency on the order of one to hundreds of millihertz. It is therefore easier
to measure the frequency of the AOM controlling the clock laser than the
frequency of the clock laser itself since the clock transition is on the order of
hundreds of terahertz. However, since the clock laser is pre-stabilized to a
reference cavity which changes slowly over time the AOM has to continuously
correct for this to keep the clock laser resonant with the atomic transition.

One solution is to build two identical clocks using two independent clock
lasers stabilized to the same cavity. If we then calculate the difference be-
tween the AOM frequencies of the two clock lasers the cavity change would be
identical for both of them and thus disappear.

Instead of building two clocks we could run a single clock and apply the
correction calculated for shot 1 to shot 3, and the correction calculated for
shot 2 to shot 4. If the short term drift of the cavity between two shots is
negligible we can calculate the frequency difference between the even and odd
shots and any long term cavity drift will again be common and disappear. This
way of locking the clock laser twice but independently to the atoms is called
interleaved measurement.

We run one 'collection' of shots one set of parameters, and another collection
with another set of parameters. The frequency difference between the two
collections is then the difference in light shift predicted by the light shift model
for the two sets of parameters.

Some of our measurements expand on the idea of interleaved measurements
and run 4 collections at a time. We then run two sets of parameters with both
a high and a low atom density. Because a higher atomic density increases the
chance of having more than one atom per lattice site we can use the frequency
difference between a high density and low density measurement to determine
any shift caused by collisions.

An illustration of how the interleaved measurements are performed can be
seen on Figure 5.1 where each color represents a set of parameters. The black
line is the order the measurements are done in, while the colored lines represent
how the data is connected.

The experimental data was taken in 6 groups with two or three days of
measurements in each group. Between groups many of the lasers were powered
down and realigned before the beginning of a new group.

The first two groups focused on measuring the resulting frequency shift be-
tween having $n = 0$ and $n = 1$ at low peak trap depth at multiple different
lattice frequencies around the magic frequency. Under these operating condi-
tions the light shifts will be dominated by the first term in the light shift model.
Varying $n$ is therefore a good way of determining the multipolarizability $b$.

The multipolarizability measurements were conducted in "inverted" mode,
as described in Section 4.4, in order to obtain $n = 1$. The clock pulse was
using the Rabi scheme with a pulse length of 300 ms and the settling pulses
described in Section 4.3 were not implemented when these measurements were
taken. The timing diagram for these measurements is Figure 4.18.

The last four groups were used to vary the peak trap depth over a large
range from 85 $E_{\mathrm{recoil}}$ to 650 $E_{\mathrm{recoil}}$ at 7 different lattice frequencies. At high
peak trap depths the light shift model will be dominated by the last term which
makes it easy to determine the hyperpolarizability $d$. By varying the lattice
frequency we also get a good estimation of $a$.
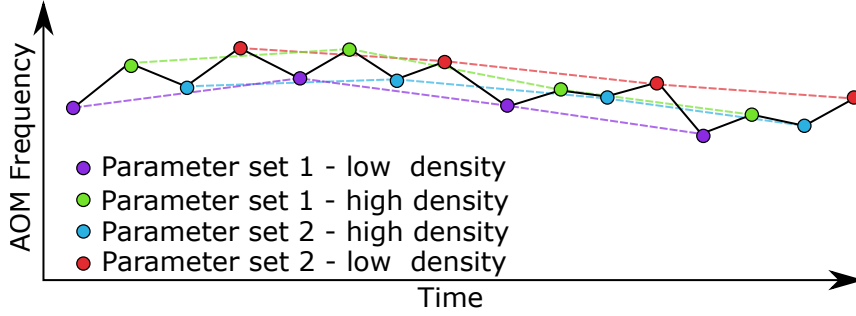
**Figure 5.1:** *An illustration of how the interleaved measurements are done. Each color represents a specific set of parameters. The black line represents the order the measurements are done in, while the colored, dashed lines represent the order they are split into when analysing the data.*

| Group nr | Date | Parameter of interest | Probe | Probe timings | Operation mode |
|---|---|---|---|---|---|
| 1 | Aug 15-16 | Multipolarizability | Rabi excitation | 300 ms | 'inverted' |
| 2 | Aug 27-29 | | | | |
| 3 | Nov 09-10 | Hyperpolarizability | Ramsey excitation | $\tau_1 = 38.6$ ms $T = 150$ ms $\tau_2 = 21.4$ ms | 'non inverted' |
| 4 | Nov 18-20 | | | | |
| 5 | Nov 21-23 | | | | |
| 6 | Nov 24-26 | | | | |

**Table 5.1:** *Overview of the 6 groups of measurements performed to determine the variables of the light shift model.*

These measurements were not done in "inverted" mode and used the Ramsey scheme with the first pulse being 38.6 ms, the dark time being 150 ms, and the second pulse being 21.4 ms. The timing diagram for the Hyperpolarizability measurements is seen on Figure 4.17.

As mentioned earlier the peak trap depth can be changed by controlling the lattice laser intensity. This was controlled by software by changing the lock point of the lattice power feedback control mentioned in Section 4.1. Due to the issues mentioned in the same section this does not necessarily keep the lattice intensity in the vacuum chamber constant, so to determine the actual lattice intensity we make use of the relation between trap depth and intensity mentioned in Section 2.2 and take a spectrum which is broad enough to capture the sideband structure. By analyzing the sideband spectrum we can extract not only the trap depth $U_{\mathrm{trap}}$ but also the average energy level $n_{\mathrm{avg}}$ and the intensity reduction parameters $\zeta$ and $\delta\zeta$. This is detailed in Section 5.3.

To precisely measure the frequency shift arising from varying the parameters we must average over many repeated measurements to decrease the statistical uncertainty. The analysis of a frequency shift measurement is presented in Section 5.2.

## 5.2    Interleaved measurement analysis

We do interleaved measurements to determine the frequency shift arising from
varying different parameters in the light shift model, namely the trap depth
$U_0$, the vibrational level $n$ and the frequency of the lattice $\nu_{\text{lattice}}$.

   This section will go through the data analysis of a measurement that used
four trackers: two at a low trap depth of 82 $E_{\text{recoil}}$ but at two different atom
numbers, and two at a higher trap depth of 330 $E_{\text{recoil}}$ also with different atom
numbers.  We ran a high and low atom number version of the same set of
parameters because this allows us to estimate the collisional shifts which the
light shift model does not take into account.

   As explained earlier we do not measure the absolute frequency of the clock
transition but rather the difference between two 'collections' of shots.  This
means all frequency shifts are measured relative to some set of parameters
which we try to keep constant over all the measurements. The low trap depth
measurements are denoted the reference point and the high trap depth are
denoted the measurement point. For the measurements that varied the vibra-
tional level $n$ instead of the trap depth, the reference point is $n = 0$ and the
measurement point is the $n = 1$.

### 5.2.1    Measurement scheme

The clock states $^1S_0$, and $^3P_0$ have two magnetic substates $m_F = \pm\frac{1}{2}$.  By
using $\pi$ polarized light we can target either the $^1S_0, m_F \frac{1}{2} \leftrightarrow {}^3P_0, m_F \frac{1}{2}$ or the
$^1S_0, m_F - \frac{1}{2} \leftrightarrow {}^3P_0, m_F - \frac{1}{2}$ transition which are separated by $\sim 340$ Hz during
interrogation due to the bias B-field.

   In order to cancel out any first order Zeeman shifts arising from variations
in the magnetic field, we measure both Zeeman transitions, alternate between
the two sides of the fringe, creating a 4-step cycle on top of the interleaved
measurement scheme. This is illustrated on Figure 5.2 and Figure 5.3.
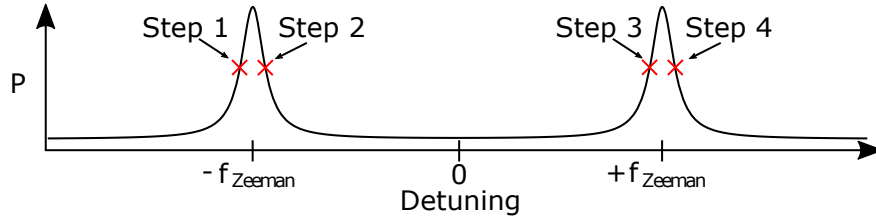


**Figure 5.2:** *The cycle of 4 shots that each tracker repeats. This probes the left and
right side and the two Zeeman substates alternating.*

   A plot of the raw data can be seen on Figure 5.4, where the blue points are
the frequency correction applied to the clock laser AOM and the green points
are the atom number.  If something happens that causes the clock laser to
not lock to the atomic frequency, we remove those datapoints. For the large
gap in this dataset the ultra stable cavity which the clock laser is locked to
became unstable.  The clock kept repeating shots but failed to lock to the
atomic transition. As no parameters or environmental factors changed during
the missing time we assume that the conditions before and after the missing
time were identical and stick the two sets of data together.
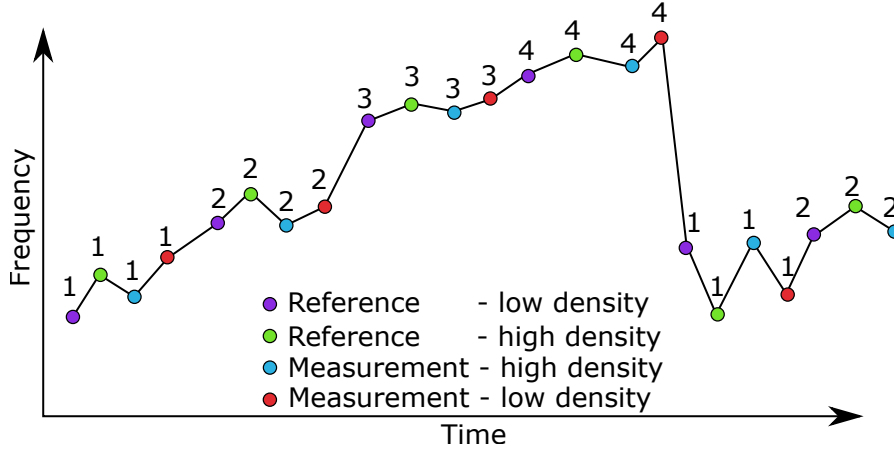
**Figure 5.3:** *The interleaved measurement scheme, with the 4-step cycle included for clarity. In this example we run 4 collections at the same time, but it is possible to run fewer.*
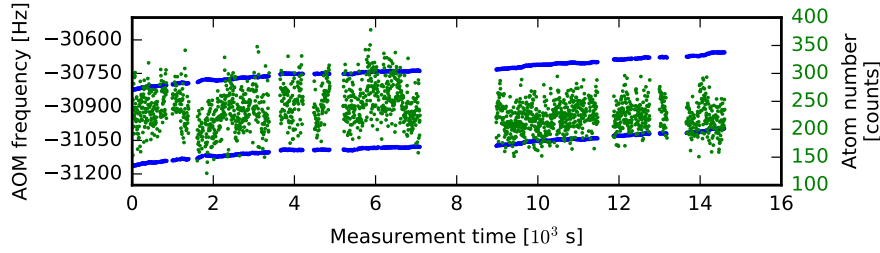


**Figure 5.4:** *The raw data from a clock measurement. The blue points are the frequency corrections applied to the clock laser AOM and the green points are the clock laser AOM frequency. The points are split into two bands, one for each Zeeman substate. The green points are the atom number.*

The AOM frequency is split into two bands because we alternate between measuring the two Zeeman components. Each of the two bands are in turn split into two bands, one for each side of the fringe. We separate the raw data into independent collections of shots and remove all shots that have too low or too high excitation probabilities because there always is a small loss of contrast limiting the range of excitations we can expect to measure.

### 5.2.2   Determining the frequency of a collection of shots

From the measured excitation probability $P$ we can calculate the detuning of each shot from the Zeeman substate resonance. This is done in two different ways depending whether we used the Ramsey or Rabi scheme for interrogation.

For Ramsey interrogation we invert the expression for Ramsey excitation

so it becomes a function of excitation probability:[23]

$$P = \cos\left(2\pi\Delta f_{\text{clock}}T\right), \tag{5.1}$$

$$\Delta f_{\text{clock}} = \frac{1}{2\pi T}\cos^{-1}\left(2P - 1\right) \tag{5.2}$$

which is only good for small detunings. Here $T$ is the time between the beginning of the first and the second $\frac{\pi}{2}$ pulse. The Ramsey line shape for $T = 180$ ms is plotted as a blue line on Figure 5.5 with the inverse plotted in green on top.

For Rabi interrogation it is a bit more tricky since the Rabi excitation probability is not easily invertible:

$$P = \left|\frac{\Omega}{\left(2\pi\Delta f_{\text{clock}}\right)^2 + \Omega^2}\right|^2 \sin^2\left(\frac{\sqrt{\left(2\pi\Delta f_{\text{clock}}\right)^2 + \Omega^2}}{2}\tau\right),$$

(reprint of Equation 2.11)

Instead we use interpolation to construct a model which is the inverse of $P$:

$$\Delta f_{\text{clock}}(P) = \mathcal{F}(P). \tag{5.3}$$

The interpolated function is plotted with green on Figure 5.6 on top of the line shape for a Rabi pulse of $\tau = 300$ ms.
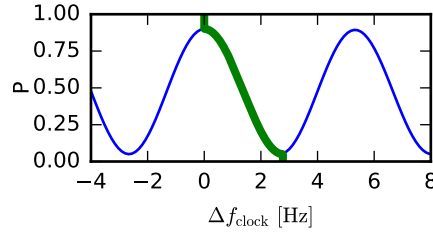


**Figure 5.5:** *A plot illustrating the inverse Ramsey line shape (green) on top of the Ramsey line shape (blue) with $T = 180$ ms.*
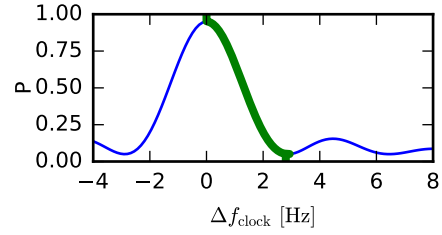
**Figure 5.6:** *A plot illustrating the inverse Rabi line shape (green) on top of the Rabi line shape (blue) with $T = 300$ ms.*

Using either the inverse Ramsey or Rabi excitation equation we can calculate the detuning from the excitation probability in two different ways depending on what side of the fringe we measured. By combining this with the measured AOM frequency we can calculate the line center of the resonance:

$$f_{\substack{\text{line} \\ \text{center}}} = \begin{cases} f_{\text{AOM}} - \Delta f_{\text{clock}}\left(P\right) & \text{Step 1 and 3} \\ f_{\text{AOM}} + \Delta f_{\text{clock}}\left(P\right) & \text{Step 2 and 4} \end{cases} \tag{5.4}$$

This can be seen on Figure 5.7 where the crosses are the measured AOM frequency ($f_{\text{AOM}}$), the numbers represent the measured excitation probability $P$ and the dots are the calculated $f_{\substack{\text{line} \\ \text{center}}}$. Note that the the y-axis of Figure 5.7 is broken half way. This is done to illustrate both of the Zeeman substates on the same plot. The calculated $f_{\substack{\text{line} \\ \text{center}}}$ are always centered between the $f_{\text{AOM}}$ points because the latter measure the side of the fringe and not the center, as explained in Figure 5.2.
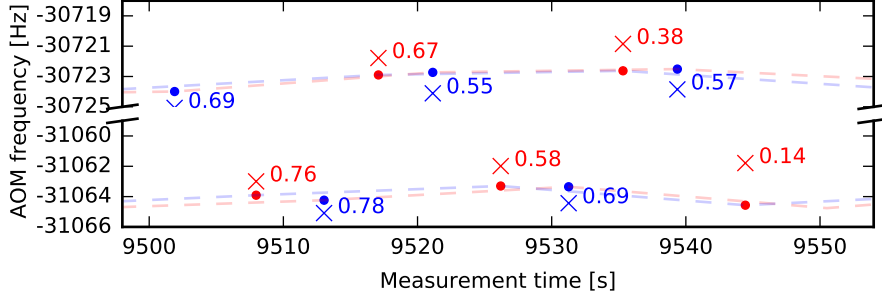
**Figure 5.7:** *A plot of the measured AOM frequency (cross) and the calculated Zeeman line center frequency (dot). The numbers are the measured excitation probability P for that shot. The dashed lines are the linear interpolation to the calculated Zeeman line center for each group of points.*

We now use the four points to calculate the center frequency, i.e. the AOM frequency that would have been required to make the clock laser resonant with the transition if there was no magnetic field and thus no Zeeman splitting:

$$f_{\text{center}} = \frac{1}{2} \left( \frac{f^{(1)}_{\substack{\text{line} \\ \text{center}}} + f^{(2)}_{\substack{\text{line} \\ \text{center}}}}{2} + \frac{f^{(3)}_{\substack{\text{line} \\ \text{center}}} + f^{(4)}_{\substack{\text{line} \\ \text{center}}}}{2} \right), \qquad (5.5)$$

but because the shots are taken consecutively we first interpolate between the points. This can be see as the four dashed lines in Figure 5.7. With these interpolations we can then calculate the center frequency:

$$f_{\text{center}}(t) = \frac{1}{2} \left( \frac{F^{(1)}_{\substack{\text{line} \\ \text{center}}}(t) + F^{(2)}_{\substack{\text{line} \\ \text{center}}}(t)}{2} + \frac{F^{(3)}_{\substack{\text{line} \\ \text{center}}}(t) + F^{(4)}_{\substack{\text{line} \\ \text{center}}}(t)}{2} \right), \qquad (5.6)$$

where $F^i(t)$ represents the interpolation function for step $i$, evaluated at time $t$. By interpolating we get a calculated $f_{\text{center}}$ for each shot as illustrated in Figure 5.8.

By calculating the mean of the Zeeman line centers for every point individually we cancel out any fluctuations or variations in the magnetic field that might cause the Zeeman splitting to change over time.

Figure 5.9 shows the calculated $f_{\text{center}}$ for the entire data set. The slow change over time is due to the length of the stabilizing cavity changing, and is what prevents us from using this calculated value to determine the clock transition frequency.

### 5.2.3    Comparing trackers

As explained earlier we do interleaved measurements to combat the exact problem with the drift seen in Figure 5.9. By looking at the difference between the calculated center frequency for the reference point shots and the measurement
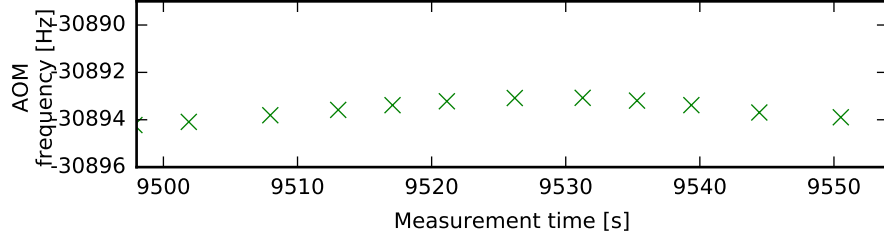
**Figure 5.8:** *The calculated $f_{\text{center}}$ based on the interpolation of the Zeeman line centers.*
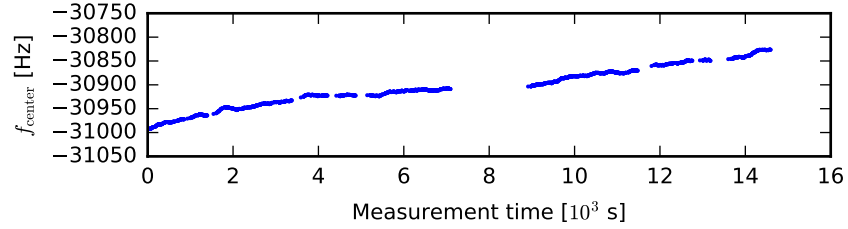


**Figure 5.9:** *The calculated AOM frequency needed to make the clock laser resonant with the atomic transition in the absence of any magnetic fields.*

points shots we can determine the frequency shift:

$$f_{\text{clock}}^{\text{diff}} = f_{\text{center}}^{\text{meas}} - f_{\text{center}}^{\text{ref}}. \tag{5.7}$$

Since the shots of the two trackers were taken at different times we interpolate again, but this time only for the reference data:

$$f_{\text{clock}}^{\text{diff}}(t_i) = f_{\text{center}_i}^{\text{data}} - F_{\text{center}}^{\text{ref}}(t_i), \tag{5.8}$$

where the subscript $i$ refers to the $i$'th time stamp of the measurement tracker. The clock frequency difference between the low density reference tracker and the low density measurement tracker is plotted on Figure 5.10 where we see that the cavity drift is no longer visible. By averaging over the entire measurement period we find a mean clock frequency difference of:

$$\langle f_{\text{clock}}^{\text{diff}} \rangle = 215.1 \text{ mHz} \tag{5.9}$$

To help estimate the uncertainty of the measured frequency difference, we calculate the overlapping Allan deviation as recommended in [21]. The Allan deviation is a two sample variance, which separates a time series into $M$ bins, each of a length $\tau$, and calculates the average difference between adjacent bins. The overlapping Allan deviation differs from the normal Allan deviation by creating additional bins by changing the starting point of the first bin. This can create $m$ extra bins, where $m$ is one less than the number of points in each bin, as illustrated on Figure 5.11 taken from [21].
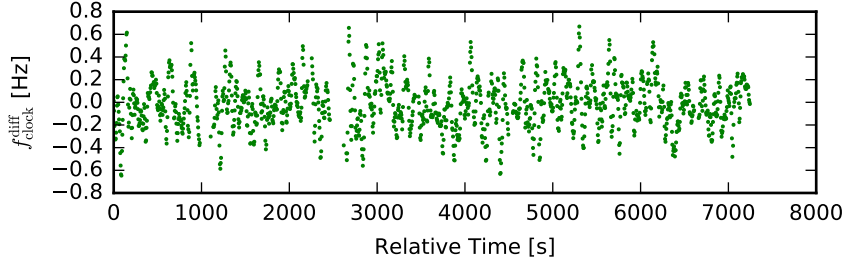
**Figure 5.10:** *The difference in AOM frequency between two trackers. Since the cavity drift is common for both trackers the frequency difference must come from the difference in operating parameters for the two trackers. For this data the reference shots used a trap depth 82 $E_{\text{recoil}}$ and the measurement shots used a trap depth of 330 $E_{\text{recoil}}$.*
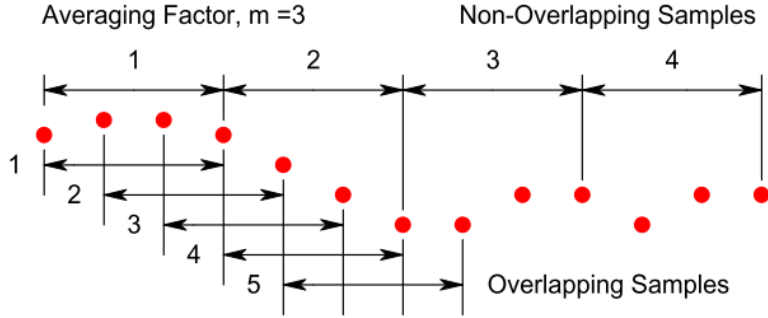


**Figure 5.11:** *An illustration of Overlapping Allan deviation compared to the normal Allan deviation. Taken from [21].*

The overlapping Allan variance, which is just the square of the Allan deviation, can be calculated by:

$$\sigma_f^2(\tau) = \frac{1}{2m^2 \left( M - 2m + 1 \right)} \sum_{j+1}^{M-2m+1} \left( \sum_{i=j}^{j+m-1} \bar{f}_{i+m} - \bar{f}_i \right), \qquad (5.10)$$

where $\langle f \rangle_k$ is the average of bin $k$. Figure 5.12 contains a plot of the overlapping Allan deviation of the data in Figure 5.10.

The error bars, which represent the 68% confidence interval, are calculated by first estimating the degrees of freedom, which varies depending on noise type. For white frequency modulation noise a good approximation is[21]:

$$\text{dof} = \left( \frac{3(M)}{2m} - \frac{2(M-1)}{M+1} \right) \frac{4m^2}{4m^2 + 5} \qquad (5.11)$$

The confidence interval can then be calculated as:

$$\sigma_{\min} = \sigma_f^2 \frac{\text{dof}}{\chi^2(p, \text{dof})} \quad \text{and} \quad \sigma_{\max} = \sigma_f^2 \frac{\text{dof}}{\chi^2(1-p, \text{dof})} \qquad (5.12)$$

where $\chi^2$ is the chi-squared distribution, and $\sigma_{\min}$ and $\sigma_{\max}$ are the lower and upper values $\sigma_f$ at the confidence limit $p$.

The Allan deviation is an excellent tool to determine the stability of a measurement and is therefore widely used when analyzing the data from clocks. For our purpose we wish to average over many repeated measurements to determine the measures frequency shift as accurately as possible. In order to do so we need to be certain the measured shift is stable in time and the Allan deviation in Figure 5.12 tells us exactly that.

We see that from $\tau = 40$ and onward the Allan deviation seems to follow a $\frac{1}{\sqrt{\tau}}$ slope and even though the last few points in Figure 5.12 behave strangely,, the uncertainties are also so large that it is difficult to make any definite claims.

When analyzing the frequency differences from the rest of the data sets we see a change in the day to day stability where measurements taken on the same day show very similar stabilities. We therefore find a region in the Allan deviation that seems representative of the stability on that given day, and use this to extrapolate the final uncertainty.

For this data set (and the others taken together with it) we choose the region from $\tau = 60$ to $\tau = 300$ and make the assumption that the clock stability will improve as $\frac{1}{\sqrt{\tau}}$ from here. This is marked by the dashed line in Figure 5.12.

When extrapolating to the full measurement length we get an uncertainty of 12.5 mHz, leading to a frequency difference between the low density reference tracker and the low density measurement tracker of:

$$\left\langle f_{\text{clock}}^{\text{diff}} \right\rangle = 215.1 \text{ mHz} \pm 12.5 \text{ mHz}. \tag{5.13}$$
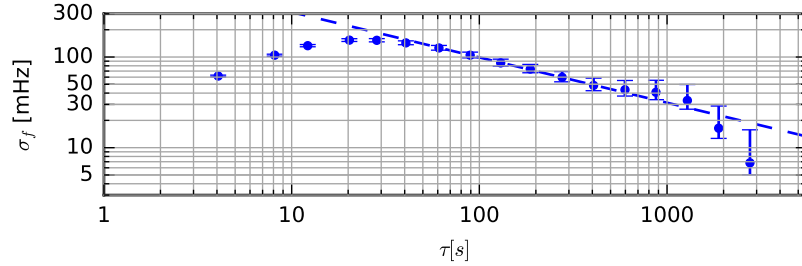


**Figure 5.12:** *The overlapping Allan deviation plot of the data in Figure 5.10. The dashed line indicates a $\frac{1}{\sqrt{\tau}}$ slope.*

### 5.2.4  Correcting for collisional shifts

As mentioned earlier we assume that the collisional shifts are linear in atom number and correct for them by running a high density and low density version of the two parameter sets being investigated.

The frequency difference between the high and low density versions are summarized in Table 5.2. By assuming the collisional shifts are linear in atom number we calculate a correction for both the low trap depth (ref) and high trap depth measurement (meas). To apply this correction to the frequency

| Trap depth | Clock frequency difference | Atom number | Collisional shift correction |
| --- | --- | --- | --- |
| Low | 30.3 mHz ± 6.2 mHz | 233 vs 104 | 24.99 mHz ± 2.0 mHz |
| High | 11.8 mHz ± 8.0 mHz | 218 vs 85 | 7.5 mHz ± 1.7 mHz |

**Table 5.2:** *The result from comparing low atom number and low trap depth with high atom number and low trap depth (Low) and comparing low atom number and high trap depth with high atom number and high trap depth. The last column shows the extrapolation to zero atom number.*

difference between the two measurements we must add one and subtract the other:

$$
\begin{aligned}
\left\langle f_{\text{clock}}^{\text{diff}} \right\rangle &= \left\langle f_{\text{clock}}^{\text{meas}} \right\rangle - \left\langle f_{\text{clock}}^{\text{ref}} \right\rangle \\
&= \left( \left\langle f_{\text{clock}}^{\text{meas}} \right\rangle + f_{\text{correction}}^{\text{high}} \right) - \left( \left\langle f_{\text{clock}}^{\text{ref}} \right\rangle + f_{\text{correction}}^{\text{low}} \right) \\
&= (215.1 \text{ mHz} + 7.5 \text{ mHz}) - (0 \text{ mHz} + 24.99 \text{ mHz}) \\
&= 197.7 \text{ mHz}
\end{aligned}
\tag{5.14}
$$

And the uncertainties add in quadrature:

$$
\sigma_{f_{\text{clock}}^{\text{diff}}} = \sqrt{12.5^2 + 1.7^2 + 2.0^2} \text{ mHz} = 12.8 \text{ mHz}
\tag{5.15}
$$

The final result of the collisional shift corrected frequency difference measurement for this data set is then:

$$
\left\langle f_{\text{clock}}^{\text{diff}} \right\rangle = 197.7 \text{ mHz} \pm 12.8 \text{ mHz}
\tag{5.16}
$$

## 5.3   Sideband spectrum analysis

To determine the parameters $U_{\text{trap}}^0$, $n_{\text{avg}}$, $\zeta$ and $\delta\zeta$ we take a spectrum wide enough to resolve the sidebands.

For the atoms trapped in a lattice we expect a spectrum like the one in Figure 2.7 (reprinted on page 59).

The data of such a spectrum can be seen on Figure 5.13, where the black points are the excitation probability $P$ and the green points are the total atom number. We have removed all points with an atom number below a certain threshold[1] because this is due to technical issues preventing us from succesfully loading atoms into the lattice. The data is then binned in frequency and smoothed by a symmetric moving average filter with a width of three bins.

We see that while the carrier in Figure 5.13 looks like the carrier in Figure 2.7, the red and blue sidebands look significantly different both in width and in height.
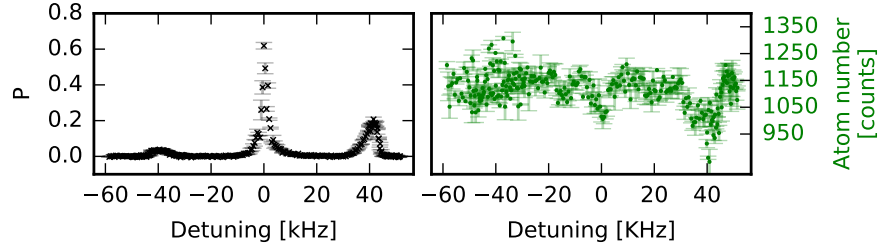


**Figure 5.13:**  *The raw data binned in frequency and with a moving average filter applied. The data points with atom numbers below the threshold have been removed. The error bars represent the standard deviation of the points in each bin.*

As the peak of the red sideband is much lower than the peak of the blue sideband, it indicates most of the atoms are not able to make a transition to a lower vibrational ground state. This means we must have more atoms in $n = 0$ than in $n = 1, 2, 3 \ldots$, which is to be expected because the spectrum in Figure 5.13 is taken on a sample of atoms which have been cooled by the resolved motional sideband cooling technique described in Section 4.3.

As evident of the nonzero excitation probability in the red sideband not all atoms are in $n = 0$. Since it is evident that only a small fraction of the atoms are in $n > 0$ we can estimate the average vibrational level $n_{\text{avg}}$ by comparing the area of the blue and red sideband:

$$n_{\text{avg}} = \frac{A_{\text{red}}}{A_{\text{blue}}}. \tag{5.17}$$

Also, the width of both the red and the blue sideband in Figure 5.13 is much wider than expected from Figure 2.7 and has a shape that extends inwards towards the carrier. This is due to the atoms only being tightly confined along the lattice axis as explained in Section 2.2.2 which leads to the axial trap

---

[1]This threshold is determined individually for each spectrum and is for this data 200 atoms.
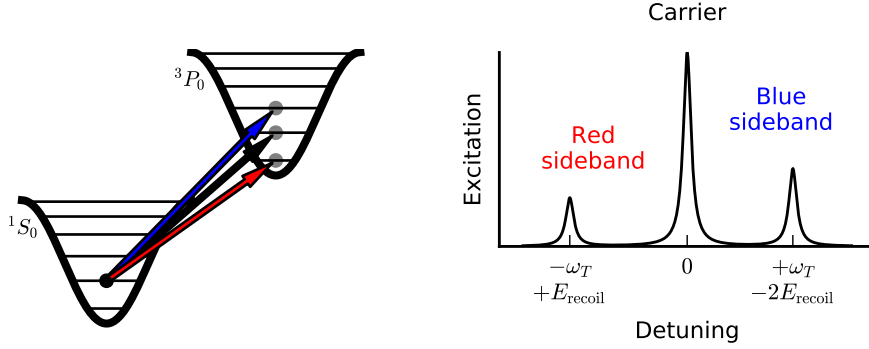
**Figure 2.6:** *An illustration of excitation of the atom in an optical lattice well. The atom starts in n = 1 and can be excited to three different final vibrational states depending on the frequency of the laser. (From page 14)*

**Figure 2.7:** *Spectrum of the sideband excitation for an atom starting in n = 1. (From page 14)*

frequency changing with the atoms radial movement in the lattice because the instantaneous trap depth changes:

$$\nu_T = 2\sqrt{\frac{E_{\text{recoil}}}{h} \frac{U_{\text{trap}}}{h}}, \tag{5.18}$$

where we have rewritten Equation 2.23 from angular frequency $\omega_T$ to frequency $\nu_T$ to match the units of the raw data.

The highest trap frequency in the sideband represents the peak trap depth $U_{\text{trap}}^0$, and since the trap depth decreases symmetrically for atoms with a radial position on either side of the center the sideband in asymmetric.

All the sideband spectra used in our measurements are taken with a pulse length of 1 ms which is short enough to allow us to sample the distribution of radial positions which means the shape of the sideband contains information about the distribution of radial energies.
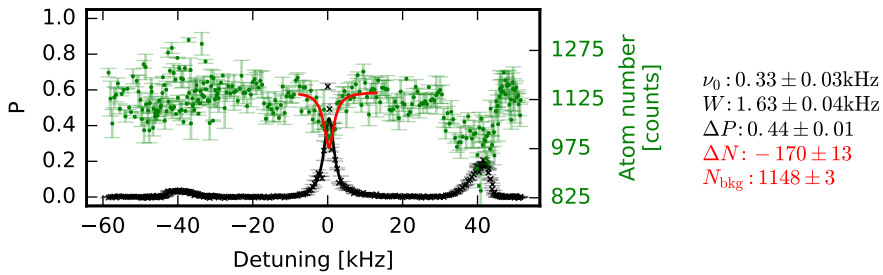


**Figure 5.16:** *The data fitted with Equation 5.19 to the excitation probability P (black line) and Equation 5.20 fitted to the atom number (red line). The numbers on the right hand side are the parameters from the two fits. $N_{\text{bkg}}$ is the atom number in the absence of any losses.*

### 5.3.1   Estimating the recovered fraction

As explained in Section 4.4, some of the excited atoms are lost when they are repumped to the ground state for detection either because they get heated by scattering or because they end in $^3P_2$. During measurements we assume that only a fraction of the excited atoms are recovered and factor this into the calculation of the excitation probability.

By looking at the correlation between the excitation probability and the atom number we can determine the exact fraction of lost atoms. We do this by first modeling the excitation probability of the carrier with a Lorentzian of the form:

$$\mathcal{P}(\nu) = \Delta P \frac{1}{1 + \left(\frac{(\nu - \nu_0)}{W}\right)^2} + P_{\mathrm{bkg}}, \tag{5.19}$$

The background $P_{\mathrm{bkg}}$ is not fitted but set to the expected value of zero.

We then use our model $\mathcal{P}$ to correlate the relative excitation probability to the atom number by fitting the atom number with:

$$\mathcal{N}(\nu) = \Delta N \frac{(\mathcal{P}(\nu) - P_{\mathrm{bkg}})}{\Delta P} + N_{\mathrm{bkg}}, \tag{5.20}$$

where the peak atom loss $\Delta N$ and the background $N_{bkg}$ are free parameters. The fit can be seen on Figure 5.16, where the black line is the fit of Equation 5.19 to the excitation probability $P$, and the red line is the fit of Equation 5.20 to the atom number. The parameter values from the two fits can be seen on the right hand side of Figure 5.16 and show a correlation between low atom number and high excitation probability.

The measured number of atoms in the excited state can be expressed as the total measured atom number multiplied with the calculated excitation probability:

$$N_e = N_{\mathrm{tot}} \cdot P. \tag{5.21}$$

Because of the loss during repumping this could also be expressed as:

$$N_e = P^{\mathrm{true}} \cdot N_{\mathrm{tot}}^{\mathrm{true}} \cdot R, \tag{5.22}$$

where $P^{\mathrm{true}}$ is the true excitation probability, $N_{\mathrm{tot}}^{\mathrm{true}}$ is the true total atom number, and $R$ is the fraction of atoms that were repumped without being lost. Using these two equations we can write up four equations, two for the atom number at the peak of the carrier, and two for the atom number at the background far away from the carrier:

$$\text{At peak} \begin{cases} N_e = N_{\mathrm{pk}} \cdot P_{\mathrm{pk}} = P_{\mathrm{pk}}^{\mathrm{true}} \cdot N^{\mathrm{true}} \cdot R \\ N_g = N_{\mathrm{pk}} \cdot (1 - P_{\mathrm{pk}}) = (1 - P_{\mathrm{pk}}^{\mathrm{true}}) \cdot N^{\mathrm{true}} \end{cases} \tag{5.23}$$

$$\text{At background} \begin{cases} N_e = N_{\mathrm{bkg}} \cdot P_{\mathrm{bkg}} = P_{\mathrm{bkg}}^{\mathrm{true}} \cdot N^{\mathrm{true}} \cdot R \\ N_g = N_{\mathrm{bkg}} \cdot (1 - P_{\mathrm{bkg}}) = (1 - P_{\mathrm{bkg}}^{\mathrm{true}}) \cdot N^{\mathrm{true}} \end{cases} \tag{5.24}$$

Here $P_{\mathrm{pk}} = \Delta P + P_{\mathrm{bkg}}$, $N_{\mathrm{pk}} = \Delta N + N_{\mathrm{bkg}}$, $N_e$ is the number of atoms in the excited state and $N_g$ is the number of atoms in the ground state.

We can then isolate $R$ in this set of equations to find an expression for the recovered fraction:

$$R = \frac{N_{\mathrm{bkg}} P_{\mathrm{bkg}} - N_{\mathrm{pk}} P_{\mathrm{pk}}}{N_{\mathrm{pk}} + N_{\mathrm{bkg}} P_{\mathrm{bkg}} - N_{\mathrm{bkg}} - N_{\mathrm{pk}} P_{\mathrm{pk}}}, \tag{5.25}$$

For the data plotted in Figure 5.16, we find $R = 0.73$ which fits nicely with the visible drop in atom number around the carrier.

To reduce the effect of measurement noise, we average over all the calculated $R$ for all the sidebands taken in a single group of measurements, and use this average to correct all the sideband spectra. The sideband spectrum analyzed here is chosen because it has a large, visible loss in atom number. It illustrates well how the loss correction is performed but is not part of the final data analysis. For the sideband data which we do use we commonly find $R_{\mathrm{avg}} \approx 0.9$ when averaged all the sideband spectra in a group.

The correction is applied across the entire spectrum, by correcting the excitation probability $P$ and atom number $N$:

$$P_{\mathrm{corr}} = \frac{N_e/R_{\mathrm{avg}}}{N_g + N_e/R_{\mathrm{avg}}}$$
$$N_{\mathrm{corr}} = N_e/R_{\mathrm{avg}} + N_g \tag{5.26}$$

The corrected data is then split into three parts: The blue, and red sideband data where the carrier contribution has been subtracted, and the carrier data itself.

The splitting of the data is plotted on Figure 5.17 were the black points are the data, the black line is the Lorentzian carrier fit and the red and blue points are the respective sideband data points with the carrier fit subtracted. In the plot of the atom number we no longer see a drop around zero detuning. There is still a visible loss of atoms around 40 kHz which we will take care of later.
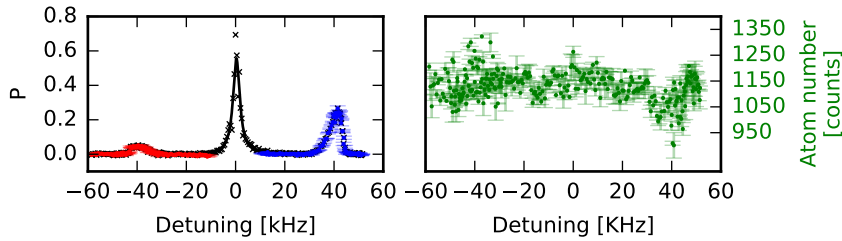


**Figure 5.17:** *The sideband data, split into carrier and red and blue sidebands. The red and blue points are the corrected data points with the Lorentzian carrier fit subtracted.*

To get the parameters $n_{\mathrm{avg}}$, $U_{\mathrm{trap}}^0$ and the radial energy distribution from which we can calculate $\zeta$ and $\delta\zeta$ we must model the sideband spectrum. This has previously been done by a method based on [4], but we present a different approach in the following sections.

### 5.3.2 Fitting the sidebands

We start by modeling the blue sideband by using a simple, but computationally heavy, technique to fit the blue sideband by simulating virtual atoms with

different radial positions and calculating the resulting spectrum from this. The advantage is that we require no assumption of the distribution of the atoms. Placing virtual atoms at different radial energies is akin to assigning them different instantaneous axial trap frequencies $\nu_T$ or placing them at different detunings in the sideband spectrum.

To estimate the contribution to the total spectrum from a single virtual atom we need the Rabi frequency. This can be found from the Rabi frequency of the carrier[2] modified by the matrix element dealing with the vibrational states (see Equation 2.37):

$$\Omega_{\text{SB}}(n_<, \Delta n, \eta) = \Omega_C \langle n' | e^{i\eta(a^\dagger + a)} | n \rangle = \Omega_C e^{-\frac{1}{2}\eta^2} \sqrt{\frac{n_<!}{(n_< + \Delta n)!}} \, (i\eta)^{\Delta n} L_{n_<}^{\Delta n} (\eta^2) \,,$$
(5.27)

where $\eta$ is the Lamb Dicke paramter:

$$\eta = \sqrt{\frac{E_{\text{recoil}}^p}{h\nu_T}} \,.$$
(5.28)

$\Omega_C$ is the carrier Rabi frequency found from the width (W) of the Lorentzian fit:

$$W = \Omega_C.$$
(5.29)

This equation is accurate in the regime where there is no dampening due to the long lifetime of the excited state, but where we still drive the atoms into saturation with an $\sim 5\pi$ pulse.[13].

Over all the sideband spectra we have taken at different lattice intensities, we see axial trap frequencies ranging between 20 kHz and 100 kHz. This leads to Lamb Dicke parameters between 0.19 and 0.41. With a carrier Rabi frequency of $2\pi \cdot 1.63$ kHz we can estimate the sideband Rabi frequencies from Equation 5.27:

$$\begin{aligned}
\Omega_{\text{SB}} &\sim 2\pi \cdot 220 \text{ Hz} \quad \text{at 100 kHz,} \\
\Omega_{\text{SB}} &\sim 2\pi \cdot 360 \text{ Hz} \quad \text{at 40 kHz.}
\end{aligned}$$
(5.30)

This means that while the carrier might be saturated by a 1 ms pulse the sidebands do not. We can also estimate the radial trap frequencies at the waist by rewriting Equation 2.43 from angular frequency:

$$\nu_T^{\text{radial}} = \sqrt{\frac{2U_{\text{trap}}^0}{\pi^2 m_{\text{atom}} w_0^2}} \,.$$
(5.31)

Note that this depends not on the instantaneous axial trap frequency but rather on the peak axial trap frequency ($\nu_T^0$) which ranges from 40 kHz to 100 kHz. With $w_0 = 44$ μm, $m_{\text{atom}} \approx 2.3 \cdot 10^{-25}$ kg and $U_{\text{trap}}^0 = \frac{(h\nu_T^0)^2}{4E_{\text{recoil}}}$ the radial trap frequency gives:

$$\begin{aligned}
\nu_T^{\text{radial}} &\sim 200 \text{ Hz} \quad \text{at 40 kHz,} \\
\nu_T^{\text{radial}} &\sim 500 \text{ Hz} \quad \text{at 100 kHz.}
\end{aligned}$$
(5.32)

---

[2]This is possible because the electronic dipole matrix element is identical for the carrier and the sidebands.

which means they move significantly during our 1 ms pulse. Since the atoms are both moving radially during the pulse and have a very low sideband Rabi frequency we cannot use the Lorentzian line shape from Equation 5.19 or the pure Rabi excitation (Equation 2.11) to model the spectrum of a virtual atom.

The radial movement is slow enough that the atoms will not oscillate back and forth multiple times. We can therefore picture it as atoms moving either into the center of the trap, or away from the center of the trap. Since the sideband Rabi frequency they perceive is larger the further they are away from the trap center, we model the excitation of the atoms as if they interacted with a shorter pulse, in this case half as long:

$$P_{\text{model}}(\Delta, \Omega_{\text{SB}}, \tau) = \frac{\Omega_{\text{SB}}}{\Delta^2 + \Omega_{\text{SB}}^2} \sin\left( \frac{\sqrt{\Delta^2 + \Omega_{\text{SB}}^2}}{2} \frac{\tau}{2} \right)^2 \qquad (5.33)$$

where $\tau$ is the pulse length of 1 ms and $\Delta$ is the detuning. The spectrum contribution for each virtual atom is then calculated from Equation 5.33 with:

$$\Delta = \nu - (\nu_T - \frac{E_{\text{recoil}}}{h})$$

$$n_< = 0 \quad \Delta n = 1 \quad \eta = \sqrt{\frac{E_{\text{recoil}}}{h\nu_T}}$$

$$\tau = 0.001 \text{ s} \qquad (5.34)$$

where $\nu_T$ is the instantaneous axial trap frequency, corresponding to the harmonic potential felt by the virtual atom. We assume initially that all virtual atoms are in $n = 0$ and subtract one unit of $E_{\text{recoil}}$ in the detuning because of the anharmonic correction, as described in Section 2.2.1, since this is the effective axial trap frequency of the virtual atoms.

The next part describes the computational steps done to model the sideband spectrum.

### Placing the virtual atoms

The first virtual atom is placed at the frequency corresponding to the largest observed excitation probability of the sideband, with the consecutive ones being placed randomly inside the sideband. We limit the number of initially placed virtual atoms to 10-20 based on the width of the sideband. This is far less than reality, but is limited to decrease the sensitivity to noise.

After each placement we sum the contributions from each atom over the entire frequency range to get a model spectrum. The model spectrum after placing two atoms can be seen on Figure 5.18a(i) where the blue points represent the sideband data. The thin green lines are the individual spectra from virtual atoms placed at two different trap frequencies and the black line is the combined spectrum from both atoms. Both the individual spectra and the combined spectrum have been renormalized to fit the data.

We estimate the goodness of our model renormalizing the model spectrum to fit the data and calculate the residual sum of squares between the two. Figure 5.18a(ii) shows a plot of the residuals. We reject the placement of new atoms if the sum of squares increases and continue to try to place atoms.

Figure 5.18b(i) shows the result of placing four virtual atoms. Note that the individual contribution from each virtual atom decreases as more atoms
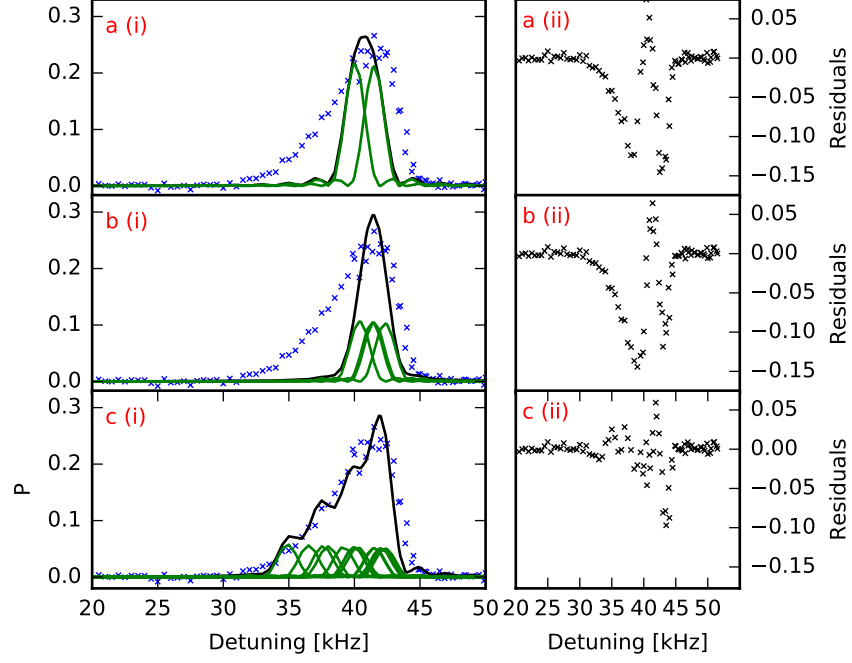
**Figure 5.18:** *These figures show the procedure of simulating virtual atoms with different trap frequencies to model the blue sideband. The blue points are the data points, the thin green lines are the spectra from the individual virtual atoms and the black line is the combined spectrum from all the virtual atoms. The black lines have been renormalized to match the data. a(i) shows the model with only two virtual atoms. The residuals in a(ii) is used to estimate how well our model fits the data. b(i) shows the model after placing four atoms. We see that b(ii) models the data better with four atoms. c(i) shows the spectrum after placing all the atoms. The model now fits nicely which is also evident from c(ii).*
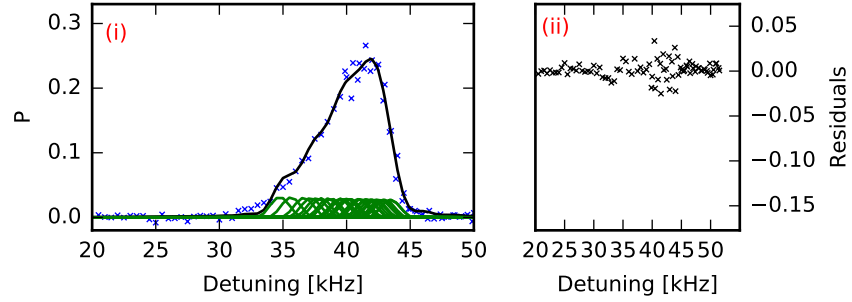


**Figure 5.19:** *After placement the trap frequency of the virtual atoms are randomly moved around in order to optimize the model. This plot is after the optimization stage. The black line in (i) is the combined spectrum from all the virtual atoms, renormalized to match the data.*

are added. The residuals seen in Figure 5.18b(ii) show some improvement over using only two virtual atoms.

The model spectrum after finishing placing the atoms can be seen on Figure 5.18c(i). Now the combined spectrum (the black) models the data much better which is also visible in the plot of the residuals in Figure 5.18c(ii). By looking at the thin green lines in Figure 5.18c(i) we see how the distribution of virtual atoms influence the combined spectrum.

## Optimizing the placement

After the initial placement of atoms we optimize the model by 'wiggling' the trap frequencies ($\nu_T$) of the virtual atoms. This is done by moving the trap frequencies of all virtual atoms, simultaneously, one small frequency step in a random direction.

If the sum of squares show that the steps improved the model, the virtual atoms keep their new trap frequencies and take a new random step from there. This process continues until the sum of squares has converged, at which point the model fits the data better as evident of the plot on Figure 5.19i. We also see a clear improvement in the residuals going from Figure 5.18c(ii) to Figure 5.19ii.

Because our method works by summing over many tiny contributions we have a large number of degrees of freedom. This makes it possible to fit any type of underlying distribution, but also makes the model very susceptible to noise. We minimize the risk of optimizing to noise by limiting the number of virtual atoms, thus ensuring that the contribution from each virtual atom is larger than the average noise.

## Estimating the loss in the blue sideband

As the blue sideband corresponds to an increase in vibrational level $n$, there is some atom loss due to atoms with a high radial energy not being confined for higher axial $n$. We are still able to excite these atoms on the sideband transition because the radial motion of the atom is very slow compared to the axial motion. Therefore the atom is 'bound' while near the center of the trap while becoming 'unbound' once it moves radially away. While the atom is 'bound' it can be excited to a higher axial vibrational level. This is further complicated by the fact that the lattice is tilted 15 degrees to gravity. This causes the trapping potential to be lower on one side compared to the other.

To estimate this loss, we use the same method as we did with the estimated repump loss previously. This time we already have a model fitting the blue sideband, so we can fit the atom number with:

$$N(\nu) = \Delta N \cdot \frac{P_{\text{model}}(\nu)}{\Delta P} + N_{\text{bkg}}. \tag{5.35}$$

where $P_{\text{model}}$ is our model spectrum and $\Delta P = \max(P_{\text{model}})$. A plot of this fit can be seen as the red line on Figure 5.20, where the solid blue line is the model spectrum. We now calculate $R$ exactly as before, and once again average over all the sideband spectra taken under similar conditions. We do not correct the entire spectrum but only the data points which lie inside the blue sideband. Compared to the other loss, this a physical effect that only applies to atoms getting excited to a higher $n$ level. For the data in Figure 5.20 $R$ is found
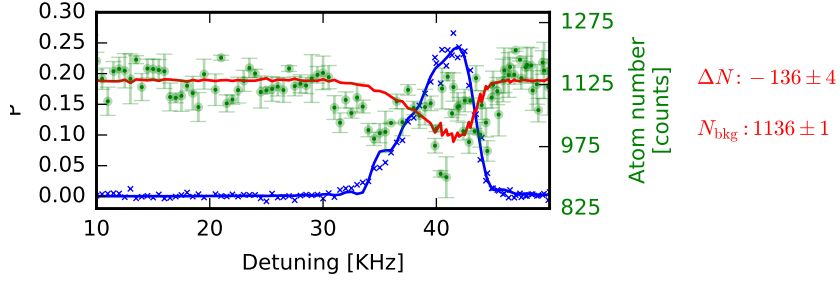
**Figure 5.20:** *The blue sideband model (blue line) on top of the data points (blue cross). The correlation between the sideband model and atom number (green) is fitted with Equation 5.35 and plotted as the red line. It clearly shows that exictation in the blue sideband leads to an atom loss. The numbers are the parameters from the red fit.*

to be 0.69 which corresponds to the drop in atom count seen around the blue sideband in Figure 5.20. Note again that the losses in this data set are not representative for the data used later. This data set is chosen because it clearly illustrates the loss correction processes.

The correction of the loss in the blue sideband relies on the assumption that the loss is identical for all $n \rightarrow n + 1$ excitations, which is not completely true because the energy difference between the higher $n$ states is smaller making it less probable that an atom ends in a semi-bound state.

We also assume that the loss is independent of radial energy even though atoms with higher radial energy are more likely to get lost.

After correcting for loss we discard our previous model for the blue sideband and create a new starting by placing new virtual atoms and optimizing the placement of these.

### Including $n \neq 0$

We now have a model for the blue sideband created under the assumption that all atoms are in $n = 0$. As explained earlier we can get an estimate of $n_{\text{avg}}$ by comparing the ratio of the blue sideband area to the red sideband area. Here we do this by reconstructing the red sideband from our virtual atom distribution. We then renormalize the red sideband model so it fits the data. This can be seen on Figure 5.21 where the red points are the data and the green lines are the reconstructed spectrum from the virtual atoms. The red black line is the rescaled red sideband model.

By taking the ratio of the red sideband model to the blue sideband model we can get an estimate of $n_{\text{avg}}$. Since atoms in $n = 1$ will have slightly different Rabi frequencies than atoms in $n = 0$ we must take this into account for the blue sideband model. We do this by creating a new blue sideband model where we assume that $n_{\text{avg}}$ of the atoms are in $n = 0$ and $1 - n_{\text{avg}}$ atoms are in $n = 1$.

The blue sideband model is then calculated as:

$$P_{\text{total}} = n_{\text{avg}} \cdot P_{\text{model}}(\Delta^{(0)}, \Omega_{\text{SB}}^{(0)}, \tau^{(0)}) + (1 - n_{\text{avg}}) \cdot P_{\text{model}}(\Delta^{(1)}, \Omega_{\text{SB}}^{(1)}, \tau^{(1)})$$

$$(5.36)$$
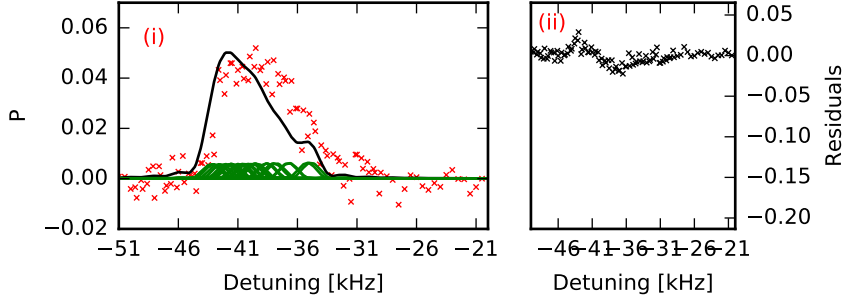
**Figure 5.21:** *(i) shows the reconstructed red sideband used to estimate $n_{\mathrm{avg}}$. The red points are the data points. The green lines are the individual spectra from the virtual atoms and the black line is the combined spectrum from all the virtual atoms. Both the green and the black lines have been normalized to the data. (ii) is the residuals of the model compared to the data.*

where the first term represents atoms in $n = 0$ with the parameters:

$$\Delta^{(0)} = \nu - (\nu_T - \frac{E_{\mathrm{recoil}}}{h})$$

$$n_<^{(0)} = 0 \quad \Delta n^{(0)} = 1 \quad \eta^{(0)} = \sqrt{\frac{E_{\mathrm{recoil}}}{h\nu_T}}$$

$$\tau^{(0)} = 0.001 \text{ s} \tag{5.37}$$

and the second term represents atoms in $n = 1$ with the parameters:

$$\Delta^{(1)} = \nu - (\nu_T - 2\frac{E_{\mathrm{recoil}}}{h})$$

$$n_<^{(1)} = 1 \quad \Delta n^{(1)} = 1 \quad \eta^{(1)} = \sqrt{\frac{E_{\mathrm{recoil}}}{h\nu_T}}$$

$$\tau^{(1)} = 0.001 \text{ s} \tag{5.38}$$

Note that the resonance frequency for the sideband transition $n = 1 \to n = 2$ is shifted an additional factor of $E_{\mathrm{recoil}}$ closer to the carrier due to the anharmonicity.

We then optimize the new blue sideband model by 'wiggling' it around once more and moving the trap frequencies of all the atoms in random steps. Once this has converged we reconstruct the red sideband but assume the $n_{\mathrm{avg}}$ distribution of atoms, and then calculate a new $n_{\mathrm{avg}}$.

This process of estimating $n_{\mathrm{avg}}$ and re optimizing the blue model continues until $n_{\mathrm{avg}}$ has converged on a value.

Finally we end up with the model shown on Figure 5.22. The points are the raw data and the red and blue lines are the sideband model. The black line is the Lorentzian carrier fit.
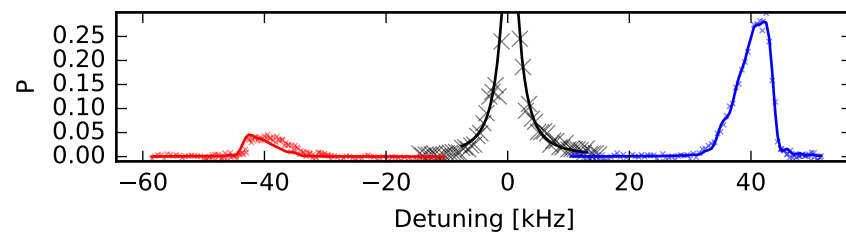
**Figure 5.22:** *The full sideband model after optimizing for n.*

### 5.3.3 Extracting the operational parameters

The full light shift model described in Section 2.3 has five parameters of which four $(n, U_{\text{trap}}^0, \zeta, \delta\zeta)$ can be extracted from our model of the sideband:

$$
\begin{aligned}
\Delta\nu_{\text{clock}}^{\text{lattice}} = {} & (a\,(\nu_{\text{lattice}} - \nu_{\text{E1}}) - b)\,(n_{\text{avg}} + {}^{1\!}/{}_{2}) \sqrt{\left(\zeta_1 - \frac{1}{2}\delta\zeta\right)\frac{U_{\text{trap}}^0}{E_{\text{recoil}}}} \\
& - \left(a\,(\nu_{\text{lattice}} - \nu_{\text{E1}}) - \frac{3}{4}d(2n_{\text{avg}}^2 + 2n_{\text{avg}} + 1)\right)\zeta_1\frac{U_{\text{trap}}^0}{E_{\text{recoil}}} \\
& + d(2n_{\text{avg}} + 1)\left(\left(\zeta_1 + \frac{1}{2}\delta\zeta\right)\frac{U_{\text{trap}}^0}{E_{\text{recoil}}}\right)^{3/2} \\
& - d\left((\zeta_1 + \delta\zeta)\frac{U_{\text{trap}}^0}{E_{\text{recoil}}}\right)^2. \qquad \text{(reprint of Equation 2.71)}
\end{aligned}
$$

The parameters we are able to get from the sideband spectra are averages over all the atoms in the lattice. They will therefore enter Equation 2.71 as averages which becomes a problem if the light shift model is non linear in a given parameter.

Because we do resolved sideband cooling the average vibrational level is very close to zero, making it a reasonable approximation that the light shift model is linear in $n$ and we can therefore use the calculated $n_{\text{avg}}$ as the vibrational level number. This is also true when running the clock in inverted mode where $n_{\text{avg}}$ is close to one, since that still makes the light shift model linear in $n$.

The peak trap depth $U_{\text{trap}}^0$ can be calculated from the largest axial trap frequency in our virtual atom distribution using the relation from Section 2.2:

$$
\omega_T = 2\sqrt{\frac{E_{\text{recoil}}}{\hbar}\frac{U_{\text{trap}}}{\hbar}}, \qquad \text{(Equation 2.23)}
$$

$$
U_{\text{trap}}^0 = \frac{h^2\nu_T^{0^2}}{4E_{\text{recoil}}} \qquad (5.39)
$$

The parameters $\zeta_1$ was included in the light shift model to express the average trap depth as a fraction of the peak trap depth. But since the light shift model is non linear in trap depth we later introduced $\delta\zeta$ to correct the nonlinear averages.

Despite that the sideband spectra were taken with a pulse time too long to freeze the radial motion, we still assume that the distribution of axial trap frequencies represents the distribution of radial energies. $\zeta_1$ is then found from the average of the relative trap depths of our virtual atoms:

$$
\overline{U_{\text{trap}}} = \zeta_1 U_{\text{trap}}^0
$$

$$
\zeta_1 = \frac{1}{N}\sum_j \frac{U_{\text{trap}}^j}{U_{\text{trap}}^0}. \qquad (5.40)
$$

while $\delta\zeta$ is found as described in Section 2.3.1:

$$
\delta\zeta = \zeta_2 - \zeta_1 = \sqrt{\frac{1}{N}\sum_j^N \left(\frac{U_{\text{trap}}^j}{U_{\text{trap}}^0}\right)^2} - \frac{1}{N}\sum_j \frac{U_{\text{trap}}^j}{U_{\text{trap}}^0}, \qquad (5.41)
$$

For the spectrum analyzed here we find the following parameters:

$$n_{\mathrm{avg}} = 0.119 \qquad\qquad U^0_{\mathrm{trap}} = 45.3 \text{ kHz}$$
$$\zeta_1 = 0.88 \qquad\qquad\qquad \delta\zeta = 0.005 \qquad\qquad (5.42)$$

## 5.4 Fitting the light shift model

Throughout the 6 measurement groups described in Section 5.1 we did a total of 37 interleaved measurements. Each interleaved measurement used at least two collections of shots[3] to measure the resulting frequency shift of varying either the lattice intensity or the harmonic vibrational level at various different lattice frequencies. To determine the parameters $U_{\mathrm{trap}}^0$, $n_{\mathrm{avg}}$, $\zeta$ and $\delta\zeta$ we took sideband spectra and extracted the parameters as explained in Section 5.3.

Most of the measurements ran with two additional collections of shots to determine and correct for collisional shifts.

The data for measurement group 3 is summarized in Table 5.3 while the rest of the data can be found at the end of this chapter. The tables contain the time of the interleaved measurement, the lattice frequency and the parameters from the sideband spectra taken before and after the measurement. The parameters are listed in two rows with the top row being the reference point and the bottom row being the measurement point.

The frequency shift between the measurement point and the reference point is then listed together with the uncertainty. The corrected frequency shift refers to the collisional shift corrected frequency shift.

Some of the sideband parameters in Table 5.3 are identical from measurement to measurement because the measurements were done right after each other. The sideband spectrum describing the reference tracker parameters after measurement $n$ is therefore also used to describe the reference parameters before measurement $n+1$. This is only valid if nothing but the lattice frequency is changed, since this has no influence on the sideband spectrum analysis.

As seen from the tables the parameters from the sideband spectra vary slightly from the spectrum before compared to the spectrum after. This is due to uncertainties in estimating the parameters or slow changes in the experimental setup such as misalignments which decrease the lattice intensity. To account for this we use the mean of the values before and after and assign an uncertainty calculated as the uncorrected sample standard deviation. Because we only have two points it can be calculated as:

$$\sigma_k = \sqrt{\frac{(k_{\mathrm{after}} - \langle k \rangle)^2 + (k_{\mathrm{before}} - \langle k \rangle)^2}{2}} \tag{5.43}$$

where $\langle k \rangle$ is the average and $k = U_{\mathrm{trap}}^0, n_{\mathrm{avg}}, \zeta, \delta\zeta$.

**Table 5.3:** *Group 4 Nov 18-20 data.*

| Date | $\nu_{\mathrm{lattice}}$ (+394 798 000) [MHz] | | $U_{\mathrm{trap}}^0$ [$E_{\mathrm{recoil}}$] | $\zeta$ - | $\delta\zeta$ - | $n_{\mathrm{avg}}$ - | Frequency shift [mHz] | Corrected frequency shift [mHz] |
|---|---|---|---|---|---|---|---|---|
| Nov-18 02:55 | +309.0 | Ref | $79.2/84.8$ | $0.81/0.81$ | $0.011/0.011$ | $0.07/0.03$ | $-70.5 \pm 6.5$ | $-62.6 \pm 6.7$ |
| | | Meas | $167.6/166.9$ | $0.87/0.86$ | $0.005/0.006$ | $0.03/0.04$ | | |
| Nov-18 08:55 | +309.0 | Ref | $86.1/72.5$ | $0.82/0.81$ | $0.010/0.011$ | $0.02/0.12$ | $-104.8 \pm 6.2$ | $-97.2 \pm 6.4$ |
| | | Meas | $261.6/199.2$ | $0.79/0.77$ | $0.017/0.017$ | $0.04/0.20$ | | |

---

[3]A reference point and a measurement point as explained in Section 5.2.

| Date | $\nu_{\text{lattice}}$ (+394 798 000) [MHz] | | $U^0_{\text{trap}}$ [$E_{\text{recoil}}$] | $\zeta$ - | $\delta\zeta$ - | $n_{\text{avg}}$ - | Frequency shift [mHz] | Corrected frequency shift [mHz] |
|---|---|---|---|---|---|---|---|---|
| Nov-18 17:01 | +309.0 | Ref | $^{85.9}/_{91.0}$ | $^{0.79}/_{0.80}$ | $^{0.013}/_{0.010}$ | $^{0.15}/_{0.03}$ | $-153.9 \pm 7.1$ | $-139.9 \pm 7.2$ |
|  |  | Meas | $^{331.4}/_{354.2}$ | $^{0.80}/_{0.82}$ | $^{0.012}/_{0.010}$ | $^{0.20}/_{0.07}$ |  |  |
| Nov-18 22:51 | +309.0 | Ref | $^{91.0}/_{88.7}$ | $^{0.80}/_{0.81}$ | $^{0.010}/_{0.012}$ | $^{0.03}/_{0.03}$ | $-198.5 \pm 7.9$ | $-188.0 \pm 8.0$ |
|  |  | Meas | $^{465.6}/_{492.4}$ | $^{0.87}/_{0.83}$ | $^{0.006}/_{0.008}$ | $^{0.03}/_{0.06}$ |  |  |
| Nov-19 03:57 | +309.0 | Ref | $^{88.7}/_{93.4}$ | $^{0.81}/_{0.80}$ | $^{0.012}/_{0.012}$ | $^{0.03}/_{0.01}$ | $-200.9 \pm 6.6$ | $-195.7 \pm 6.8$ |
|  |  | Meas | $^{634.4}/_{640.0}$ | $^{0.88}/_{0.86}$ | $^{0.003}/_{0.006}$ | $^{0.04}/_{0.03}$ |  |  |

The header spanning "Before/After" covers the $\zeta$, $\delta\zeta$, and $n_{\text{avg}}$ columns.

Using this data we can estimate the variables $a$, $b$, $d$ and $\omega_{\text{E1}}$ from the light shift model:

$$\Delta\nu^{\text{lattice}}_{\text{clock}}\left(U^0_{\text{trap}}, n_{\text{avg}}, \zeta, \delta\zeta, \nu_{\text{lattice}}\right) = \left(a\left(\nu_{\text{lattice}} - \nu_{\text{E1}}\right) - b\right)\left(n_{\text{avg}} + 1/2\right)\sqrt{\left(\zeta_1 - \frac{1}{2}\delta\zeta\right)\frac{U^0_{\text{trap}}}{E_{\text{recoil}}}}$$

$$- \left(a\left(\nu_{\text{lattice}} - \nu_{\text{E1}}\right) - \frac{3}{4}d(2n^2_{\text{avg}} + 2n_{\text{avg}} + 1)\right)\zeta_1\frac{U^0_{\text{trap}}}{E_{\text{recoil}}}$$

$$+ d(2n_{\text{avg}} + 1)\left(\left(\zeta_1 + \frac{1}{2}\delta\zeta\right)\frac{U^0_{\text{trap}}}{E_{\text{recoil}}}\right)^{3/2}$$

$$- d\left(\left(\zeta_1 + \delta\zeta\right)\frac{U^0_{\text{trap}}}{E_{\text{recoil}}}\right)^2. \tag{5.44}$$

which predicts a frequency shift from an input of $U^0_{\text{trap}}$, $n_{\text{avg}}$, $\zeta$, $\delta\zeta$ and $\nu_{\text{lattice}}$. Since our measured frequency shifts are the difference between two trackers and thus two sets of input parameters we can calculate the expected shift from as:

$$\Delta\nu = \Delta\nu^{\text{lattice}}_{\text{clock}}\underbrace{\left(U^0_{\text{trap}}, n_{\text{avg}}, \zeta, \delta\zeta, \nu_{\text{lattice}}\right)}_{\text{Meas}} - \Delta\nu^{\text{lattice}}_{\text{clock}}\underbrace{\left(U^0_{\text{trap}}, n_{\text{avg}}, \zeta, \delta\zeta, \nu_{\text{lattice}}\right)}_{\text{Ref}}$$

$$\tag{5.45}$$

where the 'Meas' and 'Ref' refer to the parameters in the top and bottom row of each input in Table 5.3. The lattice frequency was never varied between the reference and measurement tracker and is thus identical for both.

By using the data from the 37 interleaved measurements we can estimate the variables of the light shift model by finding the set of variables that minimize the $\chi^2$:

$$\chi^2 = \sum_i^{37}\frac{\left(f^{\text{diff}}_i - \Delta\nu_i\right)^2}{\sigma^2_{f^{\text{diff}}_i}}, \tag{5.46}$$

where $i$ denotes the $i$'th data point.

Doing this with the 37 data points and the parameters from the sideband spectra, without taking the uncertainties of the parameters into account, yields the results listed in Table 5.4. The table lists the results from using either the uncorrected frequency measurements, or the measurements which have been

corrected for collisional shifts. There is a reduction in the calculated $\chi^2$ when including the collisional shifts, but because we only have 37 data points care must be taken when interpreting the $\chi^2$

| **First fitting** | With collisional shifts | | Without collisional shifts | |
|---|---|---|---|---|
| Variable | Value | Uncertainty | Value | Uncertainty |
| $a \left( \frac{\mu Hz}{MHz} \right)$ | 25.34 | 0.25 | 25.80 | 0.24 |
| $b$ (mHz) | -1.36 | 0.36 | -1.29 | 0.32 |
| $d$ (µHz) | -1.184 | 0.059 | -1.306 | 0.055 |
| $\nu_{E1}$ (MHz) | 394 798 263.1 | 1.2 | 394 798 260.5 | 1.1 |
| $\chi^2$ | 40.3 | | 50.4 | |

**Table 5.4:** *Results from fitting the light shift model to the 37 data points with and without the collisional shift correction. The uncertainties in the parameters $U_{trap}^0$, $n_{avg}$, $\zeta$, $\delta\zeta$, $\nu_{lattice}$ are not included in this fit. With 37 data points and 4 fitted parameters we expect a reduced chisquare 33.*

The data points for the measurements in group 1 and 2, which focused on varying $n$ over a range of lattice frequencies at two different trap depths, are plotted on Figure 5.23. The mean peak trap depth of the blue points is 89.2 $E_{recoil}$ while for the red points it is 127.1 $E_{recoil}$. The black points include the collisional shift correction when available. If no collisional shift corrections exists the black point is identical to the colored point.

The slope we see in this figure is expected because we only varied $n$ and kept the trap depth constant. Looking at Equation 5.44 and Equation 5.44 we see that if the trap depth is kept constant only the first term including $\nu_{lattice}$ survives. This means the observed shift from varying $n$ will have a slope in lattice frequency proportional to $a$. The slope is also proportional to $\sqrt{U_{trap}^0}$ which explains why the red points follow a steeper slope than blue points.

The plot only shows the data points as a function of a single parameter, in this case the lattice frequency. In reality the points vary slightly in peak trap depth ($U_{trap}^0$) and energy level ($n_{avg}$) from each other. The fitting model takes this into account but it makes it difficult to draw a single line which goes through all the points. The blue line uses the mean of the parameters as input to the light shift model fit and plots it as a function of lattice frequency. Similarly the red line uses the mean parameters from the red points. It is therefore not expected that it agrees perfectly with the points.

Figure 5.24 shows the data points for the measurements in group 3-6 that varied the trap depth at 7 different lattice frequencies. The colored points are the frequency shifts without the collisional shift correction and the black points include this correction. The lines are once again drawn by taking the mean of the input parameters of all the points taken at a particular lattice frequency and then plotting the light shift model as a function of peak trap depth.

Because these measurements vary the trap depth over a very large range we see a quadratic behavior in trap depth as expected from Equation 5.44, which makes the determination of $d$ possible. By measuring the shift at similar trap depths but with different lattice frequencies we can accurately determine $\nu_{E1}$. We see this from the second term in Equation 5.44 which contributes a

shift that is linear in trap depth with a slope which depends strongly on the detuning from the magic frequency. Because the points in the seven data series are taken at the same trap depths, the changing linear slope must be due to the detuning from the magic wavelength.

Note that the accessible trap depth range with the previous lattice setup was from $70\,E_{\text{recoil}}$ to $160\,E_{\text{recoil}}$.

### 5.4.1  Including the statistical parameter uncertainties

The first fit we made to estimate the variables of the light shift model did not take the error of the input parameters into account. With our first fit we now have a model where we can take these uncertainties into account by assuming that they are small enough to justify a linear approximation where we can use the derivative to convert a parameter uncertainty into a frequency shift error:

$$\sigma_{f_k} = \frac{\partial \text{LSM}}{\partial k} \cdot \sigma_k \tag{5.47}$$

where $k = U^0_{\text{trap}}, n_{\text{avg}}, \zeta, \delta\zeta, \nu_{\text{lattice}}$ and $\sigma_k$ is the uncorrected sample standard deviation calculated over just two points as mentioned earlier except for $\nu_{\text{lattice}}$. The uncertainty on the lattice frequency is determined to be 100 kHz based on observed beat signal between the lattice laser and the frequency comb line it is locked to.

After propagating the parameter errors to a frequency uncertainty we add it in quadrature to the existing frequency shift uncertainty.

The results from fitting the light shift model again, this time including the statistical uncertainties of the parameters, can be seen in Table 5.5. The $\chi^2$ has now decreased significantly and the reduced $\chi^2$ with 33 degrees of freedom is now 1.00. This indicates that we have reasonably estimated the statistical uncertainties of our measurements. Caution must be taken however, since we only have 33 degrees of freedom the $\chi^2$ P value is 0.46. The P value is expected to be 0.5 for a reduced $\chi^2$ of one, but the deviation in our case may be due to the low number of degrees of freedom.

| **Second fitting** | With parameter uncertainties | |
|---|---|---|
| Variable | Value | Uncertainty |
| $a\left(\frac{\mu\text{Hz}}{\text{MHz}}\right)$ | 25.28 | 0.29 |
| $b$ (mHz) | -1.35 | 0.37 |
| $d$ (µHz) | -1.164 | 0.071 |
| $\nu_{\text{E1}}$ (MHz) | 394 798 263.5 | 1.4 |
| $\chi^2$ | 33.1 | |

**Table 5.5:** *Results from fitting the light shift model to the 37 data points including the uncertainties in the parameters $U^0_{\text{trap}}$, $n_{\text{avg}}$, $\zeta$, $\delta\zeta$, $\nu_{\text{lattice}}$.*

A plot of the data points with the increased uncertainty can be seen on Figure 5.25 and Figure 5.26 where the colored points are the data points with only the measured frequency shift error and the black points include both collisional shifts and statistical parameter uncertainties. The lines are drawn in the same way as for Figure 5.23 and Figure 5.24. Since we have only included

**Figure 5.23:** *Data from the frequency shift measurements in group 1 and 2 after the first fitting. The points show the shift arising from varying the vibrational level between zero and one, at two different trap depths. The lines are the light shift model fit plotted as a function of lattice frequency with the other input parameters being the mean of the parameters of the corresponding points (blue or red). The colored points are the raw frequency measurements and the black points include the correction due to collisional shifts.*





**Figure 5.24:** *Data from the measurements in group 3-6 after the first fitting. The 7 different series measure the shift between different trap depths at different lattice frequencies. The lines are the light shift model fit plotted as a function of trap depth for each of the 7 series. The other input parameters are the mean of the parameters of the points taken at the same lattice frequency. The colored points are the raw frequency measurements and the black points include the correction due to collisional shifts.*

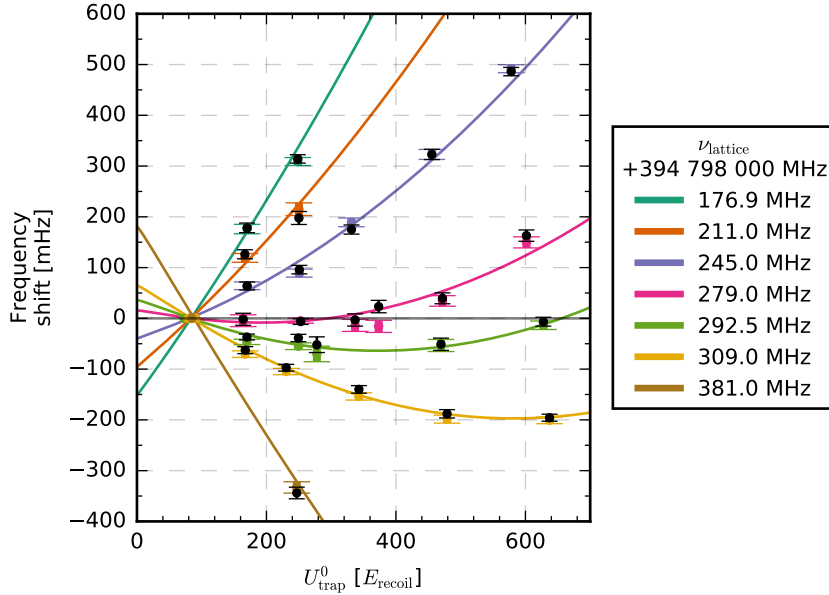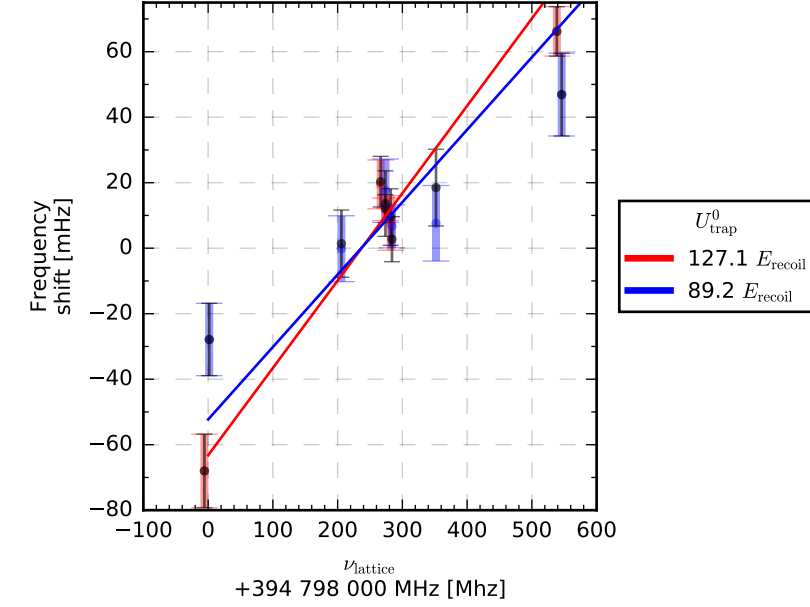extra uncertainties only the error bars of the black points have increased while their position has not changed.

## 5.5   The comparison with the previous values

The variables  we have now determined for the light shift model only include statistical uncertainties as we have not treated any systematic effects which could affect the results. Nonetheless, we compare our values with the previous values used in [14] in Table 5.6.

   We see that our new values all agree with the old vales within the uncertainty of the old values, and the precision of all variables but $b$ have improved by an order of magnitude. This is not a completely fair comparison since our new values do not include systematic uncertainties while the previous values do.

| Variable | New values | Values from [14] |
|---|---|---|
| $a \left( \frac{\mu\text{Hz}}{\text{MHz}} \right)$ | 25.28  ±0.29 | 21   ±6 |
| $b$ (mHz) | -1.35  ±0.37 | -0.68±0.71 |
| $d$ (μHz) | -1.164±0.071 | -1.9  ±0.8 |
| $\nu_{\text{E1}}$ (MHz) | 394 798 263.5   ±1.4 | 394 798 265   ±9 |

**Table 5.6:** *Comparison of the new estimated variables of the light shift model compared to those used in [14] and presented in Section 3.*

   We can also compare the contribution of our new variables under normal operating conditions, i.e. the conditions used in [14]:

$$U^0_{\text{trap}} = 100(2) \, E_{\text{recoil}} \qquad\qquad \zeta = 0.72(5)$$
$$n_{\text{avg}} = 0.08(8) \qquad\qquad \nu_{\text{lattice}} = 394 \; 798 \; 278(0.1) \text{ MHz}$$

By using error propagation like we did in Section 3 we can estimate the contribution from each of the variables. A comparison of the contributions from the new values and the previous values can be seen in Table 5.7.

   The large reduction in the contribution of the E1 magic wavelength is because the uncertainty is much lower. This is primarily due to the uncertainty of $d$ and $a$ also being lower. As explained earlier, the magic wavelength can be estimated by measuring the shift at similar trap depths over a range of different lattice frequencies. The uncertainty of $\nu_{\text{E1}}$ will then be correlated with the uncertainties of $a$ and $d$.

   With the new values the uncertainty contribution from $n_{\text{avg}}$ has increased. The contribution to the uncertainty from $n_{\text{avg}}$ is proportional to the partial derivative of the light shift model:

$$\frac{\partial \Delta\nu^{\text{laattice}}_{\text{clock}}}{\partial n_{\text{avg}}} = (a \left( \nu_{\text{lattice}} - \nu_{\text{E1}} \right) - b) \sqrt{\zeta \frac{U^0_{\text{trap}}}{E_{\text{recoil}}}} + \frac{3}{4} d (4 n_{\text{avg}} + 2) \zeta \frac{U^0_{\text{trap}}}{E_{\text{recoil}}} + 2d \left( \zeta \frac{U^0_{\text{trap}}}{E_{\text{recoil}}} \right)^{3/2}.$$
$$(5.48)$$

Because $a$ and $d$ have both become larger ($d$ has become less negative) and $b$ and $\nu_{\text{E1}}$ have become smaller, the contribution from $n_{\text{avg}}$ is expected to increase. The same argument can be made for the increased uncertainty of

**Figure 5.25:** *Data from the frequency shift measurements in group 1 and 2 after the second fitting. The black points now include the correction due to collisional shifts and the added uncertainty from the input parameters. The points show the shift arising from varying the vibrational level between zero and one, at two different trap depths. The lines are the light shift model fit plotted as a function of lattice frequency with the other input parameters being the mean of the parameters of the corresponding points (blue or red). The colored points are the raw frequency measurements and the black points include the correction due to collisional shifts and the added uncertainty from the input parameters.*
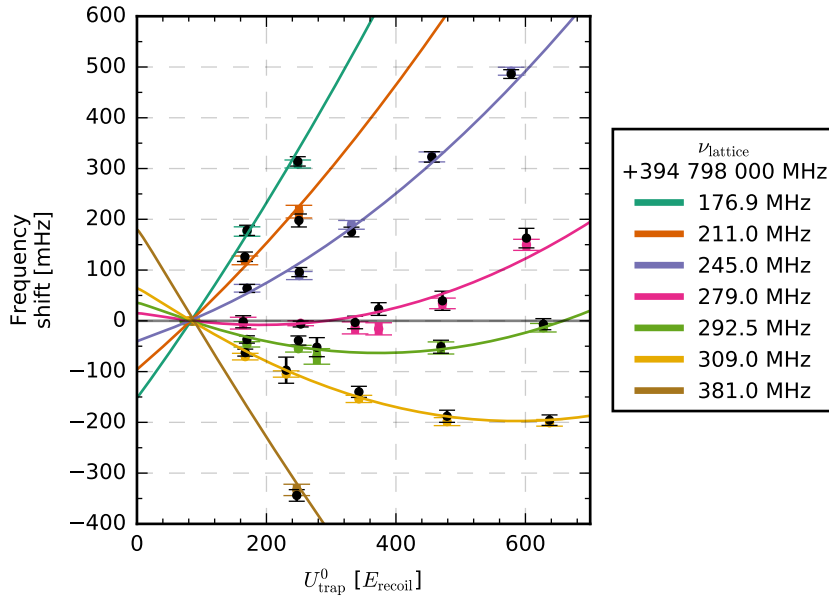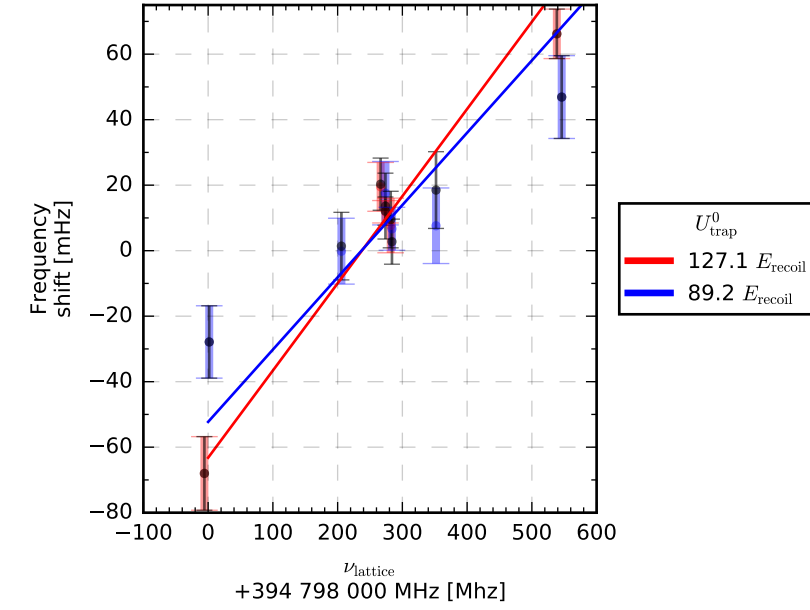




**Figure 5.26:** *Data from the measurements in group 3-6 after the second fitting. The black points now include both the collisional shift correction and the uncertainties from the input parameters. The 7 different series measure the shift between different trap depths at different lattice frequencies. The lines are the light shift model fit plotted as a function of trap depth for each of the 7 series. The other input parameters are the mean of the parameters of the points taken at the same lattice frequency. The colored points are the raw frequency measurements and the black points include the correction due to collisional shifts.*

$U_{\text{trap}}^0$. The latter will however decrease when we use the newfound value of the magic frequency to determine a new operation point.

| Coefficient | New | From [14] |
|---|---|---|
| $a$ | 0.54 | 10.09 |
| $b$ | 3.51 | 6.74 |
| $d$ | 0.60 | 6.81 |
| $\zeta$ | 1.98 | 2.64 |
| $n_{\text{avg}}$ | 2.01 | 0.85 |
| $\nu_{\text{E1}}$ | 4.87 | 26.01 |
| $\nu_{\text{lattice}}$ | 4.17 | 3.47 |
| $U_{\text{trap}}^0$ | 1.67 | 0.43 |

**Table 5.7:** *Contribution to the fractional uncertainty from the lattice light shift model with our new and with the old variables, given the experimental parameters used in [14].*

## 5.6 Data tables

The data used to estimate the variables of the light shift model is presented here. Each table represents one group of measurements.

**Table 5.8:** *Group 1 Aug 15-16 data.*

| Date | $\nu_{\text{lattice}}$ (+394 798 000) [MHz] | | $U_{\text{trap}}^0$ [$E_{\text{recoil}}$] | $\zeta$ - | $\delta\zeta$ - | $n_{\text{avg}}$ - | Frequency shift [mHz] | Corrected frequency shift [mHz] |
|---|---|---|---|---|---|---|---|---|
| Aug-15 21:40 | +274.0 | Ref | $^{89.4}/_{91.1}$ | $^{0.78}/_{0.79}$ | $^{0.012}/_{0.012}$ | $^{0.01}/_{0.01}$ | $17.5 \pm 9.7$ | $13.6 \pm 9.8$ |
| | | Meas | $^{85.9}/_{97.9}$ | $^{0.77}/_{0.69}$ | $^{0.011}/_{0.013}$ | $^{0.68}/_{0.67}$ | | |
| Aug-16 02:45 | +284.0 | Ref | $^{92.1}/_{92.1}$ | $^{0.78}/_{0.78}$ | $^{0.013}/_{0.013}$ | $^{0.02}/_{0.02}$ | $6.7 \pm 6.6$ | $2.8 \pm 6.7$ |
| | | Meas | $^{89.4}/_{89.4}$ | $^{0.78}/_{0.78}$ | $^{0.011}/_{0.011}$ | $^{0.73}/_{0.73}$ | | |
| Aug-16 05:32 | +352.0 | Ref | $^{92.1}/_{92.1}$ | $^{0.78}/_{0.78}$ | $^{0.013}/_{0.013}$ | $^{0.02}/_{0.02}$ | $7.6 \pm 11.5$ | $18.5 \pm 11.6$ |
| | | Meas | $^{89.4}/_{89.4}$ | $^{0.78}/_{0.78}$ | $^{0.011}/_{0.011}$ | $^{0.73}/_{0.73}$ | | |
| Aug-16 08:17 | +206.0 | Ref | $^{92.1}/_{92.2}$ | $^{0.78}/_{0.79}$ | $^{0.013}/_{0.013}$ | $^{0.02}/_{0.02}$ | $-0.2 \pm 10.1$ | $1.4 \pm 10.1$ |
| | | Meas | $^{89.4}/_{88.0}$ | $^{0.78}/_{0.78}$ | $^{0.011}/_{0.012}$ | $^{0.73}/_{0.62}$ | | |
| Aug-16 11:28 | +2.0 | Ref | $^{92.2}/_{92.2}$ | $^{0.79}/_{0.79}$ | $^{0.013}/_{0.013}$ | $^{0.02}/_{0.02}$ | $-27.9 \pm 11.0$ | - |
| | | Meas | $^{88.0}/_{88.0}$ | $^{0.78}/_{0.78}$ | $^{0.012}/_{0.012}$ | $^{0.62}/_{0.62}$ | | |
| Aug-16 12:26 | +546.0 | Ref | $^{92.2}/_{92.2}$ | $^{0.79}/_{0.79}$ | $^{0.013}/_{0.013}$ | $^{0.02}/_{0.02}$ | $46.9 \pm 12.6$ | - |
| | | Meas | $^{88.0}/_{88.0}$ | $^{0.78}/_{0.78}$ | $^{0.012}/_{0.012}$ | $^{0.62}/_{0.62}$ | | |

**Table 5.9:** *Group 2 Aug 27-29 data.*

| Date | $\nu_{\text{lattice}}$ (+394 798 000) [MHz] | | $U^0_{\text{trap}}$ [$E_{\text{recoil}}$] | $\zeta$ - | $\delta\zeta$ - | $n_{\text{avg}}$ - | Frequency shift [mHz] | Corrected frequency shift [mHz] |
|---|---|---|---|---|---|---|---|---|
| Aug-27 01:54 | +274.0 | Ref | $^{121.0}/_{121.7}$ | $^{0.77}/_{0.77}$ | $^{0.015}/_{0.016}$ | $^{0.05}/_{0.06}$ | $11.9 \pm 3.4$ | $12.1 \pm 3.8$ |
| | | Meas | $^{117.8}/_{117.3}$ | $^{0.77}/_{0.77}$ | $^{0.015}/_{0.014}$ | $^{0.74}/_{0.83}$ | | |
| Aug-27 17:48 | +266.0 | Ref | $^{132.1}/_{123.2}$ | $^{0.72}/_{0.76}$ | $^{0.016}/_{0.017}$ | $^{0.09}/_{0.06}$ | $19.5 \pm 7.5$ | $20.3 \pm 7.6$ |
| | | Meas | $^{117.3}/_{134.0}$ | $^{0.77}/_{0.67}$ | $^{0.014}/_{0.017}$ | $^{0.83}/_{0.76}$ | | |
| Aug-28 12:47 | +539.0 | Ref | $^{123.2}/_{123.2}$ | $^{0.76}/_{0.76}$ | $^{0.017}/_{0.017}$ | $^{0.06}/_{0.06}$ | $66.2 \pm 7.6$ | - |
| | | Meas | $^{134.0}/_{134.0}$ | $^{0.67}/_{0.67}$ | $^{0.017}/_{0.017}$ | $^{0.76}/_{0.76}$ | | |
| Aug-28 18:05 | -6.0 | Ref | $^{123.2}/_{131.1}$ | $^{0.76}/_{0.71}$ | $^{0.017}/_{0.026}$ | $^{0.06}/_{0.12}$ | $-68.0 \pm 11.2$ | - |
| | | Meas | $^{134.0}/_{134.0}$ | $^{0.67}/_{0.67}$ | $^{0.017}/_{0.017}$ | $^{0.76}/_{0.76}$ | | |
| Aug-29 01:10 | +282.0 | Ref | $^{127.6}/_{127.6}$ | $^{0.76}/_{0.76}$ | $^{0.018}/_{0.018}$ | $^{0.05}/_{0.05}$ | $7.7 \pm 8.3$ | $9.5 \pm 8.5$ |
| | | Meas | $^{124.3}/_{124.3}$ | $^{0.73}/_{0.73}$ | $^{0.017}/_{0.017}$ | $^{0.79}/_{0.79}$ | | |

**Table 5.10:** *Group 3 Nov 9-11 data.*

| Date | $\nu_{\text{lattice}}$ (+394 798 000) [MHz] | | $U^0_{\text{trap}}$ [$E_{\text{recoil}}$] | $\zeta$ - | $\delta\zeta$ - | $n_{\text{avg}}$ - | Frequency shift [mHz] | Corrected frequency shift [mHz] |
|---|---|---|---|---|---|---|---|---|
| Nov-09 01:16 | +293.0 | Ref | $^{86.1}/_{88.5}$ | $^{0.81}/_{0.80}$ | $^{0.011}/_{0.012}$ | $^{0.03}/_{0.05}$ | $-13.6 \pm 8.4$ | $-6.6 \pm 8.6$ |
| | | Meas | $^{617.7}/_{637.6}$ | $^{0.86}/_{0.84}$ | $^{0.007}/_{0.007}$ | $^{0.06}/_{0.09}$ | | |
| Nov-09 06:39 | +293.0 | Ref | $^{88.5}/_{84.7}$ | $^{0.80}/_{0.82}$ | $^{0.012}/_{0.009}$ | $^{0.05}/_{0.03}$ | $-53.4 \pm 11.9$ | $-51.0 \pm 12.0$ |
| | | Meas | $^{489.3}/_{449.8}$ | $^{0.84}/_{0.83}$ | $^{0.008}/_{0.009}$ | $^{0.07}/_{0.07}$ | | |
| Nov-09 18:38 | +293.0 | Ref | $^{83.6}/_{61.5}$ | $^{0.80}/_{0.80}$ | $^{0.010}/_{0.017}$ | $^{0.05}/_{0.18}$ | $-70.1 \pm 15.3$ | $-51.9 \pm 15.4$ |
| | | Meas | $^{312.3}/_{243.4}$ | $^{0.79}/_{0.80}$ | $^{0.013}/_{0.011}$ | $^{0.16}/_{0.20}$ | | |
| Nov-10 04:52 | +293.0 | Ref | $^{87.4}/_{83.2}$ | $^{0.81}/_{0.80}$ | $^{0.010}/_{0.011}$ | $^{0.09}/_{0.22}$ | $-54.9 \pm 6.6$ | $-38.8 \pm 7.0$ |
| | | Meas | $^{262.3}/_{236.5}$ | $^{0.80}/_{0.77}$ | $^{0.013}/_{0.016}$ | $^{0.18}/_{0.33}$ | | |
| Nov-10 23:37 | +293.0 | Ref | $^{82.6}/_{90.7}$ | $^{0.79}/_{0.80}$ | $^{0.012}/_{0.012}$ | $^{0.01}/_{0.10}$ | $-46.3 \pm 5.2$ | $-36.7 \pm 5.5$ |
| | | Meas | $^{159.6}/_{180.0}$ | $^{0.87}/_{0.86}$ | $^{0.005}/_{0.006}$ | $^{0.03}/_{0.09}$ | | |

**Table 5.11:** *Group 4 Nov 18-20 data.*

| Date | $\nu_{\text{lattice}}$ (+394 798 000) [MHz] | | $U^0_{\text{trap}}$ [$E_{\text{recoil}}$] | Before/After | | | Frequency shift [mHz] | Corrected frequency shift [mHz] |
| | | | | $\zeta$ - | $\delta\zeta$ - | $n_{\text{avg}}$ - | | |
| Nov-18 02:55 | +309.0 | Ref | $79.2/_{84.8}$ | $0.81/_{0.81}$ | $0.011/_{0.011}$ | $0.07/_{0.03}$ | $-70.5 \pm 6.5$ | $-62.6 \pm 6.7$ |
| | | Meas | $167.6/_{166.9}$ | $0.87/_{0.86}$ | $0.005/_{0.006}$ | $0.03/_{0.04}$ | | |
| Nov-18 08:55 | +309.0 | Ref | $86.1/_{72.5}$ | $0.82/_{0.81}$ | $0.010/_{0.011}$ | $0.02/_{0.12}$ | $-104.8 \pm 6.2$ | $-97.2 \pm 6.4$ |
| | | Meas | $261.6/_{199.2}$ | $0.79/_{0.77}$ | $0.017/_{0.017}$ | $0.04/_{0.20}$ | | |
| Nov-18 17:01 | +309.0 | Ref | $85.9/_{91.0}$ | $0.79/_{0.80}$ | $0.013/_{0.010}$ | $0.15/_{0.03}$ | $-153.9 \pm 7.1$ | $-139.9 \pm 7.2$ |
| | | Meas | $331.4/_{354.2}$ | $0.80/_{0.82}$ | $0.012/_{0.010}$ | $0.20/_{0.07}$ | | |
| Nov-18 22:51 | +309.0 | Ref | $91.0/_{88.7}$ | $0.80/_{0.81}$ | $0.010/_{0.012}$ | $0.03/_{0.03}$ | $-198.5 \pm 7.9$ | $-188.0 \pm 8.0$ |
| | | Meas | $465.6/_{492.4}$ | $0.87/_{0.83}$ | $0.006/_{0.008}$ | $0.03/_{0.06}$ | | |
| Nov-19 03:57 | +309.0 | Ref | $88.7/_{93.4}$ | $0.81/_{0.80}$ | $0.012/_{0.012}$ | $0.03/_{0.01}$ | $-200.9 \pm 6.6$ | $-195.7 \pm 6.8$ |
| | | Meas | $634.4/_{640.0}$ | $0.88/_{0.86}$ | $0.003/_{0.006}$ | $0.04/_{0.03}$ | | |

**Table 5.12:** *Group 5 Nov 21-23 data.*

| Date | $\nu_{\text{lattice}}$ (+394 798 000) [MHz] | | $U^0_{\text{trap}}$ [$E_{\text{recoil}}$] | Before/After | | | Frequency shift [mHz] | Corrected frequency shift [mHz] |
| | | | | $\zeta$ - | $\delta\zeta$ - | $n_{\text{avg}}$ - | | |
| Nov-21 19:25 | +279.0 | Ref | $77.8/_{83.9}$ | $0.81/_{0.81}$ | $0.013/_{0.011}$ | $0.06/_{0.02}$ | $-4.6 \pm 11.6$ | $-1.8 \pm 11.8$ |
| | | Meas | $160.3/_{167.8}$ | $0.85/_{0.87}$ | $0.006/_{0.005}$ | $0.09/_{0.02}$ | | |
| Nov-22 00:25 | +279.0 | Ref | $83.9/_{86.5}$ | $0.81/_{0.80}$ | $0.011/_{0.010}$ | $0.02/_{0.02}$ | $-4.7 \pm 4.9$ | $-6.4 \pm 5.3$ |
| | | Meas | $253.2/_{252.6}$ | $0.78/_{0.80}$ | $0.017/_{0.014}$ | $0.07/_{0.06}$ | | |
| Nov-22 07:31 | +279.0 | Ref | $86.5/_{86.5}$ | $0.80/_{0.80}$ | $0.010/_{0.010}$ | $0.02/_{0.02}$ | $-13.9 \pm 11.9$ | $-3.2 \pm 12.0$ |
| | | Meas | $344.3/_{329.6}$ | $0.80/_{0.82}$ | $0.014/_{0.011}$ | $0.05/_{0.07}$ | | |
| Nov-22 12:45 | +279.0 | Ref | $86.5/_{83.3}$ | $0.80/_{0.81}$ | $0.010/_{0.010}$ | $0.02/_{0.12}$ | $-15.8 \pm 12.0$ | $23.2 \pm 12.1$ |
| | | Meas | $375.4/_{371.2}$ | $0.82/_{0.81}$ | $0.012/_{0.012}$ | $0.09/_{0.16}$ | | |
| Nov-22 17:11 | +279.0 | Ref | $83.3/_{89.9}$ | $0.81/_{0.80}$ | $0.010/_{0.012}$ | $0.12/_{0.01}$ | $34.3 \pm 10.5$ | $39.5 \pm 10.6$ |
| | | Meas | $443.3/_{500.3}$ | $0.82/_{0.87}$ | $0.009/_{0.005}$ | $0.19/_{0.02}$ | | |
| Nov-23 02:28 | +279.0 | Ref | $89.9/_{83.6}$ | $0.80/_{0.82}$ | $0.012/_{0.010}$ | $0.01/_{0.01}$ | $149.7 \pm 10.9$ | $163.0 \pm 11.1$ |
| | | Meas | $624.5/_{578.6}$ | $0.86/_{0.87}$ | $0.006/_{0.006}$ | $0.03/_{0.03}$ | | |

**Table 5.13:** *Group 6 Nov 24-26 data.*

| Date | $\nu_{\text{lattice}}$ (+394 798 000) [MHz] | | $U_{\text{trap}}^0$ [$E_{\text{recoil}}$] | $\zeta$ - | $\delta\zeta$ - | $n_{\text{avg}}$ - | Frequency shift [mHz] | Corrected frequency shift [mHz] |
|---|---|---|---|---|---|---|---|---|
| Nov-24 19:12 | +177.0 | Ref | 85.5/86.1 | 0.80/0.79 | 0.011/0.011 | 0.03/0.02 | $175.9 \pm 9.3$ | $178.2 \pm 9.4$ |
| | | Meas | 168.7/171.4 | 0.86/0.87 | 0.005/0.005 | 0.01/0.00 | | |
| Nov-24 23:55 | +245.0 | Ref | 86.1/86.5 | 0.79/0.82 | 0.011/0.010 | 0.02/0.01 | $64.2 \pm 7.6$ | $63.8 \pm 7.7$ |
| | | Meas | 171.4/168.8 | 0.87/0.87 | 0.005/0.005 | 0.00/0.01 | | |
| Nov-25 05:17 | +245.0 | Ref | 85.1/83.1 | 0.81/0.80 | 0.009/0.012 | 0.00/0.01 | $89.2 \pm 8.0$ | $96.0 \pm 8.2$ |
| | | Meas | 254.4/247.0 | 0.78/0.80 | 0.016/0.015 | 0.03/0.02 | | |
| Nov-25 12:08 | +211.0 | Ref | 84.8/88.0 | 0.80/0.80 | 0.011/0.010 | 0.01/0.03 | $215.1 \pm 12.5$ | $197.7 \pm 12.6$ |
| | | Meas | 250.0/250.2 | 0.79/0.79 | 0.017/0.014 | 0.06/0.05 | | |
| Nov-25 18:23 | +211.0 | Ref | 83.2/82.4 | 0.81/0.82 | 0.010/0.011 | 0.01/0.03 | $119.1 \pm 8.6$ | $126.2 \pm 8.8$ |
| | | Meas | 168.4/165.1 | 0.85/0.87 | 0.005/0.005 | 0.02/0.01 | | |
| Nov-25 23:22 | +245.0 | Ref | 82.4/84.7 | 0.82/0.81 | 0.011/0.009 | 0.03/0.06 | $491.7 \pm 7.9$ | $486.1 \pm 8.1$ |
| | | Meas | 578.2/577.8 | 0.87/0.87 | 0.005/0.007 | 0.06/0.04 | | |
| Nov-26 03:38 | +245.0 | Ref | 84.8/82.0 | 0.80/0.80 | 0.010/0.012 | 0.04/0.12 | $322.9 \pm 9.8$ | $322.9 \pm 10.0$ |
| | | Meas | 456.9/454.1 | 0.86/0.86 | 0.007/0.006 | 0.03/0.06 | | |
| Nov-26 08:55 | +245.0 | Ref | 83.3/85.8 | 0.81/0.81 | 0.011/0.010 | 0.04/0.06 | $189.1 \pm 8.6$ | $175.0 \pm 8.8$ |
| | | Meas | 328.7/333.9 | 0.79/0.81 | 0.013/0.011 | 0.13/0.14 | | |
| Nov-26 13:17 | +177.0 | Ref | 85.8/84.7 | 0.81/0.81 | 0.010/0.012 | 0.06/0.05 | $308.9 \pm 7.9$ | $314.1 \pm 8.1$ |
| | | Meas | 250.0/246.8 | 0.78/0.79 | 0.017/0.015 | 0.14/0.14 | | |
| Nov-26 16:58 | +381.0 | Ref | 84.7/84.7 | 0.81/0.81 | 0.012/0.012 | 0.05/0.05 | $-333.1 \pm 11.2$ | $-344.0 \pm 11.3$ |
| | | Meas | 246.8/246.8 | 0.79/0.79 | 0.015/0.015 | 0.14/0.14 | | |

# 6

# Summary and outlook

## 6.1  Summary and outlook

With the implementation of the new lattice setup we have been able to create a lattice with a much higher intensity than previously, allowing us to measure trap depths ranging from 60 $E_{\mathrm{recoil}}$ to 640 $E_{\mathrm{recoil}}$. By measuring the frequency difference between very high and very low trap depths we have been able to clearly resolve the quadratic behavior of the hyperpolarizability. This has led to a determination of the hyperpolarizability coefficient $d$ which is much more precise than the value previously used. It is also the first the hyperpolarizability coefficient is directly measured with our clock setup, having previously borrowed the coefficient from the Yb clock at NIST.

Simultaneously we have been able to determine the magic frequency $\nu_{\mathrm{E1}}$, the multipolarizabiltiy coefficient $b$, and the polarizability coefficient $a$ with improved precision.

The new coefficients presented in this work only include statistical uncertainties and do not take systematic uncertainties into account. It is unlikely that the inclusion of systematic uncertainties will change the uncertainties on the parameter by an order of magnitude, but great care should be taken when comparing the new coefficients with those used in previous works.

When looking at the fractional contribution at normal operating conditions these results suggest that the contributions from $a$ and $d$ are in the high $10^{-19}$ range while the contributions from $b$ and $\nu_{\mathrm{E1}}$ are an order of magnitude larger.

## 6.2  Outlook

Before we can truly claim anything on the basis of the coefficients presented here it is paramount that the systematic uncertainties are included. One of the  contributions is the systematic effect of running waves in the lattice beam. These are caused by any power imbalance between the two counter propagating beams as this will affect the intensity at the nodes. It will no longer be zero and there will be a systematic contribution from the electronic quadrupole and

magnetic dipole polarizabilities. The determination of the light shift model co-

efficients is nonetheless an important step in improving the fractional stability
of the Yb optical lattice clock. With the new coefficients it should be possible
to go below $10^{-17}$.

One of the limitations of the current clock setup is the radial motion of
the atoms. The implementation of the $\zeta$ and $\delta\zeta$ parameters in the light shift
model are ways of dealing with not having enough control of the radial motion.
The uncertainties they introduce could be decreased if the atoms could be
radially cooled. The settling pulses described in this work are a step in the
right direction, but further cooling of the radial motion of the atoms would
lead to improved results.

Another possibility is to design the next generation of the Yb lattice clock as
a 3D lattice clock. This would confine the atoms tightly in all three dimensions
and allow much greater control of the atomic motion.

# A two level system

Considering a laser producing an electrical field given as:

$$E = E_0 \cos\left(\mathbf{k} \cdot \mathbf{R} - \omega t\right) \hat{\epsilon} = \frac{E_0}{2} \hat{\epsilon} \left( e^{i(\mathbf{k} \cdot \mathbf{R} - \omega t)} + e^{-i(\mathbf{k} \cdot \mathbf{R} - \omega t)} \right) \qquad (A.1)$$

The interaction with an atom is described by the interaction Hamiltonian:

$$\mathcal{H}_{\mathrm{AF}} = -\mathbf{d} \cdot \frac{E_0}{2} \hat{\epsilon} \left( e^{i(\mathbf{k} \cdot \mathbf{R} - \omega t)} + e^{-i(\mathbf{k} \cdot \mathbf{R} - \omega t)} \right). \qquad (A.2)$$

We then solve the time dependent Schrödinger equation in a basis of electronic eigenstates in the interaction picture:

$$i\hbar \frac{\partial |\Psi\rangle}{\partial t} = e^{i\mathcal{H}_0 \frac{t}{\hbar}} \mathcal{H}_{\mathrm{AF}} e^{-i\mathcal{H}_0 \frac{t}{\hbar}} . |\Psi\rangle \qquad (A.3)$$

$$i\hbar \sum_n \dot{a}_n |\psi_n\rangle = e^{i\mathcal{H}_0 \frac{t}{\hbar}} \left( -\mathbf{d} \cdot \mathbf{E} \right) e^{-i\mathcal{H}_0 \frac{t}{\hbar}} \sum_m a_m |\psi_m\rangle \qquad (A.4)$$

Inserting the electrical field leads to::

$$i\hbar \dot{a}_n = -\frac{E_0}{2} \sum_m e^{i\omega_n t} e^{-i\omega_m t} a_m \langle \psi_n | \mathbf{d} \cdot \hat{\epsilon} \left( e^{i(\mathbf{k} \cdot \mathbf{R} - \omega t)} + e^{-i(\mathbf{k} \cdot \mathbf{R} - \omega t)} \right) |\psi_m\rangle \tag{A.5}$$

We now define $\omega_n - \omega_m = \omega_{nm}$ and use the dipole approximation where the wavelength of the applied field is considered much longer than the size of the atom, such that $e^{\mathbf{k} \cdot \mathbf{R}} = 1 + i\mathbf{k} \cdot \mathbf{R} \ldots \approx 1$:

$$i\hbar \dot{a}_n = -\frac{E_0}{2} \sum_m a_m \langle \psi_n | \mathbf{d} \cdot \hat{\epsilon} | \psi_m \rangle \left( e^{i(\omega_{nm} - \omega)t} + e^{i(\omega_{nm} + \omega)t} \right). \qquad (A.6)$$

Lets restrict ourselves to a system with only two electronic eigenstates: A ground level $|g\rangle$, and an excited level $|e\rangle$ with the energies $E_g$ and $E_e$ respectively. We interact with these levels with a laser with frequency $\omega$.

We can then write up the two coupled differential equations for the system from Equation A.5:

$$i\hbar\dot{a}_e = -\frac{E_0}{2}\left(a_g\langle\psi_e|\mathbf{d}\cdot\hat{\epsilon}|\psi_g\rangle\left(e^{i(\omega_{eg}-\omega)t}+e^{i(\omega_{eg}+\omega)t}\right)+a_e\langle\psi_e|\mathbf{d}\cdot\hat{\epsilon}|\psi_e\rangle\left(e^{i(\omega_{ee}-\omega)t}+e^{i(\omega_{ee}+\omega)t}\right)\right)$$

$$i\hbar\dot{a}_g = -\frac{E_0}{2}\left(a_g\langle\psi_g|\mathbf{d}\cdot\hat{\epsilon}|\psi_g\rangle\left(e^{i(\omega_{gg}-\omega)t}+e^{i(\omega_{gg}+\omega)t}\right)+a_e\langle\psi_g|\mathbf{d}\cdot\hat{\epsilon}|\psi_e\rangle\left(e^{i(\omega_{ge}-\omega)t}+e^{i(\omega_{ge}+\omega)t}\right)\right)$$

$$\text{(A.7)}$$

We now define the so called Rabi frequency:

$$\Omega_{km} = -\frac{\langle\psi_k|d|\psi_m\rangle E_0}{\hbar},\tag{A.8}$$

and the detuning:

$$\Delta = \omega_{eg} - \omega$$

$$\text{(A.9)}$$

and make the approximation that the laser frequency is close to resonance, meaning $\omega \approx \omega_{eg}$. The term $e^{i(\omega_{eg}+\omega)t}$ and $e^{i(\omega_{ge}-\omega)t}$ then oscillate so fast, that they average to zero over any reasonable timescale. We can also eliminate the terms that violate the parity dipole selection rule:

$$\langle\psi_g|\mathbf{d}\cdot\hat{\epsilon}|\psi_g\rangle = \langle\psi_e|\mathbf{d}\cdot\hat{\epsilon}|\psi_e\langle = 0.\tag{A.10}$$

This leaves us with:

$$i\dot{a}_e = \frac{\Omega_{eg}}{2}a_g e^{i\Delta t}\tag{A.11}$$

$$i\dot{a}_g = \frac{\Omega_{ge}}{2}a_e e^{-i\Delta t},\tag{A.12}$$

where we, for simplicity, have chosen the dipole orientation parallel to the laser polarization ($\mathbf{d}\cdot\hat{\epsilon} = d$).

If we assume the initial conditions $a_g(0) = 1$ and $a_e(0) = 0$, meaning the atom starts out in the ground state, we can solve these two coupled differential equations by first differentiating Equation A.11:

$$i\ddot{a}_e = \frac{\Omega_{eg}}{2}\left(\dot{a}_g e^{i\Delta t} + i\Delta a_g e^{i\Delta t}\right)$$

We then insert $\dot{a}_g$, and isolate and insert $a_g$ from Equation A.11:

$$i\ddot{a}_e = \frac{\Omega_{eg}}{2}\left(-i\frac{\Omega_{ge}}{2}a_e e^{-i\Delta t}e^{i\Delta t} - \Delta\dot{a}_e\frac{2}{\Omega_{eg}}e^{-i\Delta t}e^{i\Delta t}\right)$$

$$\ddot{a}_e + i\Delta\dot{a}_e + \left|\frac{\Omega_{eg}}{2}\right|^2 a_e = 0$$

$$\text{(A.13)}$$

This second order differential equation can be solved by guessing an ansatz of the form:

$$a_e(t) = C_1 e^{r_1 t} + C_2 e^{r_2 t}\tag{A.14}$$

where $r_1$ and $r_2$ are the roots of the differential equation:

$$r_1 = \frac{i}{2}\left(-\Delta + \sqrt{\Delta^2 + |\Omega_{eg}|^2}\right), \qquad r_2 = \frac{i}{2}\left(-\Delta - \sqrt{\Delta^2 + |\Omega_{eg}|^2}\right).$$

(A.15)

For simplicity we define the generalized Rabi frequency $\tilde{\Omega} = \sqrt{\Delta^2 + |\Omega_{eg}|^2}$:

$$a_e(t) = C_1 e^{\frac{i}{2}\left(-\Delta + \tilde{\Omega}\right)t} + C_2 e^{\frac{i}{2}\left(-\Delta - \tilde{\Omega}\right)t}, .$$

(A.16)

This can now be solved by using the initial conditions:

$$a_e(0) = C_1 + C_2 = 0$$
$$C_1 = -C_2$$

and from differentiating Equation A.16, and using Equation A.11:

$$\dot{a}_e(0) = C_1 \frac{i}{2}\left(-\Delta + \tilde{\Omega}\right) + C_2 \frac{i}{2}\left(-\Delta - \tilde{\Omega}\right) = -i\frac{\Omega_{eg}}{2}a_g(0)$$

$$C_1\left(-\Delta - \tilde{\Omega}\right) - C_1\left(-\Delta + \tilde{\Omega}\right) = \Omega_{eg}$$

$$C_1 = -\frac{\Omega_{eg}}{2\tilde{\Omega}}$$

$$C_2 = \frac{\Omega_{eg}}{2\tilde{\Omega}}$$

Finally collecting it all:

$$a_e(t) = -\frac{\Omega_{eg}}{2\tilde{\Omega}}e^{\frac{i}{2}\left(-\Delta + \tilde{\Omega}\right)t} + \frac{\Omega_{eg}}{2\tilde{\Omega}}e^{\frac{i}{2}\left(-\Delta - \tilde{\Omega}\right)t}$$

$$a_e(t) = \frac{\Omega_{eg}}{\tilde{\Omega}}i\sin\left(\frac{\tilde{\Omega}}{2}t\right)e^{-i\frac{\Delta}{2}t}$$

(A.17)

And calculating the probability of finding the atom in state $|\psi_e\rangle$:

$$P_e(t) = |a_e(t)|^2 = \left|\frac{\Omega_{eg}}{\tilde{\Omega}}\right|^2 \sin^2\left(\frac{\tilde{\Omega}}{2}t\right).$$

(A.18)

which is the well known result of Rabi oscillations, where $\tilde{\Omega} = \sqrt{\Delta^2 + |\Omega_{eg}|^2}$ is the generalized Rabi frequency.

# Polarizability

Considering a laser producing an electrical field given as:

$$E = E_0 \cos\left(\mathbf{k} \cdot \mathbf{R} - \omega t\right) \hat{\epsilon} = \frac{E_0}{2} \hat{\epsilon} \left(e^{i(\mathbf{k} \cdot \mathbf{R} - \omega t)} + e^{-i(\mathbf{k} \cdot \mathbf{R} - \omega t)}\right) \tag{B.1}$$

The interaction with an atom is described by the interaction Hamiltonian:

$$\mathcal{H}_{\mathrm{AF}} = -\mathbf{d} \cdot \frac{E_0}{2} \hat{\epsilon} \left(e^{i(\mathbf{k} \cdot \mathbf{R} - \omega t)} + e^{-i(\mathbf{k} \cdot \mathbf{R} - \omega t)}\right). \tag{B.2}$$

We then solve the time dependent Schrödinger equation in a basis of electronic eigenstates in the interaction picture:

$$i\hbar \frac{\partial |\Psi\rangle}{\partial t} = e^{i\mathcal{H}_0 \frac{t}{\hbar}} \mathcal{H}_{\mathrm{AF}} e^{-i\mathcal{H}_0 \frac{t}{\hbar}} . |\Psi\rangle \tag{B.3}$$

$$i\hbar \sum_n \dot{a}_n |\psi_n\rangle = e^{i\mathcal{H}_0 \frac{t}{\hbar}} \left(-\mathbf{d} \cdot \mathbf{E}\right) e^{-i\mathcal{H}_0 \frac{t}{\hbar}} \sum_m a_m |\psi_m\rangle \tag{B.4}$$

Inserting the electrical field leads to::

$$i\hbar \dot{a}_n = -\frac{E_0}{2} \sum_m e^{i\omega_n t} e^{-i\omega_m t} a_m \langle \psi_n | \mathbf{d} \cdot \hat{\epsilon} \left(e^{i(\mathbf{k} \cdot \mathbf{R} - \omega t)} + e^{-i(\mathbf{k} \cdot \mathbf{R} - \omega t)}\right) |\psi_m\rangle \tag{B.5}$$

We now define $\omega_n - \omega_m = \omega_{nm}$ and use the dipole approximation where the wavelength of the applied field is considered much longer than the size of the atom, such that $e^{\mathbf{k} \cdot \mathbf{R}} = 1 + i\mathbf{k} \cdot \mathbf{R} \ldots \approx 1$:

$$i\hbar \dot{a}_n = -\frac{E_0}{2} \sum_m a_m \langle \psi_n | \mathbf{d} \cdot \hat{\epsilon} |\psi_m\rangle \left(e^{i(\omega_{nm} - \omega)t} + e^{i(\omega_{nm} + \omega)t}\right). \tag{B.6}$$

When far away from resonance we consider any far off resonance interaction as a perturbation to the initial state and approximate:

$$a_n(t) = a_n^{(0)}(t) + a_n^{(1)}(t) + a_n^{(2)}(t) \ldots \tag{B.7}$$

where $a_n^{(0)}(t) = a_n(0)$ and:

$$i\hbar\dot{a}_k^{(i+1)}(t) = -\frac{E_0}{2}\sum_m a_m^i\langle\psi_k|\mathbf{d}\cdot\hat{\epsilon}|\psi_m\rangle\left(e^{i(\omega_{km}-\omega)t} + e^{i(\omega_{km}+\omega)t}\right). \quad (B.8)$$

We then, once again, assume that the atom at $t = 0$ is in a single eigenstate $|\psi_g\rangle$ such that $a_g(0) = 1$. But this time we have many excited states $|\psi_{n\neq g}\rangle$ with $a_{n\neq g}(0) = 0$.

We can now find $a_k(t)$ to first order by integrating Equation B.8 from 0 to $t$:

$$a_k^1(t) = \int_0^t -\frac{E_0}{2i\hbar}\sum_m a_m^0\langle\psi_k|\mathbf{d}\cdot\hat{\epsilon}|\psi_m\rangle\left(e^{i(\omega_{km}-\omega)t'} + e^{i(\omega_{km}+\omega)t'}\right)\mathrm{d}t'$$

$$= -\frac{E_0}{2\hbar}\langle\psi_k|\mathbf{d}\cdot\hat{\epsilon}|\psi_g\rangle\left(\frac{e^{i(\omega_{kg}-\omega)t}-1}{\omega_{kg}-\omega} + \frac{e^{i(\omega_{kg}+\omega)t}-1}{\omega_{kg}+\omega}\right) \quad (B.9)$$

The factor of $-1$ describes transient effects. We can make them disappear by assuming that the laser has been on for a long time. We will choose to remove them now, though it won't be obvious until the next section why we chose so.

What we are actually interested in, is the magnitude of the induced dipole, or rather, the expectation value of the dipole operator to first order in perturbation theory:

$$\langle\mathbf{d}\rangle = \left(\langle\Psi|^{(0)} + \langle\Psi|^{(1)}\right)e^{i\frac{\mathcal{H}_0}{\hbar}t}\mathbf{d}e^{-i\frac{\mathcal{H}_0}{\hbar}t}\left(|\Psi\rangle^{(0)} + |\Psi\rangle^{(1)}\right).$$

$$= \left(\langle\psi_g| + \sum_n a_n^{*(1)}\langle\psi_n|\right)e^{i\frac{\mathcal{H}_0}{\hbar}t}\mathbf{d}e^{-i\frac{\mathcal{H}_0}{\hbar}t}\left(|\psi_g\rangle + \sum_m a_m^{(1)}|\psi_m\rangle\right)$$

$$= \overbrace{\langle\psi_g|\mathbf{d}|\psi_g\rangle}^{0} + \overbrace{\sum_{m,n}a_n^{*(1)}a_m^{(1)}\langle\psi_n|\mathbf{d}|\psi_m\rangle e^{i\omega_{nm}t}}^{0}$$

$$+ \underbrace{\langle\psi_g|\mathbf{d}\sum_m a_m^{(1)}|\psi_m\rangle e^{i\omega_{gm}t} + \sum_n a_n^{*(1)}\langle\psi_n|\mathbf{d}|\psi_g\rangle e^{i\omega_{ng}t}}_{2\mathrm{Re}\left\{\langle\psi_g|\sum_m a_m^{(1)}\mathbf{d}|\psi_m\rangle e^{i\omega_{gm}t}\right\}}. \quad (B.10)$$

Where the second term is zero due to parity as seen when we insert the expressions in Equation B.9 (ignoring the constants and exponentials and setting $\hat{\mathbf{d}}\cdot\hat{\epsilon} = 1$):

$$\sum_{m,n}a_n^{*(1)}a_m^{(1)}\langle\psi_n|\mathbf{d}|\psi_m\rangle = \sum_{m,n}a_n^{*(1)}\langle\psi_n|\mathbf{d}|\psi_m\rangle a_m^{(1)}$$

$$= \sum_{m,n}\langle\psi_g|\mathbf{d}|\psi_n\rangle\langle\psi_n|\mathbf{d}|\psi_m\rangle\langle\psi_m|\mathbf{d}|\psi_g\rangle$$

Now using the identity $\sum_k|\psi_k\rangle\langle\psi_k| = 1$:

$$\sum_{m,n}a_n^{*(1)}a_m^{(1)}\langle\psi_n|\mathbf{d}|\psi_m\rangle = \langle\psi_g|\mathbf{ddd}|\psi_g\rangle, \quad (B.11)$$

which is obviously zero due to the parity of $\mathbf{d}$.

We can then insert our expression for $a_k^{(1)}$ from Equation B.9 into Equation B.10:

$$
\langle \mathbf{d} \rangle = 2\mathrm{Re}\left\{ \langle \psi_g | \sum_m -\frac{E_0}{2\hbar} \langle \psi_m | \mathbf{d} | \psi_g \rangle \left( \frac{e^{i(\omega_{mg}-\omega)t}}{\omega_{mg}-\omega} + \frac{e^{i(\omega_{mg}+\omega)t}}{\omega_{mg}+\omega} \right) \mathbf{d} | \psi_m \rangle e^{i\omega_{gm}t} \right\}
$$

$$
= \sum_m \frac{2}{\hbar} \frac{\omega_{mg} \langle \psi_m | \mathbf{d} | \psi_g \rangle \langle \psi_g | \mathbf{d} | \psi_m \rangle}{\left( \omega_{mg}^2 - \omega^2 \right)} E_0 \cos(\omega t), \tag{B.12}
$$

where we immediately identify the last two factors as the electrical field defined in the beginning but with the dipole approximation. The sum then describes how much an atom gets polarized and is called the polarizability $\alpha$:

$$
\alpha(\omega) = \sum_m \frac{2}{\hbar} \frac{\omega_{mg} \langle \psi_m | \mathbf{d} | \psi_g \rangle \langle \psi_g | \mathbf{d} | \psi_m \rangle}{\left( \omega_{mg}^2 - \omega^2 \right)}, \tag{B.13}
$$

# Bibliography

[1] Baptiste Chupin. FREQUENCY COMPARISON (H_MASER 140 0889) - (LNE-SYRTE-FO2) For the period MJD 57824 to MJD 57839. Technical report, 2017.

[2] Z. W. Barber, J. E. Stalnaker, N. D. Lemke, N. Poli, C. W. Oates, T. M. Fortier, S. A. Diddams, L. Hollberg, C. W. Hoyt, A. V. Taichenachev, and V. I. Yudin. Optical lattice induced light shifts in an Yb atomic clock. *Physical Review Letters*, 100(10):6–9, 2008.

[3] BIPM. *Le système international d'unités (SI)*. 8th. edition, 2006.

[4] S. Blatt, J. W. Thomsen, G. K. Campbell, A. D. Ludlow, M. D. Swallows, M. J. Martin, M. M. Boyd, and J. Ye. Rabi spectroscopy and excitation inhomogeneity in a one-dimensional optical lattice clock. *Physical Review A*, 80(5):052703, 2009.

[5] C. Chou, D. Hume, J. Koelemeij, D. Wineland, and T. Rosenband. Frequency Comparison of Two High-Accuracy Al+ Optical Clocks. *Physical Review Letters*, 104(7):070802, 2010.

[6] A. Derevianko and H. Katori. Colloquium : Physics of optical lattice clocks. *Reviews of Modern Physics*, 83(2):331–347, 2011.

[7] V. A. Dzuba and A. Derevianko. Dynamic polarizabilities and related properties of clock states of the ytterbium atom. *Journal of Physics B: Atomic, Molecular and Optical Physics*, 43(7):074011, 2010.

[8] C. J. Foot. *Atomic Physics*. Oxford University Press, 2008.

[9] H. Katori, M. Takamoto, V. G. Pal'chikov, and V. D. Ovsiannikov. Ultrastable Optical Clock with Neutral Atoms in an Engineered Light Shift Trap. *Physical Review Letters*, 91(17):173005, 2003.

[10] N. D. Lemke, A. D. Ludlow, Z. W. Barber, T. M. Fortier, S. A. Diddams, Y. Jiang, S. R. Jefferts, T. P. Heavner, T. E. Parker, and C. W. Oates. Spin-1/2 optical lattice clock. *Physical Review Letters*, 103(6):10–13, 2009.

[11] N. D. Lemke, J. von Stecher, J. A. Sherman, A. M. Rey, C. W. Oates, and A. D. Ludlow. p-Wave Cold Collisions in an Optical Lattice Clock. *Physical Review Letters*, 107(10):103902, 2011.

[12] L.-S. Ma, P. Jungner, J. Ye, and J. L. Hall. Delivering the same optical frequency at two places: accurate cancellation of phase noise introduced

by an optical fiber or other time-varying path. *Optics Letters*, 19(21):1777, 1994.

[13] P. W. Milonni and J. H. Eberly. *Lasers*. Wiley, 1988.

[14] N. Nemitz, T. Ohkubo, M. Takamoto, I. Ushijima, M. Das, N. Ohmae, and H. Katori. Frequency ratio of Yb and Sr clocks with 5e-17 uncertainty at 150 seconds averaging time. *Nature Photonics*, 10(4):258–261, 2016.

[15] T. Ohkubo. イッテルビウム　ストロンチウム光格子時計の時計遷移周波数比測定. PhD thesis, University of Tokyo, 2016.

[16] V. D. Ovsiannikov, S. I. Marmo, V. G. Palchikov, and H. Katori. Higher-order effects on the precision of clocks of neutral atoms in optical lattices. *Physical Review A*, 93(4):043420, 2016.

[17] S. G. Porsev, Y. G. Rakhlina, and M. G. Kozlov. Electric-dipole amplitudes, lifetimes, and polarizabilities of the low-lying levels of. *Physical Review A*, 60(4):2781–2785, 1999.

[18] S. G. Porsev, A. Derevianko, and E. N. Fortson. Possibility of an optical clock using the 61S0→63P0 transition in 171,173Yb atoms held in an optical lattice. *Physical Review A*, 69(2):021403, 2004.

[19] E. L. Raab, M. Prentiss, A. Cable, S. Chu, and D. E. Pritchard. Trapping of Neutral Sodium Atoms with Radiation Pressure. *Physical Review Letters*, 59(23):2631–2634, 1987.

[20] F. Riehle. *Frequency Standards*. Wiley, Weinheim, FRG, 2003.

[21] W. J. Riley and D. A. Howe. *Handbook of Frequency Stability Analysis*. Number 1. 2008.

[22] U. Schünemann, H. Engler, R. Grimm, M. Weidemüller, and M. Zielonkowski. Simple scheme for tunable frequency offset locking of two lasers. *Review of Scientific Instruments*, 70(1):242–243, 1999.

[23] D. A. Steck. Quantum and Atom Optics Textbook, 2007.

[24] F. R. Stephenson, L. V. Morrison, and C. Y. Hohenkerk. Measurement of the Earth's rotation: 720 BC to AD 2015. *Proceedings of the Royal Society A: Mathematical, Physical and Engineering Science*, 472(2196):20160404, 2016.

[25] M. Takamoto and H. Katori. Spectroscopy of the 1S0-3P0 Clock Transition of 87Sr in an Optical Lattice. *Physical Review Letters*, 91(22):223001, 2003.

[26] I. Ushijima, M. Takamoto, M. Das, T. Ohkubo, and H. Katori. Cryogenic optical lattice clocks. *Nature Photonics*, 9(3):185–189, 2015.

[27] D. J. Wineland and W. M. Itano. Laser cooling of atoms. *Physical Review A*, 20(4):1521–1540, 1979.

[28] R. Yanagimoto. *Characterization of collisional shifts in optical lattice clocks based on asymmetries in the Ramsey spectrum*. Bachelor thesis, Tokyo University, 2017.